Stony Brook University

DATA TO NEUT AND GENIE MC GENERATORS PREDICTION CC1π+/CCQE RATIO COMPARISON FOR NEUTRINO INTERACTIONS WITH T2K PØD DETECTOR AS INPUT TO T2K OSCILLATION ANALYSIS

A Dissertation Presented

by

Dmitriy Beznosko

to

The Graduate School

in Partial Fulfillment of the

Requirements

For the Degree of

Doctor of Philosophy

In Physics

Stony Brook University

May 2012

Stony Brook University

The Graduate School

Dmitriy Beznosko

We, the dissertation committee for the above candidate for the
Doctor of Philosophy degree, hereby recommend
acceptance of the dissertation.

Dr. Chang Kee Jung - Dissertation advisor
Professor of Physics, Department of Physics and Astronomy

Dr. Chiaki Yanagisawa - Chairperson of Defense
Professor of Physics, Department of Physics and Astronomy

Dr. George Sterman
Distinguished Professor of Physics, Department of Physics and Astronomy

Dr. Vera Gorfinkel
Professor of Electrical Engineering, department of Electrical & Computer Engineering

This dissertation is accepted by the Graduate School.

Charles Taber
Interim Dean of the Graduate School

Abstract of the Dissertation

Data to NEUT and GENIE MC Generators Prediction CC1π^+/CCQE Ratio Comparison for Neutrino Interactions with T2K PØD Detector as input to T2K Oscillation Analysis

by

Dmitriy Beznosko

Doctor of Philosophy

in

Physics

Stony Brook University

2012

Historically, neutrinos were introduces by W. Pauli in 1930. A non-zero rest mass is required to explain the oscillation phenomenon discovered by Super-Kamiokande experiment using atmospheric neutrinos, and later reaffirmed using atmospheric neutrinos and other atmospheric and accelerator experiments.

The T2K experiment is an off-axis long baseline neutrino oscillation experiment. It utilizes the intense ν_μ beam generated at the J-PARC accelerator complex in Tokai, Japan. It has a near detector, ND280, at 280m from the proton target, and Super-Kamiokande as far detector at 295 km. The cross-section measurement of the single charged current π+ production in neutrino interactions is to contribute to our understanding of the background for measurement of the θ_{13} mixing angle. However, this cross-section is not known well in the energy region ~0.6GeV that is the peak energy of the T2K neutrino beam. This affects the MC predicted neutrino reaction rates for both near and far detectors. This dissertation compares the ratio of the single charged current π+ production rate over the charged current quasi-elastic production rate between the data and the predictions of neutrino interaction MC event generators (NEUT and GENIE) using the Pi-Zero detector (PØD), a part of the ND280 near detector. This is done for both the water-in and water-out data of 9.89×10^{19} and 3.57×10^{19} protons on target respectfully. Additionally, the design, construction and the calibration of the PØD detector and its constituents, such as extruded scintillator and multi-pixel silicon photo detectors, are explained.

TABLE OF CONTENTS

LIST OF FIGURES

LIST OF TABLES

ACKNOWLEDGMENTS

At this time and achievement level, I would like to express my sincere appreciation to all those people, who helped me to get here. Starting with my parents, then a number of school teachers, university professors, to professors and students in my research group, and to my thesis advisor, I thank you all for the support both in life and in learning process.

1. INTRODUCTION

1.1 Neutrinos – Historic Overview

Neutrinos are neutral leptons of three generations: electron, muon and tau neutrino. Their existence was theoretically predicted by Wolfgang Pauli in 1930 to explain conservation of energy in beta decay $N \rightarrow N' + \beta$ ($n \rightarrow p^+ + e^-$). Without the neutrino, the energy of the electron in a beta decay of the nucleus N into N' and an electron is simply defined from the conservation of energy, assuming N is at rest. Then from the relativistic formulation of two-body decay we get the monochromatic energy spectrum for the electron from equation 1.1.

$$E_e = \left(M_N^2 + M_{N'}^2 - M_e^2\right)/2M_N \qquad 1.1$$

Instead, a continuous spectrum was observed with its maximum E_{max} reaching E_e from above formula. The proposed by Pauli particle (firstly called as "neutron" by Pauli with the name later reassigned by James Chadwick to a different particle before the neutrino was experimentally observed) explained this spectrum of now a three-body decay $N \rightarrow N' + \beta + \nu$. This had to be a not charged fermion to converse angular momentum and charge in this decay, and with a finite rest mass on the order of the mass of the electron. However, since the $E_{max} \approx E_e$, it was taken to be zero. The name neutrino, a small neutron, was introduced by Enrico Fermi in his publication on β-decay [1] since the name 'neutron' was assigned to a different particle at about the same time.

The first proof of electron (anti)neutrino existence, came from the inverse β-decay nuclear reactor experiment ($\overline{\upsilon}_e + p \rightarrow e^+ + n$) by Reines and Cowan in 1956 [2]. As for the muon neutrino and tau neutrino, these were observed at the Alternating Gradient Synchrotron at Brookhaven in 1962 [3] and by the DONUT collaboration at Fermilab in 2000 [4] respectively.

Ever since their discovery, neutrinos have remained mysterious and elusive particles even though that they are possibly the most abundant particles in the Universe. Due to neutrino's extremely small cross-section, the high intensity beams and very high mass detectors that are designed to study the neutrino oscillations will also shed light on its other properties as well.

1.2 Neutrino Oscillations Formalism

The history of the neutrino oscillations begins with Bruno M. Pontekorvo (1913-1993) who suggested a theoretical possibility for the oscillations in the lepton sector for the neutrinos [5], implying that neutrino has a non-zero rest mass. Experimentally, this was first related to the solar neutrino problem that arose after Ray Davis whose Homestake experiment tried to measure the solar neutrino flux and observed about a third from the expected value [6].

With a neutrino that has non-zero rest mass, it is possible that the mass eigenstates $|\nu_i\rangle$ and the observed interaction, or flavor, eigenstates $|\nu_\alpha\rangle$ do not correspond to each other. The flavor states are called the same as the lepton 'companion' of each neutrino (that is e, μ and τ), and mass eigenstates

are typically denoted as 1, 2 and 3. Then there is a mixing probability between these superimposed states; this superposition can be expressed via a unitary mixing matrix U:

$$|\nu_i\rangle = \sum_\alpha U_{\alpha i}|\nu_\alpha\rangle \quad , \quad |\nu_\alpha\rangle = \sum_i U^*_{\alpha i}|\nu_i\rangle \tag{1.2}$$

U is called the (Pontecorvo-) Maki-Nakagawa-Sakata matrix and it is 3x3 matrix for the current three known flavor states (4x4 if there is a sterile neutrino) with the following elements:

$$U = \begin{pmatrix} U_{e1} & U_{e2} & U_{e3} \\ U_{\mu 1} & U_{\mu 2} & U_{\mu 3} \\ U_{\tau 1} & U_{\tau 2} & U_{\tau 3} \end{pmatrix} \tag{1.3}$$

In the extended form with the neutrino states shown, the full mixing equation is:

$$\begin{pmatrix} \nu_e \\ \nu_\mu \\ \nu_\tau \end{pmatrix} = \begin{pmatrix} 1 & 0 & 0 \\ 0 & \cos\theta_{23} & \sin\theta_{23} \\ 0 & -\sin\theta_{23} & \cos\theta_{23} \end{pmatrix} \begin{pmatrix} \cos\theta_{13} & 0 & \sin\theta_{13}e^{-i\delta} \\ 0 & 1 & \sin\theta_{23} \\ -\sin\theta_{13}e^{i\delta} & 0 & \cos\theta_{13} \end{pmatrix} \begin{pmatrix} \cos\theta_{12} & \sin\theta_{12} & 0 \\ -\sin\theta_{12} & \cos\theta_{12} & 0 \\ 0 & 0 & 1 \end{pmatrix} \begin{pmatrix} e^{i\alpha_1/2} & 0 & 0 \\ 0 & e^{i\alpha_2/2} & 0 \\ 0 & 0 & 1 \end{pmatrix} \begin{pmatrix} \nu_1 \\ \nu_2 \\ \nu_3 \end{pmatrix} \tag{1.4}$$

The α_1 and α_2 are non-zero only if neutrinos are a Majorana particle; δ is a phase factor that is non-zero if the CP violation exists in the lepton sector.

The evolution in time of each mass state that is a component of a flavor state ($e^{-i(E_i t - p_i x_i)}$), expressed in natural units ($\hbar = c = 1$) and in highly relativistic limit ($t \approx L$) will have the following form:

$$|\nu_i(L)\rangle = e^{-i(E_i - p_i)L}|\nu_i(0)\rangle \tag{1.5}$$

with the momentum and the energy of the ν_i in the laboratory frame being the p_i and E_i correspondingly. As the neutrinos are highly relativistic, in this limit we have:

$$|\vec{p}_i| = p_i \gg m_i \Rightarrow E_i = \sqrt{p_i^2 + m_i^2} \approx p_i + \frac{m_i^2}{2p_i} \approx E + \frac{m_i^2}{2E} \tag{1.6}$$

with E being the total energy. This simplifies the eq. 1.5 as following:

$$|\nu_i(L)\rangle = e^{-im_i^2 L/2E}|\nu_i(0)\rangle \tag{1.7}$$

Then the oscillation probability between the two observed flavor states will be:

$$P_{\alpha\to\beta} = \left|\langle\nu_\beta|\nu_\alpha(t)\rangle\right|^2 = \left|\sum_i U^*_{\alpha i}U_{\beta i}e^{-im_i^2 L/2E}\right|^2 = \\ \delta_{\alpha\beta} - 4\sum_{i>j}\mathcal{R}e\left(U^*_{\alpha i}U_{\beta i}U^*_{\beta j}U_{\alpha j}\right)\sin^2\left(\frac{\Delta m^2_{ij}L}{4E}\right) + 2\sum_{i>j}\mathcal{I}m\left(U^*_{\alpha i}U_{\beta i}U^*_{\beta j}U_{\alpha j}\right)\sin\left(\frac{\Delta m^2_{ij}L}{2E}\right) \tag{1.8}$$

It is convenient to re-express the $\sin^2$ argument (oscillation phase) in different units considering that in modern experiments neutrino energy is on order of GeV, distance is in (hundreds of) km and the neutrino mass difference is on the eV order scale. Thus, by also adding back c and $\hbar$, we get:

$$\frac{\Delta m_{ij}^2 c^3 L}{4\hbar E} = \frac{GeV\, fm}{4\hbar c} \times \frac{\Delta m_{ij}^2}{eV^2} \frac{L}{km} \frac{GeV}{E} \approx 1.267 \times \frac{\Delta m_{ij}^2}{eV^2} \frac{L}{km} \frac{GeV}{E} \quad 1.9$$

For the illustration, for the 2-flavor oscillation example, the U matrix will be 2x2 and will simplify to have just a single oscillation parameter θ:

$$U = \begin{pmatrix} \cos\theta & \sin\theta \\ -\sin\theta & \cos\theta \end{pmatrix} \quad 1.10$$

Then the oscillation probability becomes:

$$P_{\alpha\to\beta} = \sin^2(2\theta)\sin^2\left(\frac{1.27\,\Delta m^2[eV^2]\,L[km]}{E_\nu[GeV]}\right) \quad 1.11$$

1.3 Current Oscillation Results

For the T2K experiment [7] with the initial ν_μ beam, the magnitudes of the two oscillation parameters from the U matrix are accessible: $U_{\mu 3}$ for the ν_μ disappearance and the U_{e3} for the ν_e appearance. These respective elements are:

$$U_{\mu 3} = \sin\theta_{23}\cos\theta_{13} \approx \sin\theta_{23}\,, U_{e3} = \sin\theta_{13}\, e^{-i\delta} \quad 1.12$$

T2K major goal is to measure the magnitude of the U_{e3} via the ν_e appearance the ν_μ beam. The probability for this channel is expressible as:

$$P_{\mu\to e} = \sin^2(2\theta_{13})\sin^2(\theta_{23})\sin^2\left(\frac{1.27\,\Delta m_{23}^2 L}{E_\nu}\right) + O\left(\frac{\Delta m_{12}^2}{\Delta m_{23}^2}\sin(2\theta_{13})\cos\left(\delta + \frac{1.27\,\Delta m_{23}^2 L}{E_\nu}\right)\right) + O\left(\left(\frac{\Delta m_{12}^2}{\Delta m_{23}^2}\right)^2\right) \quad 1.13$$

Thus, the number of the ν_e's observed is also dependent on the CP violation phase.

In addition, higher statistics accumulated will allow a significant improvement for the previously measured ν_μ disappearance channel. This process is described by:

$$P_{\mu\to\mu} = 1 - \sin^2(2\theta_{23})\sin^2\left(\frac{1.27\,\Delta m_{32}^2 L}{E_\nu}\right) \quad 1.14$$

And it is sensitive both to the angle and the mass splitting. The latter also provides the E_ν for the first oscillation maximum. With L being 295km for the T2K experiment, the neutrino beam peak energy E_ν should be ~0.6 GeV. The neutrino beam is also directed 2.5° off-axis to have a narrow energy peak.

The latest T2K oscillation results have been published recently. The ν_μ disappearance results are presented in Figure 1.1 [8]. The presented intermediate result is from using the first two years of data. The point of best fit from this measurement using a binned likelihood-ratio method is $\sin^2(2\theta_{23}) = 0.98$ and $|\Delta m^2_{32}| \sim 2.65\text{x}10^{-3}$ eV^2; the alternative analysis using the maximum likelihood method yields $\sin^2(2\theta_{23}) \sim 0.99$ and $|\Delta m^2_{32}| \sim 2.63\text{x}10^{-3}$ eV^2. Systematic errors on all results are <5%. The 90% confidence regions are presented in Figure 1.2.

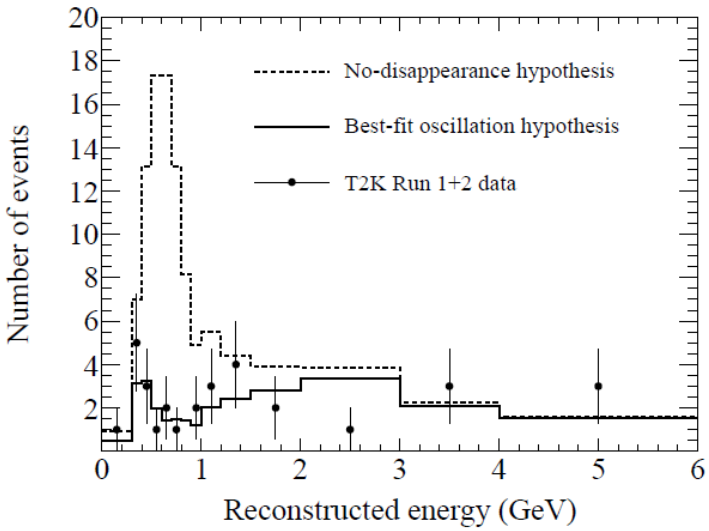

Figure 1.1: Far detector energy spectrum data compared with no-oscillation and $\nu_\mu \rightarrow \nu_\tau$ oscillation hypotheses.

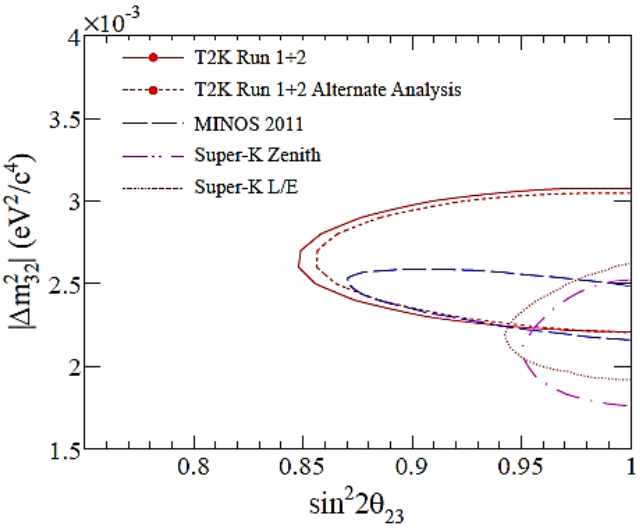

Figure 1.2: The 90% confidence regions for T2K results for $\sin^2(2\theta_{23})$ and $|\Delta m^2_{32}|$. The results are presented for both analyses.

The ~5% systematic error on the results includes a ~0.5% contribution (e.g. one tenth) from the CC1π/CCQE cross section uncertainty (or ~2% for non-oscillation hypothesis). The reduction of this and other cross section uncertainties will reduce the systematic error on the future T2K results.

The appearance results are presented in [9]. The total of 6 ν_e events was observed at the far detector for the current dataset. Including systematic uncertainties, the expectation is $1.5\pm0.3(5.5\pm1.0)$ events for $\sin^2(\theta_{13})= 0.0(0.1)$. This is a significant result that rules out the zero value for the θ_{13}.

However, more data are necessary to better determine the θ_{13} angle. Recent reactor experiments have rules out the zero-hypothesis with more then 5-sigma significance level.

For the above result, ~14%(~10%) of the systematic uncertainty falls onto the uncertainty in the cross section measurements. Thus we see that for the both main experiment results, the background contribution that comes from the cross sections uncertainty is considerable and a further study of them is needed.

1.4 Motivation for Data to MC Simulation Comparison Measurement

The T2K far detector, Super-Kamiokande (SK), is located at the Kamioka observatory. It is 50kton water Cherenkov detector. Primarily it will look for ν_e appearance from ν_μ beam. The background to this reaction is dominated by two sources: ν_e events from the primary beam contamination, and the background in SK detector that is coming from NC1π^0 production where only one γ from π^0 decay is reconstructed and is mis-identified as electron due to a small opening angle between γs or large energy asymmetry. PØD is designed to measure NC1π^0 production cross section on water to reduce the background effects on the final measurement.

The neutrino cross-section for the Charged Current single (CC1) π^+ resonant production on water is not studied well in the energy region that is available to T2K. This affects the MC predicted rates for both near and far detectors. These reactions include the following processes:

$$\begin{aligned} \nu_\mu p &\rightarrow \mu^- p \pi^+ \\ \nu_\mu n &\rightarrow \mu^- n \pi^+ \end{aligned} \qquad 1.15$$

They account for approximately 22% of the combined NC and CC cross-section. For the neutrino energy region of T2K, the resultant proton energy is too low for reliable detection; thus both processes produce similar event signature and are detected as same. The above reactions show directly the final particle states. The reactions proceed via the delta resonance, either Δ++ or Δ+, where delta decays:

$$\begin{aligned} \Delta^{++} &\rightarrow p \pi^+ \\ \Delta^{+} &\rightarrow n \pi^+ \end{aligned} \qquad 1.16$$

This combined cross-section is currently known to ~35% accuracy. However, its production rate is approximately three times the NC pion production rate for the same energy region; it is also related to this rate. Thus, more abundant and with easier to detect signature, comparison of the CC1π^+ events to the simulation prediction will allow for an early test of the detector functionality and reconstruction ability after its deployment.

In addition, the CC1π^0 production:

$$\nu_\mu n \rightarrow \mu^- p \pi^0 \qquad 1.17$$

that proceeds via the following delta resonance decay:

$$\Delta^+ \rightarrow p \pi^0 \qquad 1.18$$

for events, where muon energy is lower than detection threshold, provides sizably smaller contribution to the total π^0 background in SK detector that is coming from NC1π^0 production, as noted previously.

Understanding of this reaction production rate difference between the data and the simulation will contribute to the additional reduction of the systematic errors in the SK due to the cross-section uncertainties. The cross-section for this CC1π^0 production is related to the CC1π^+ cross-section via isospin symmetry as they all a part of the same isospin triplet. Thus measurement of the latter sets a better limit for this cross-section as well. Together, all these three reaction comprise the total CC1π resonant production cross-section for this neutrino energy region.

The result is presented as the CC1π^+ to the CCQE ratio. The CCQE reaction is the charged current interaction where no other particles exit the nucleus besides the muon and proton:

$$\nu_\mu n \rightarrow \mu^- p \qquad 1.19$$

and it accounts for almost 40% of all the interactions at T2K energies.

The reason for the ratio is to remove the beam flux uncertainty, and to remove or reduce other analysis systematics.

2. T2K EXPERIMENT OVERVIEW

2.1 General Overview

T2K (Tokai to Kamioka) is the second generation long baseline neutrino oscillation experiment based in Japan. It consists of three parts; an artificial off-axis neutrino beam line at the J-PARC facility, a Near Detector site 280 meters from the beam start point (ND280) [7], and Super-Kamiokande acting as the far detector, 295 km from Tokai. Among its main physics goals is a measurement of the θ_{13} neutrino oscillation parameter, by searching for ν_e appearance in the ν_μ beam.

The beam line consists of the 30 GeV proton beam incident on a graphite target. This is followed by focusing horn system, helium filled decay volume, beam dump, muon monitor and ND280. The neutrino off-axis beam energy at ND280 off-axis detector is expected at ~0.6 GeV at peak intensity value with a narrow energy band.

ND280 on-axis detector is to measure beam parameters such as direction, profile and intensity. ND280 off-axis detector is comprised of several sub-detectors in the magnetic field.

2.2 Primary Proton Beam

The primary proton beam is created using the J-PARC accelerator. The energy and other specifications given are for the data sample analyzed in this dissertation.

The beam starts as H^- and is accelerated to 181MeV by a linear accelerator (LINAC). At the injection to the rapid cycling synchrotron (RSC), beam is converted to H^+ (p^+) by charge stripping foils. The RSC operates on a 25Hz cycle and accelerates the beam to 3GeV with two bunches in each cycle. For further acceleration, the beam is injected to the main ring (MR) that raises the energy to 30GeV, with eight bunches (six before June 2010) at about 0.3Hz. At the extraction point for the T2K neutrino beamline, these bunches are extracted by a set of kicker magnets.

2.3 Neutrino Beam Description

The T2K neutrino beamline consists of primary and secondary sections. Primary one is used to direct the beam towards SuperK and ND280; it also includes beam intensity, beam position, beam profile and beam loss monitors.

The secondary beamline includes the target, focusing horns, decay volume, beam dump and muon monitor.

Beam intensity is measured using 5 current transformers, each being a toroidal coil of 50 turns with a ferromagnetic core. The intensity is measured to ~2% with ~0.5% fluctuations.

Beam position monitor measures the top-bottom and left-right asymmetry in the beam without affecting it. It uses four cylindrical electrodes around the beam (each covering 80°). The beam asymmetry then would induce current on these electrodes. The current measurement precision is ~450μm that is less than the required value of 500μm.

Beam profile measurements are conducted only during the beam tuning since they cause a beam loss of about 0.005%. These are done using two stripped (vertically and horizontally) titanium 5μm thin foils that are remotely inserted into the beam, with a high voltage anode foil between then. The anode collects the secondary electrons from beam interactions in the foils that are proportional to the beam intensity. From the drift time the charge, thus intensity, profile is reconstructed.

For beam loss monitoring, the number of wire proportional chambers are installed in the focusing and arc sections. The per-spill integrated signal is monitored to stay below threshold or beam is aborted. The sensitivity of this method is down to 16 mW of beam loss.

The first major part of the secondary beamline is a beam target: a 91.4 cm long, 2.6 cm in diameter graphite rod. The whole target is inside a first horn and it is cooled by helium gas flow through the special gaps. This is specifically important at the peak design beam power of 750 kW.

The three horns constitute the focusing system for the interaction products from the target. Each horn has an inner and outer conductor encompassing the volume within it. The 1/r (from the horn axis) toroidal field is created. The normal operations current is 320 kA (with corresponding magnetic field of 2.1T).

Decay volume follows the horns. The interaction products from the target (mostly pions and some kaons) are allowed to freely decay in this volume producing the neutrino beam. It is a 1.4m x 1.7m at upstream and 3.0m x 5.0m at downstream end 96 m long steel tunnel filled with helium gas to minimize any interactions within the volume. The water cooling system is in place to cool the walls below 100 ^{o}C.

The remaining interaction products and decay products are deposited into the beam dump at the end (with neutrinos continuing through). The beam dump is mostly a graphite core (75 tons) that is ~3.2m x 1.9m x 4.7m, with total 17 iron plates in front and back, with total thickness of 2.4 m. It is water cooled to below 100 ^{o}C. Besides neutrinos, muons with energy above about 5 GeV will pass through to the muon monitor.

The muon monitor is used for the beam direction and intensity monitoring using the muons produced in the decay volume. This way, the neutrino beam direction can be obtained to better then 0.25 mrad and the intensity to about 3%.

2.4 Global Alignment and Time Synchronization

For the global reconstruction between the near and far detectors, the timing of the beam spills is synchronized using a GPS system. There are a primary and secondary GPS, each having main and a backup system (total of 4) at the Tokai site. The same system is also used for distance measurements between the sites. The time synchronization is to about 50ns. The distance survey is conducted yearly and is done to about 7m precision (with 295km between the near and far sites). At the far detector, timing is used to reduce the background by selecting events within a microsecond around the beam spill.

2.5 ND280 On-axis detector – INGRIG

A front-most part of the near detector located at 280m site (ND280) is the on-axis detector that is designed to measure the neutrino beam intensity profile and direction. The Interactive neutrino grid (INGRID) detector is built from 14 identical iron-scintillator modules arranged in a cross-like shape (with horizontal part at ~33m below ground in a ND280 pit), with two additional modules at the off-axis locations outside of the cross above the horizontal part – to measure the beam axial symmetry. The scintillator channels are read-out using the Kuraray [10] wavelength shifting (WLS) fibers and MPPC photo sensors [11]. At the center of the cross (and beam) the two INGRID modules overlap (each cross bar is 7 modules); between these two there is Proton Module, a different module type. It has different scintillator planes without iron for improved tracking capabilities, and is surrounded by the veto planes.

2.6 ND280 Off-axis Detectors Overview

ND280 off-axis detector consists of several sub-detectors, all inside the UA1 magnet internal volume (7.0m x 3.5m x 3.6m) in ~0.17T magnetic field for accurate momentum measurements and charge discrimination. The intended measurements to be made using this detector group include neutrino beam energy spectrum, flux, ν_e contamination, background, and cross sections measurements. This detector group is in the direction of the far detector.

The following are the off-axis sub-detectors (Figure 2.1):

- PØD - Pi-Zero Detector
- TPC – time projection chamber
- FGD-fine grained detector
- DSECAL – downstream electromagnetic calorimeter
- SMRD – Side Muon Range Detector (inside yoke).
- PØD and Barrel ECALs

With exception of TPC, each detector utilizes scintillating bars, wavelength shifting fibers and a photon detector with the same readout/digitization scheme. Therefore, a use of efficient, high performance photon detector that operates in magnetic field is required.

2.6.1 PØD

The Pi-Zero Detector (PØD) is among the off-axis sub-detectors. It is primarily designed to measure NC1 π^0 production cross section on water to better estimate the background. PØD is a series of 40 alternating x-y orientation of the TiO_2 coated triangular extruded scintillator bars with co-extruded hole [12], with Kuraray [10] Y11 wavelength shifting fibers and single side readout using the MPPC [11] photo sensors. A light injection system for calibration purposes is used.

PØD has two ECAL parts (with lead sheets between planes) and two Water Targets with water bags between planes. Figure 2.2 shows the PØD schematic design. The further description of the PØD design, construction, calibration and data analysis will be done later in this dissertation.

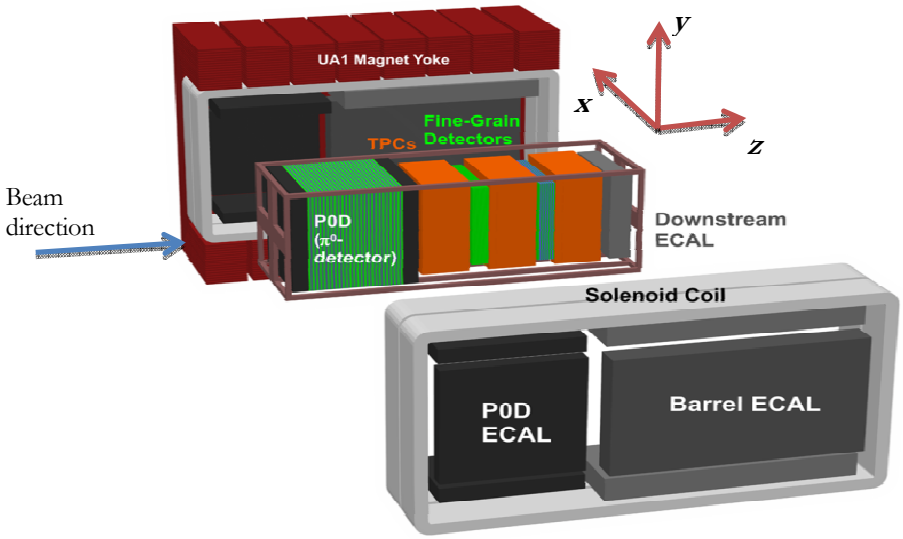

Figure 2.1: T2K ND280 off-axis detectors.

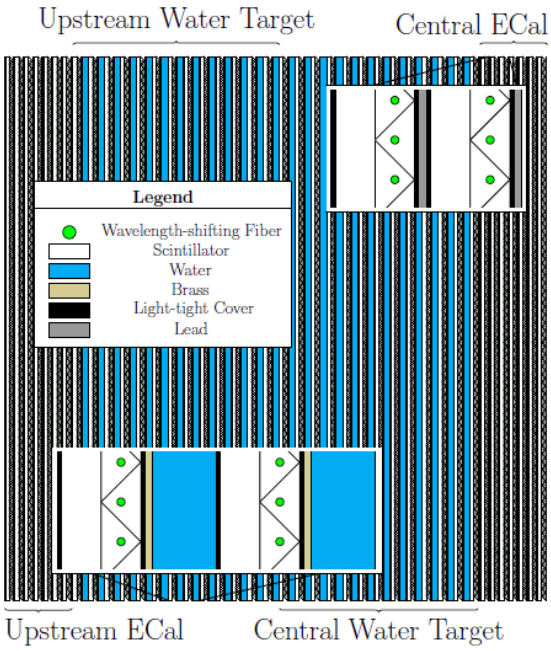

Figure 2.2: PØD Schematic design.

2.6.2 TPC

The Time Projection Chamber (TPC) is the next detector behind the PØD. There are three TPC modules sandwiched with two FGR, together forming the tracker. The inner volume of each TPC has an argon-based gas mixture and the central cathode and the side detectors for the passing particle detection. The TPCs are used for the charged particle 3D track imaging, precision momentum measurement in the magnetic field, and particle ID based on the ionization amount.

2.6.3 FGD

The two FGD modules are made from rectangular 9.6mm x 9.6mm x 1864.3mm scintillator bars with alternating x or y orientation of the layer, with 1.1ton each module. They provide the target mass for the TPCs (with the PØD being a target mass for the first TPC). The WLS fibers are used being read using MPPC sensors from alternating sides within each layer. A light injection system for calibration purposes is used. The first module has a total of 30 layers, and second had 7 scintillator layers and 6 with water bags as target mass.

2.6.4 PØD, Barrel and Downstream ECALs

The ECAL elements surround the inner detector from all sides except the upstream. It uses long scintillator bars with lead shoots between them to operate as 'tail-catcher' that is to provide hermiticity for all particles exiting the central detector units. The main task is to reconstruct the π^0s produced in the detectors and provide information on the escaping energy. There are 13 modules in total: one at the downstream end (DSECAL) and 6 on all four outer sides of the PØD and Tracker attached to the inner side of the magnet (two on top and bottom so that magnet can be opened).

2.6.5 SMRD

Located within the spaces in the magnet yoke is the Side Muon Range Detector (SMRD). Its main functions are to register the muons that exit the central detectors at large angles w.r.t. the beam, and to provide the cosmic rays trigger for muons that enter or traverse the detector. In addition, it measures beam interactions within the magnet and the pit walls, and provides a certain measure of the beam profile at the off-axis detector site as a difference in detection rates in different parts of the SMRD. The 440 scintillator planes that comprise this detector are placed in the gaps of the 16 C-shaped magnet yokes. There are two differently sized scintillator planes (875mm x 167mm x 7mm for horizontal and 875mm x 175mm x 7mm for vertical modules) with an S-curved groove for the WLS fiber and the MPPC readout on both sides of the fiber for determination of the hit position in the plane by the time difference in signal detection.

2.7 Far Detector – Super Kamiokande

At 295km, the far detector, Super-Kamiokande (SK), is located at the Kamioka observatory. It is 50kton water Cherenkov detector, with cylindrical shape and 41.4 m in height and 39.3 m in diameter. There is an inner detector with 11146 20-inch diameter PMTs on the inside of the divider wall facing inward (36.2m in height and 33.8m in diameter), and an outer detector with 1885 8-inch diameter PMTs on the outside of the divider facing outward.

The difference between the Cherenkov light from muons and electrons is determined from the detected light cone difference: electrons scatter more thus yielding a fuzzy ring that is different from the clear and clean ring from the muons. Thus the SK detector sees gamma and electron same - they both produce e-like ring. And it could mistake π^0 for a single electron if the two π^0 decay γs have a small opening angle or large energy asymmetry typically due to the relativistic boost. In both cases, only one e-like ring is detected. Therefore, π^0s present a background to the ν_e appearance and the study of π^0 cross-section on water is important for the experiment background reduction. Further information on SK can be found here [7].

3. SCINTILLATOR BARS AND WLS FIBERS FOR PØD DETECTOR

3.1 PØD Scintillator and Fiber Components

PØD comprises of series of triangular extruded TiO_2 coated scintillator bars with co-extruded hole [13] arranged in x-y sets (vertical bars and horizontal bars). Each set of x-y bars is manufactured separately and is designates as the PØDule. Each PØDule is ~2.2x2.3m, with 126 bars in x and 134 in y. Each bar is completed with Kuraray [10] Y11 mirrored wavelength shifting (WLS) fiber and Hamamatsu [14] MPPC photo sensor.

A total of 40 PØDules are in the PØD. Total length of all PØDules & targets assembled ~2.4m. For transportation convenience, these are divided into four SuperPØDules: Upstream and Downstream Electromagnetic Calorimeter (Ecal), and Upstream and Downstream Water Target (WT). Both Ecals are 7 PØDules each, with 4mm Pb radiator sandwiched between PØDules. Both WTs comprise of 13 PØDules with 1.6mm brass sheets, with upstream having 12 water bags (each bag is 3cm thick) and downstream 13, for total of ~3790 liters of water. See Figure 2.2 for the PØD structure design schematics.

This chapter covers scintillator production, a series of tests of the scintillator properties as well as a choice of the WLS fiber that were used in the final PØD design.

3.2 FNAL Extruded Scintillator

For the extruded scintillator, a continuous in-line compounding and extrusion process is used. The extrusion line is shown in Figure 3.1. This method allows to minimize the handling of the polystyrene pellets and dopants (1% by weight of 2,5-diphenyloxazole (PPO), and 0.03% by weight of 1,4-bis[2-(5-phenyloxazolyl)]benzene (POPOP)) that are the two major components of the extruded scintillator. A computerized system regulates the delivery of these components with high precision [12]. PØD triangular scintillator bars are shared together with MINERvA experiment [15].

The photograph of the cross-section for the triangular bar and the schematic are shown in Figure 3.2. Nominally, the size of each bar is 33.0±0.5 mm in base and 17.0±0.5 mm in height. The center position of the co-extruded hole is 8.5±0.25mm from base with a diameter of 1.7±0.2mm. All bars have 0.25mm thick layer of TiO_2 reflective coating. Due to extrusion process nature, the central hole is not fully circular and the size may vary within the limits indicated in specifications. However, all bars are tested using 1mm fiber to ensure that it will fit all the way through before bar is accepted. The dimensions for the scintillator bars were in part influenced by the bar size and the manufacturing facilities availability.

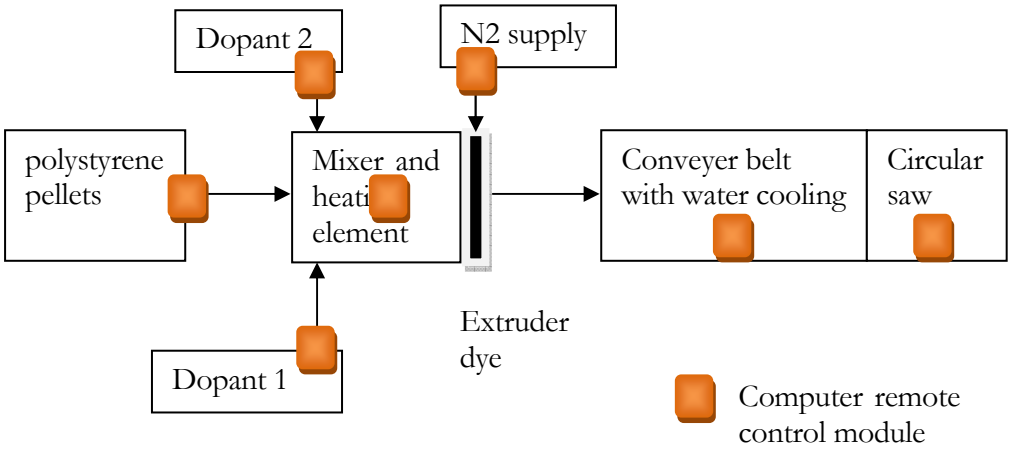

Figure 3.1: Extrusion line view (top) and schematic (bottom).

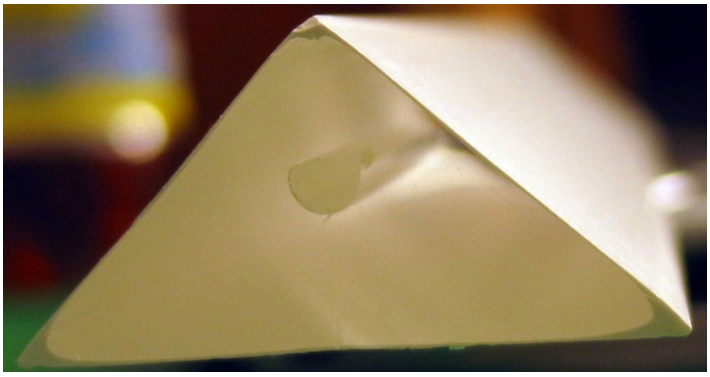

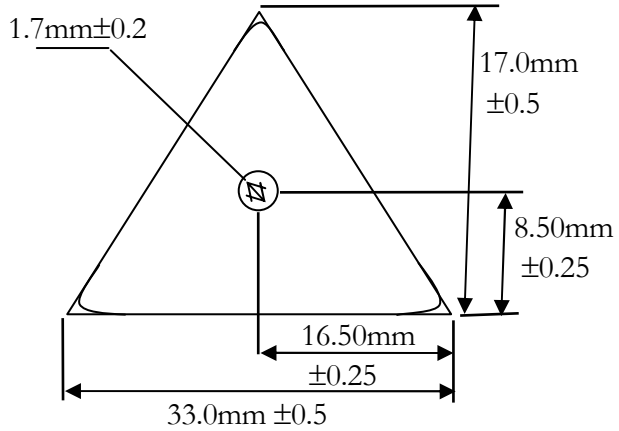

Figure 3.2: T2K-MINERvA Scintillator Bar.

3.2.1 Study of FNAL Extruded Scintillator

As mentioned above, the extruded scintillator is composed of polystyrene (C_8H_8) pellets (Dow Styron 663 W), 1% PPO and 0.03% POPOP [12]. The transparency and light yield of this scintillator is dependent on the details of technological process used for each particular production run, thus, a check of light yield and light attenuation is performed on the scintillator used for T2K [12]. In addition, coupling to the photo sensor and optical grease effects are studied as well [16] as discussed in chapter 3.3.

The following setup in Figure 3.3 was used for scintillator light attenuation and light yield measurements. The following elements were used in this setup: Hamamatsu [14] PMT R580 and readout by Keithley [17] 6485 picoammeter.

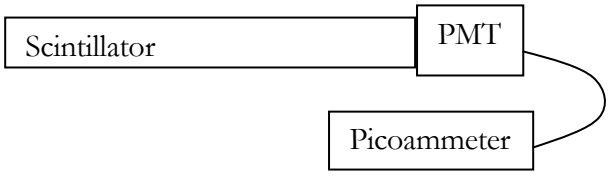

Figure 3.3: Setup for scintillator attenuation length and light yield measurements

To compare the light output level of extruded scintillator with other brand scintillators, the light output was measured for the following scintillators: extruded, Bicron [18] BC408 and Kuraray [10] SCSN-81. In this measurement, small pieces (2x0.5x2 cm^3) of scintillator, wrapped in the same material (aluminum foil), with one side without foil coupled to the PMT directly. A ^{106}Ru radioactive source was used and always placed at the same distance from the PMT. The results are shown in Table 3.1. The response is normalized to 1mm thickness.

Table 3.1: Scintillator Response.

TYPE	RESPONSE (μA)
FNAL-NICADD	2.0±0.2
BC408	2.7±0.2
KURARAY SCSN-81	2.0±0.2

These results are not corrected for spectral differences in the scintillator light emission and PMT response. This is the light output of the bulk scintillator. In small pieces the optical attenuation length differences among cast and extruded samples do not play a role. The extruded scintillator is a polystyrene-based scintillator (such as SCSN-81) with an intrinsic ~20% drop in scintillation yield when compared to poly(vinyltoluene)-based scintillator (such as BC408).

The results for the bulk scintillator light attenuation length (LAL) of the triangular shaped extruded bar is shown in Figure 3.4. Measurements were conducted using ^{137}Cs and UV LED, yielding similar results. For technical reasons, the zero position in radioactive source measurements is defined at the PMT, and at the end farthest from the PMT for LED measurements. A ~60cm long scintillator bar was used. For this test, a casing with ~1mm diameter hole for light output was built for the LED. Such LED light source was better collimated then the radioactive source. A wand configuration of gamma source without additional collimator was used.

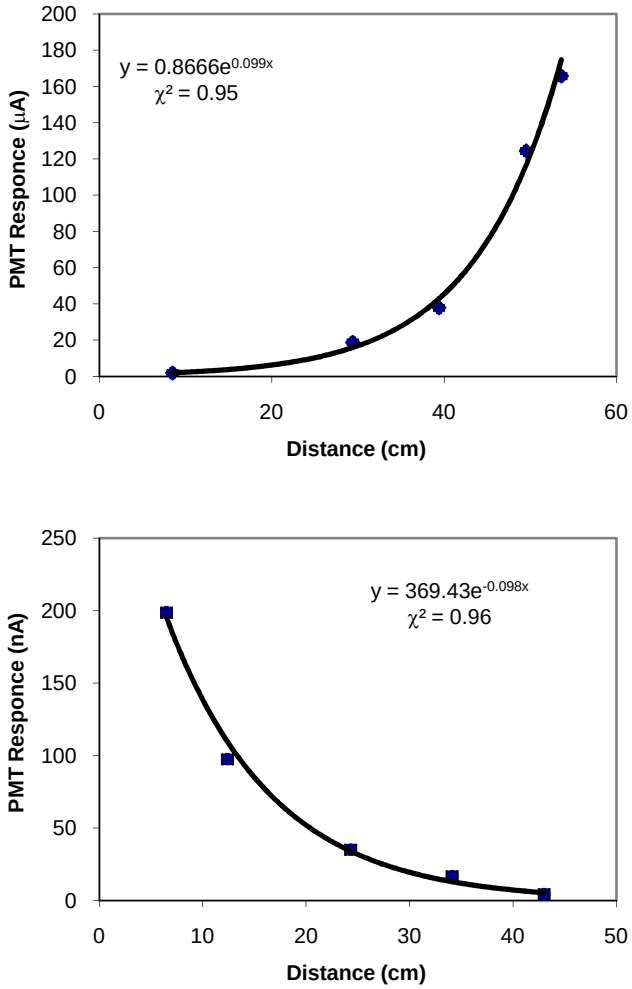

Figure 3.4: PMT response to UV LED position (top) and radioactive source position (bottom) along the bulk triangular shape scintillator without WLS fiber.

The tests yield LAL results of ~10.1±0.3cm for UV LED measurement and ~10.2±0.5cm for ^{137}Cs. The difference between results is well below measurement precision, indicating that UV LED in the attenuation length measurement performs similar to the radioactive source. A single-exponent fit was performed for it is a quick characterization of the material allowing quick comparison [13]. The LAL value for the cut and machined extruded scintillator bulk piece of 2x0.5x100cm^3 measures to be 38.0±0.7cm, and for BC404 cast scintillator (similar to BC408) that was machined to same size LAL measures to be 65.4±0.7cm [12]. This difference is expected due to the manufacturing process details (mainly melting temperature) of the cast and extruded scintillator.

3.2.2 Cross-talk Between Scintillator Bars

To access the level of optical cross-talk between two scintillator bars, a longer bar with covered ends was placed on top of the scintillator triangle attached to the PMT (as in Figure 3.3). 5mCi ^{90}Sr source was used on the top bar. Black paper was placed between the bars to access the radioactive background, and then removed for cross-talk measurement. The result showed negligible cross-talk (<1%) that is consistent with previous measurements [19].

3.2.3 Radiation Hardness Test

A simple test of the scintillator radiation hardness and annealing was conducted. Several samples of the extruded FNAL scintillator were irradiated to 0.5 and 1 Mrad in air utilizing a ^{60}Co gamma source with a dose rate of 0.8 Mrad per hour. Only minor degradation effects in light yield are observed, similar to the value observed in cast scintillator.

Table 3.2: Pulse height before and after irradiation.

DOSE (MRAD)	*BEFORE IRRADIATION*	*AFTER IRRADIATION*	*LIGHT YIELD LOSS (%)*
0.5	266±7	264±7	none
1	273±6	261±7	~5%

Light output measurements were performed using a ^{207}Bi radioactive source on scintillator discs (2 cm diameter and 1 cm thick) before and 85 days after the irradiation. The results are shown in Table 3.2. Light output is shown in arbitrary units. Thus we conclude that there is no radiation damage detectable up to 1 Mrad, as previously observed with cast scintillator samples. The delay in measuring the samples after irradiation is to allow for the natural annealing to occur. Measurements of light yield right after the irradiation were not carried over for technical reasons. Although the samples were irradiated in air, they underwent annealing because the dose rate had been high enough that the oxygen diffusion rate was smaller than its consumption rate. The final results are similar to those of an irradiation under inert conditions with the exception of the formation of oxidation products on the surface of the samples.

In addition, the transmittance of the scintillator was measured, both before and after the irradiation (see Figure 3.5). As with the light yield, no significant changes were observed. The minor variations among the spectra are within the accuracy of the instrument. The measurements were referenced to air as indicated by the solid absorption at low wavelengths and the poor transmission at long wavelengths. Since no significant change in transmittance was observed, a decrease of the light yield of the scintillator itself is most likely responsible for the changes seen in Table 3.2 [12].

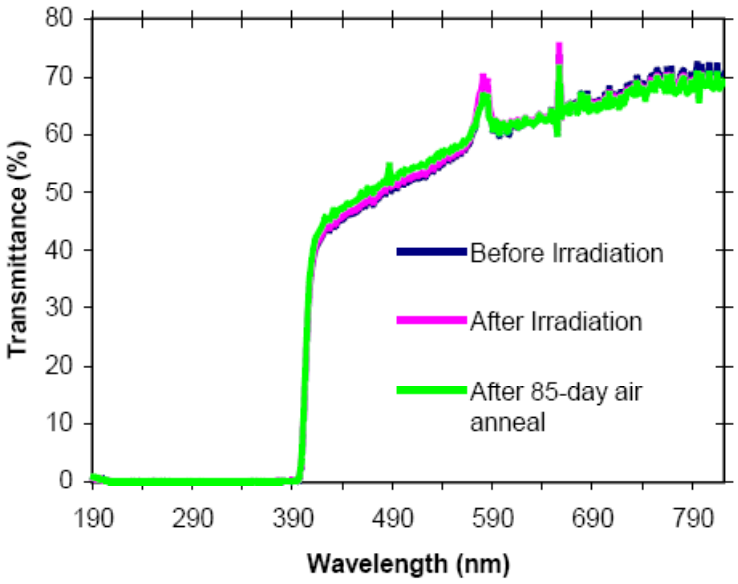

Figure 3.5: Transmittance of the extruded scintillator before, after and 85 days after

3.3 Scintillator to Photosensors - WLS Fiber Choice

Hamamatsu [14] MPPC photosensors have been used in PØD final design. They will be discussed in detail in the chapter **Error! Reference source not found.**4. However, a test using MRS (Metal-Resistor-Silicon), a photodetector of the same family, was conducted for the purpose of choosing the WLS fiber for the PØD design [16]. In addition, effects of the optical grease on the light output of the fiber were studied as well.

3.3.1 Optical Grease Effect on Light Output

Light output measurements for different WLS fiber diameter with and without optical grease in the co-extruded hole for Kuraray [10] Y11, and for 1.2 mm outer diameter Y7 fiber were conducted using the Hamamatsu [14] PMT R580. The PMT was readout by Keithley [17] 6485 picoammeter. The Y11 fibers with different diameters were tested to see the light yield change for each diameter in the same sized co-extruded hole; the Y7 fiber was 1.2 mm outer diameter only. Fibers were cut from a reel. All fibers were 16 cm in length; this is 2 cm longer than the scintillator piece used in this setup. The fibers' ends in contact with PMT were polished using a fly-diamond technique. The other ends of the fibers were cut at 45^{o} and painted black to prevent reflections. For the scintillator, a 14 cm piece of an extruded without the reflective coating triangular bar was used. The schematic of the setup used for these measurements is shown in Figure 3.6.

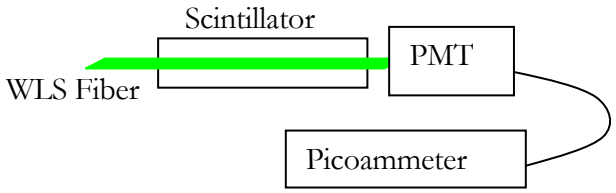

Figure 3.6: Setup schematic for measurements with WLS fibers.

The results for the light output for different diameter Y11fibers, and 1.2 mm Y7, with and without optical grease, are presented in Figure 3.7. For these measurements, the R580 PMT was biased at 1300V and directly connected to the picoammeter. The scintillator was illuminated by Bivar [20] LED5-UV-400-30 T1 3/4, 5 mm UV LED. Special care was taken to prevent LED light from reaching the PMT directly. A non-transparent cap was placed on the PMT to provide this needed light insulation and to hold fiber in place. All tested fibers were placed in front of the same photocathode area during this measurement. The Bicron [18] BC-630 optical grease was used.

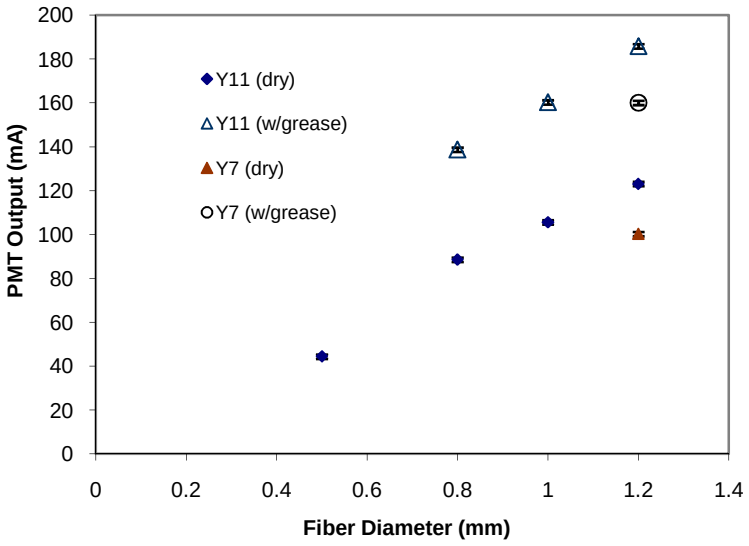

Figure 3.7: The PMT output for various WLS fibers (with and without optical grease for each fiber tested).

From Figure 3.7 we see the ~53% increase in light yield when the optical grease is used in the case of co-extruded hole. It indicates that gluing WLS fiber will provide similar increase in light output. The light yield of the 1.2 mm outer diameter Y7 WLS fiber, as measured by PMT, is lower than that of the 1.2 mm outer diameter Y11 WLS fiber. However, the later discussed in this chapter cosmic ray tests both using separate scintillator pieces and the PØDule prototype will indicate sufficient light output without gluing or grease.

3.3.2 WLS Fibers Light Attenuation

For the fiber attenuation length measurements, the 1.2 mm outer diameter 3 m long Y11 and Y7 fibers were used. In both samples, the concentration of dopant was 175ppm. Both fibers were polished at one end, and cleaved at 45° and painted black at the other. As a light source, a Bivar UV LED coupled to 2x2x3 cm extruded scintillator with co-extruded hole and no reflective coating was used. The pulse generator was providing the gate signal as well as 15 ns wide square pulses for LED.

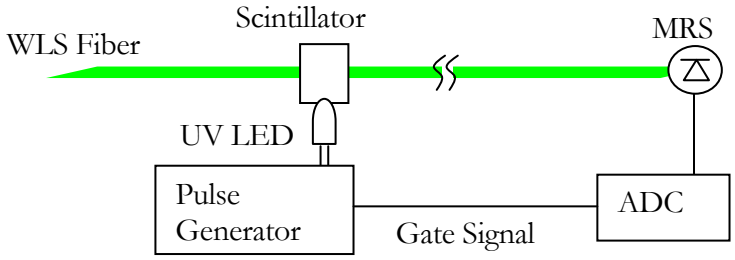

Figure 3.8: The setup for fiber attenuation length measurements.

The schematic for the light attenuation measurements in Y7 and Y11 fibers is shown in Figure 3.8. A small piece of scintillator without coating and with co-extruded hole was used in conjunction with UV LED as a light source. The results of these measurements are presented in Figure 3.10. As seen, Y7 performs better at rather short distance whereas Y11 is better at larger distances away from photodiode. The fitting with double exponent yields the following results: for Y11 get 35.5±0.3 cm and 463.4±1.2 cm for short and long components, and for Y7 we get 11.2±0.3 cm and 293.1±5.6 cm. Thus, Y11 has longer attenuation length that is better suited for the signal transmission from the far from photosensors side of the detector.

3.3.3 WLS Fibers Cosmic Rays Performance Test

Cosmic rays test was used to gauge the relative performance of both the WLS fibers and the various extruded scintillators. The following types and shapes of the scintillator were used: extruded scintillator with co-extruded hole and coating for the MINERvA [15] of both triangular and rectangular shapes (latter shown in Figure 3.9), and the K2K SciBar [21] 1.3x2.5 cm^2 rectangular extruded scintillator, also with co-extruded hole and coating.

For the measurements with cosmic rays, the ~14 cm long pieces of SciBar and MINERvA scintillators were used in conjunction with 1.2 mm pieces of Y11 and Y7 WLS fibers. The fibers were ~16 cm long, polished at one end and cleaved at 45° and painted black on the other because option of using mirrored fiber was unavailable at that time. There was ~1 cm between the sensor's cap (that held the fiber in alignment with photosensitive are of MRS) and the scintillator. For top and bottom triggers, the 1x2x10 cm pieces of extruded scintillator with co-extruded coating were used, coupled directly to the PMT face plate using optical grease. Figure 3.11 shows the schematic for this setup.

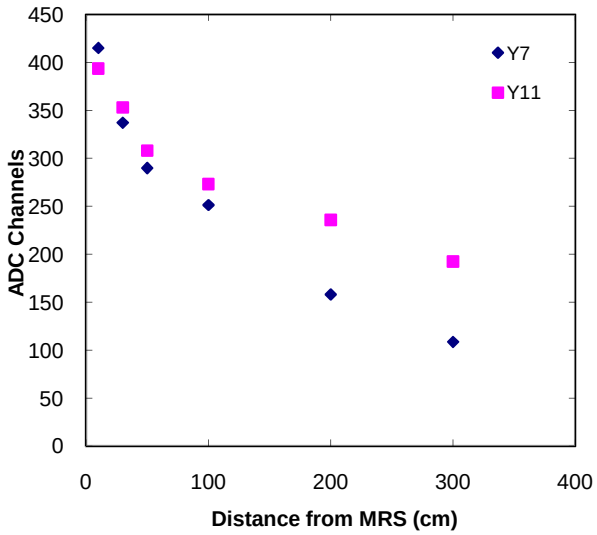

Figure 3.10: Response of Y11 and Y7 WLS fibers vs. distance from photodetector. The respective error bars are smaller than size of markers and are not shown.

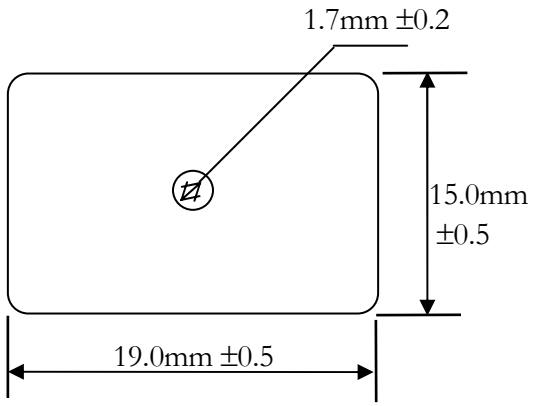

Figure 3.9: MINERvA rectangular shaped extruded scintillator with co-extruded hole and coating.

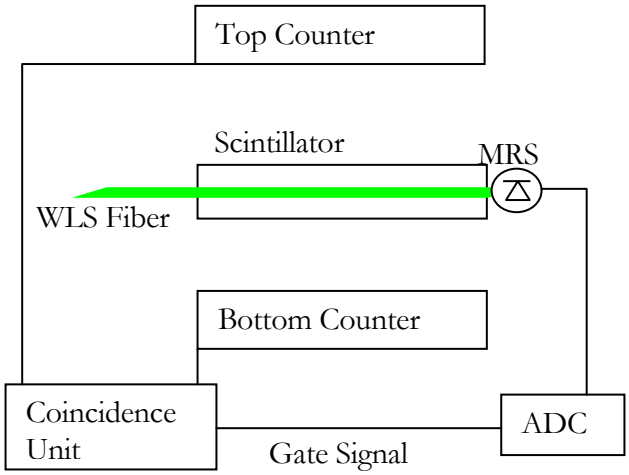

Figure 3.11: The setup for cosmic rays measurements.

Table 3.3: Light Yeild from Cosmic Rays For a Range of Scintilators Coupled to Photosensor via Y7 and Y11 WLS Fibers.

Scintillator	Fiber (1.2mm)	MRS Response (ADC Channels)	MRS Response (PE)
MINERvA Rectangular	Y11	159.2	19.5
SciBar	Y11	139.2	17.1
MINERvA Rectangular	Y7	179.4	22.0
SciBar	Y7	159.7	19.6
MINERvA Triangular (center)	Y7	138.2	17.0
MINERvA Triangular (side)	Y7	48.9	6

For this measurement, MRS photodiode was calibrated using the procedure described in [22]. The optimal operating bias voltage was found to be 27.84V. From calibration, one PE corresponded to ~8.15 ADC (analog-to-digital converter) channels. Results are summarized in Table 3.3. The ADC channel mean values and PE conversion are listed and are rounded off to first digit after decimal point. For MINERvA triangular scintillator, two results are quoted: "center" and "side". For "side" measurements, top trigger was turned 90^{o} (thus becoming 1 cm wide) and placed over the edge of the triangular scintillator. In all results quoted, the position of pedestal is subtracted.

Out of all recorded data, the lower signals discernible from noise were ~47 ADC channels (~5.8PE). In MINERvA "side" test, this value is indicative of the measurable response of the scintillator edge.

Even though Y7 fiber performs slightly better at short distances from the photosensor, at large distances (~2m) the better signal transmission by Y11 fiber is preferable.

3.3.4 PØDule Prototype Cosmic Rays Measurement

The measurement of the scintillator light yield using cosmic rays on the PØD prototype was performed. The results are presented in chapter 5.7.

3.4 Scintillator Light Yield in Magnetic Field

The measurements of the scintillator light yield and the LED performance in strong magnetic field will be discussed together with photosensor magnetic fields test in section 4.2.4. Tests conducted in magnetic field of up to 2.3T provided no evidence for scintillator light yield change with the field strength.

4. PHOTOSENSORS

4.1 Photosensor requirements

The choice of the photon detector was driven by the following requirements:

- Detector is in ~0.2T magnetic field – limits detector choice due to poor performance in the field of all PMT based devices.
- Within magnet, the space is limited for additional fiber routing for detectors placement outside of the magnet. Additional fiber also reduces light amount delivered to the sensors.
- Photosensor size – has to be small to fit within PØD structure.
- Reliable – for at least 10 years of experiment's running.
- Inexpensive to suit the budget.

The following options were considered and tested at SB:

- MCP–MAPMT - Micro-channel plate Multi-anode PMT
- Multi-pixel Silicon Photon Detectors Family
- SiPM (Silicon PMT)
- MRS (Metal - Resistive layer – Semiconductor diode)
- MPPC – Multi-Pixel Photon Counter

4.1.1 MCP–MAPMT testing

A Burle [23] 85011-501 device was used for the performance testing in the magnetic field. It is based on multichannel plate technology, with typical gain of about 7*107 and anode uniformity of 1:1.5. For nominal operations, the high voltage bias (HV) of -2600V is recommended by the manufacturer. Maximum photon detection efficiency (PDE) is achieved for light at 400nm wavelength (the peak output of Y11 WLS fiber is ~500nm).

This device was tested by Lisa Whitehead et. al. [24]. A strong dependence of the output to the angle between the device axis and magnetic field was found. Figure 4.1 shows the output dependence on the field strength at the 90^{o} between device axis and the field. No dependence was seen at 0^{o}.
In addition, cross-channel crosstalk was determined to be, on average, about ~9-10% between nearest neighbor anodes that are in 8x8 square arrangements. The purpose of this test was to indicate a possible alternative to the multi-pixel silicon detectors.

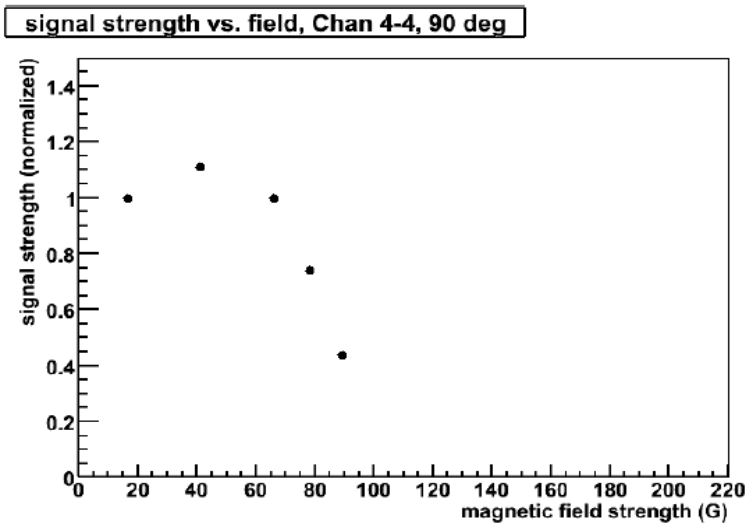

Figure 4.1: Burle 85011-501 MCP–MAPMT output vs. magnetic field strength at 90° between device axis and the field.

4.1.2 Limited Geiger mode

Avalanche photo diode (APD) is a reversed biased p-n junction that supports the amplification of the signal using impact ionization. An electron-hole pair is produced by photon absorption. Depending on applied bias polarity, electron or hole is accelerated from device's surface. As energy is gained, electron may produce another pair, etc. Typical gain achieved by this method is few hundred. Due to electron scattering and trapping at impurities and structure defects, the avalanche becomes self-sustaining at higher gain values, effectively shorting the device.

Geiger mode (in APD) is a runaway avalanche. In this mode, detector will only indicate photon detection, not light amount. However, the APD gain can be drastically increased. To avoid the avalanche becoming self-sustaining, a limiting circuitry is introduced for an effect that is generally called quenching. Two types are defined: active and passive quenching.

Active quenching constituted an external circuit, typically a fast controller chip that cuts bias voltage to quickly stop the avalanche after it is detected by increase in current drawn by the photon detector. This is a fast and effective method but requires additional circuitry that normally is not on the photosensor.

Passive quenching typically is a high value resistor that is internal to the sensor. As current drawn by the sensor rises, the voltage drop over the resistor will reduce the total bias at the photosensor, thus quenching the avalanche. This method is slower than active quenching and produces an output with longer exponentially decaying tail, but is cheaper and can be built into the device during the manufacturing process.

4.2 Studies of early multi-pixel family detectors

An idea of the silicon multi-pixel passive quenching Geiger mode Avalanche Photo Diode (APD) based detector existed for some time. Early attempts at designing such devices were unsuccessful until about year 2000 when first Russian-produced models became available.

Current implementation is the extension of the former Soviet Union military project for guided missiles. After demise of the Union, many such projects have been demilitarized and entered a civilian sector. First models available to researchers were Russia-produced SiPM and MRS sensors [22], tested at Fermi National Accelerator Laboratories (FNAL) for the proposed International Linear Collider digital hadron calorimeter and tail catcher [19] using proton test beam.

Latest success in mass production of the photo sensors of this type goes to Hamamatsu [14] with their Multi-pixel Photon Counter (MPPC) sensor.

4.2.1 Operational principle

A typical multi-pixel silicon family photon detector has from ~100 to ~1600 pixels (1mm^2 models). Each pixel (typ. up to 100μm x 100μm) is an APD in limited Geiger mode, with passive quenching by surface film resistor (Figure 4.2 [25]). Since each pixel can detect only light presence and not the intensity, thus for low light levels, when each pixel occupancy (detected_photon#/pixel#) is much less than 1, multi-pixel detector total output signal will is proportional to incident light flux since outputs of all pixels are collected by a common substrate.

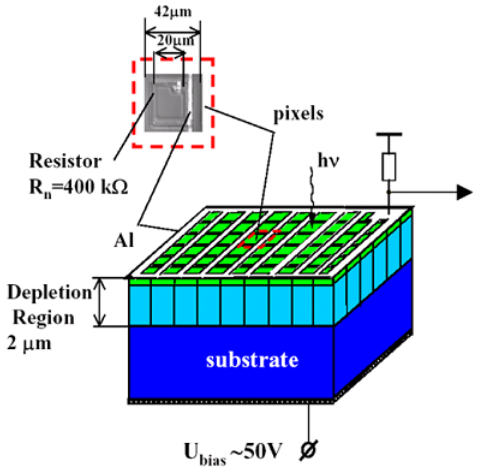

Figure 4.2: Multi-pixel silicon family detector schematic.

A single pixel schematic is shown in Figure 4.3 [25]. An incident photon, if absorbed, produces an electron-hole pair. Accelerated by intense electric field within the pixel (typ. up to 10^6 V/m), a hole or an electron (depending on biasing polarity) can start an avalanche in a pixel (pixel is said to 'fire').

Each pixel is passively quenched by means of a film resistor that is typically located on the device surface. As avalanche develops, rising current causes a voltage drop over resistor and reduces pixel bias below avalanche limit. This additionally protects the sensor from damage from high light levels.

Due to surface structure, these devices typically have overall PDE of 15-30% for green light (~500nm). With each pixel PDE being on order of ~60%-70%, lower overall value is due to inactive surface zones given to aluminum bias conductors and insulation between pixels. For this reason, models with fewer pixels generally have higher overall PDE. But even for the highest pixel models, their PDE is comparable or higher of that of the green-extended PMT.

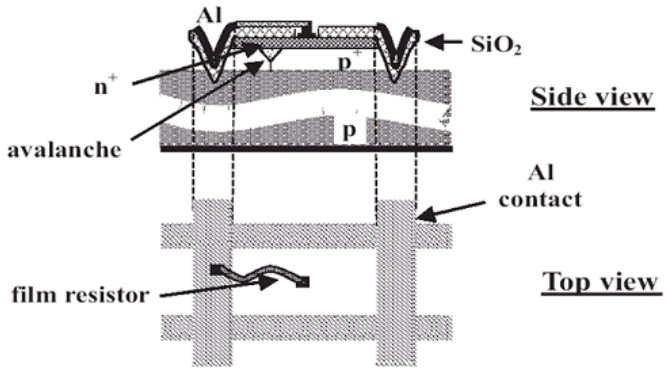

Figure 4.3: Single pixel structure schematic.

Thermally produced electron-hole pair can cause firing in the pixel. This is the dark noise for this device; it has same output shape as from detected single photon and is indistinguishable from the detected signal. In addition, there are an inter-pixel cross-talk and afterpulsing effects that will be discussed later in this chapter.

Figure 4.4 shows the schematic of the photosensor biasing with negative (-) polarity high voltage to obtain the negative polarity output. In order to use positive (+) high voltage for positive output, if needed, same circuit may be used with photosensor polarity reversed.

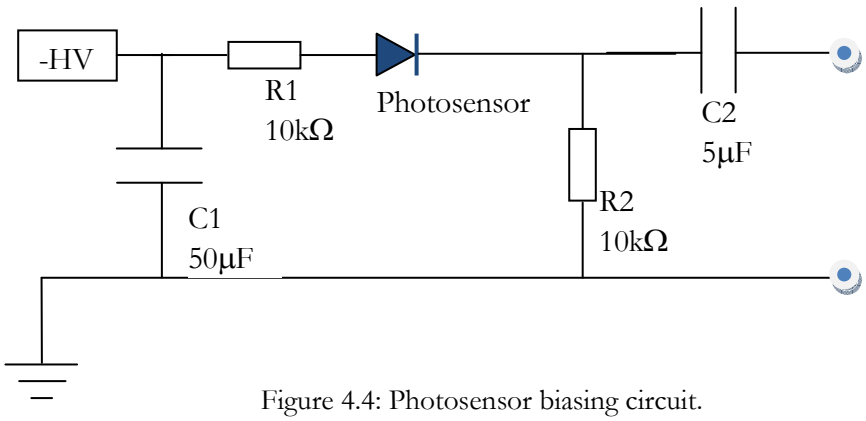

Figure 4.4: Photosensor biasing circuit.

4.2.2 MRS stability at working point

To determine the stability of the working point for the MRS, a LED signal was supplied to the sensor and a noise count rate taken at the set voltage. After twenty hours, the noise count rate was taken again and compared to the initial one (LED signal was at 58 Hz, temperature from the beginning to the end of the test was 22.8 °C ±0.1). Initially, at 50.40 V ±0.01 with the discriminator set at 80 mV threshold, the MRS count rate was 68.7 Hz ±1.1 (averaged over a three-minute period). After twenty hours of continuous operation, a noise rate of 69.2 Hz ±1.1 was measured (also averaged over three minutes). The rates measured are compatible within the estimated uncertainties.

4.2.3 Radiation Hardness Study

A separate study was undertaken to observe changes, if any, in the MRS sensor response after irradiation with a 1 Mrad dose of gamma rays. The sensor noise, amplification, signal detection, and bias voltage range were measured before and after irradiation. The details on how these measurements were obtained will be discussed further in this chapter because same setups were used for MPPC sensor as well. Only the result is presented here.

Figure 4.5 is a ratio of dark noise rate measurements vs. threshold at set bias before and after: any major changes would indicate damage to the internal cell structure of the sensor.

Figure 4.6 is a ratio of detected signal amplitude before and after irradiation. Any change would indicate, in part, that the sensor's surface has been affected by the radiation. And Figure 4.7 is a ratio of dark noise frequencies vs. bias: any changes would indicate change in the range of the bias voltage due to radiation damage.

Within experimental uncertainties, all the ratios are ~1, indicating that a 1 Mrad dose of gamma radiation causes no detectable damage to the sensor.

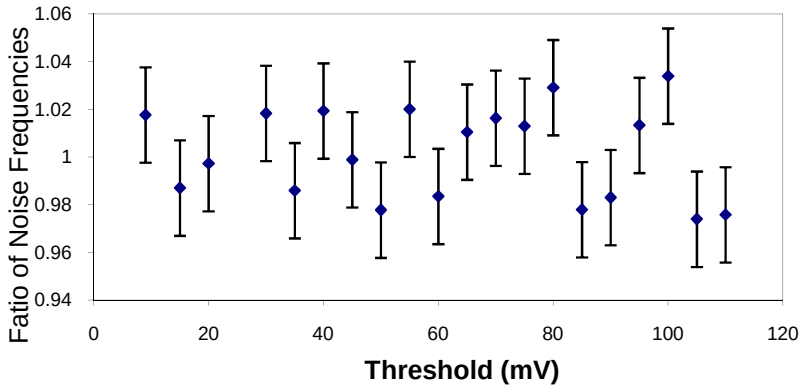

Figure 4.5: Ratio of dark noise rate vs. bias before to after irradiation.

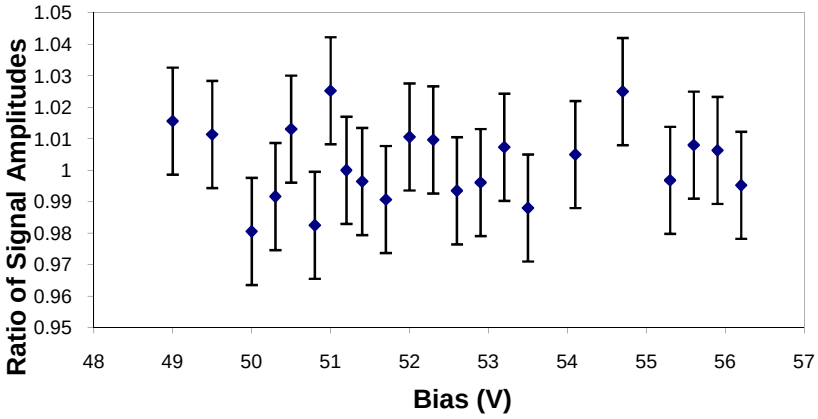

Figure 4.6: Signal amplitude ratio before to after irradiation.

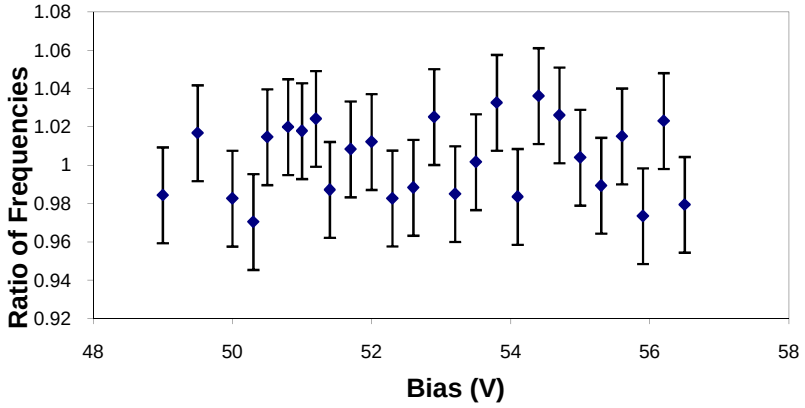

Figure 4.7: Ratio of dark noise rate at different biases of before to after irradiation.

4.2.4 Strong Magnetic Field Stability

The experimental results on the performance of the MRS (Metal/Resistor/Semiconductor) photodiode in the strong magnetic field of 9 T, and the possible impact of the quench of the magnet at 9.5 T on sensor's operation are presented.

All magnetic field measurements were performed at the Fermilab Magnet Test Facility. The magnet used for MRS measurements only was a standard Tevatron Dipole [26], whose field strength was ~1 Tesla per kA. This is a superconducting magnet with 29 mm aperture and field up to 10 T at about 2 K. The sensors were placed in the body of the magnet (far from the ends), where the field is very uniform (at the level of 1 part in 10000). The dipole field direction is vertical. The temperature in the magnet aperture was not cryogenic and was closer to room temperature, around 5-6 ^{o}C. Sufficient time was allocated for temperatures to equalize. The following characterizes the speed with which magnetic field collapses during a quench event: the current in the magnet decays (approximately) exponentially

with a time constant of about 0.25 seconds (determined by the L/R of the circuit that are not adjustable).

For this test, five MRS sensors were used, arranged in different directions with respect to the magnetic field. All sensors were biased at 29.1 V and at 30.0 V that were well within operating range of all five. An optical splitter was used to deliver similar amounts of light in the same pulse to each of the sensors.

The crystal used for splitting the light had a square cross-section being 5 mm wide and 30 mm long. At the output (front) end it had five symmetrical conical holes with 2 mm base diameter for each of them (Figure 4.8).

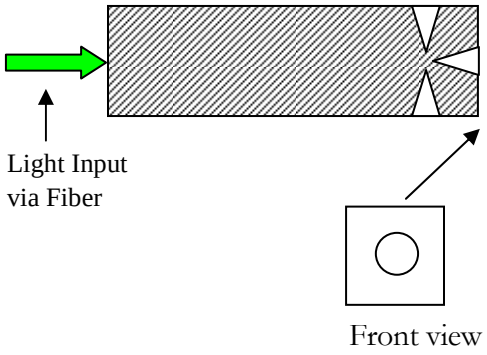

Figure 4.8: Schematic of the splitting crystal (cross section along the splitter).

The conical surfaces were not polished. Without these conical holes, the ratio of the direct light along the crystal to the "side" light at the front end the crystal was about 10 to 1. With conical holes, this ratio was less than two. No further effort was made to achieve further light uniformity in all directions since the goal was to get a comparable amount of light only. The positions of the photodetectors around the crystal were determined by these holes. The light splitting property of the crystal as measured by the same sensor is presented in Figure 4.9.

The light pulse was produced by the Bivar [20] UV LED (peak emission ~400 nm). The pulse from the pulse generator was ~30 ns wide with ~5.5 V amplitude. The LED was embedded into the 10 mm thick extruded scintillator [12]. The LED-scintillator part was placed well outside the magnet to avoid any effects of the field on it since only the photodetectors were studied here. The light pulse from the scintillator to the splitter was carried via ~2.5 m long, 2 mm outer diameter, Kuraray [10], multiclad, Y-11, wavelength shifting (WLS) fiber. The outputs of the sensors were fed into the Agilent [27] Infiniium 54832D MSO oscilloscope without additional preamplifier. The schematic of this module is given in Figure 4.10, and the schematic of the power circuit for the MRS is drawn in Figure 4.11.

The temperature inside the magnet was measured before and after the tests and was 5.0 ^{o}C $\pm$0.5. Table 4.1 shows the various properties of MRS output for all 5 sensors in their places with the test signal applied in the absence of magnetic field.

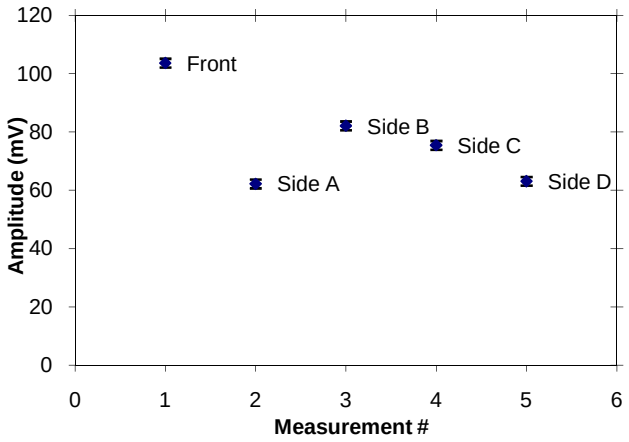

Figure 4.9: Uniformity of light output of splitting crystal.

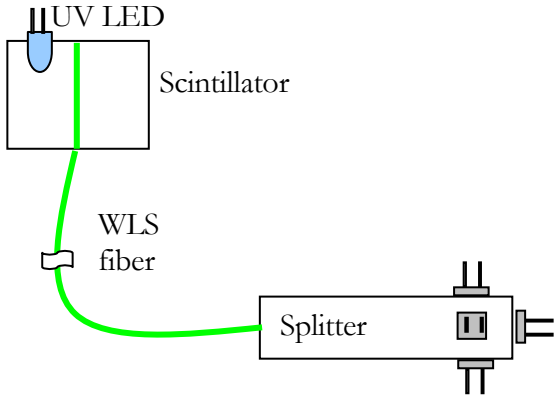

Figure 4.10: MRS module schematics.

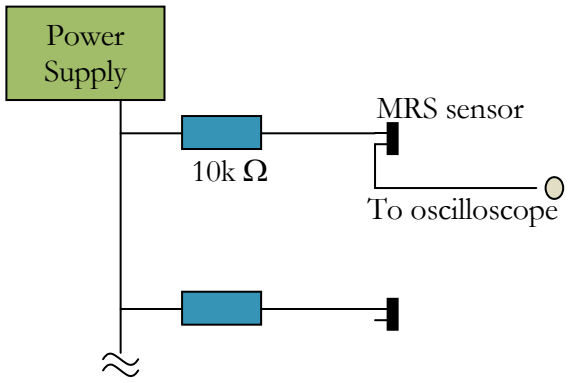

Figure 4.11: MRS power circuit schematics.

Table 4.1: Outputs for 5 channels with test signal.

Channel #	1	2	3	4	5
Area (nVs)	15.24	23.12	10.75	25.59	13.51
Amplitude (mV)	38.79	45.86	27.18	50.6	38.31
Rise time (ns)	30.55	43.16	33.69	38.94	30.50

The data for all 5 channels were obtained. Because of the similarity of the results, data only for channel 4 will be presented for illustrative purposes. This channel corresponds to the MRS sensor that was positioned at the tip of the splitter. The electrons in this sensor move along the same axis inside the magnet as the particle beam would, therefore, the MRS in channel 4 should experience the biggest effects of the B field, if any.

The following characteristics of the sensor's output were measured: amplitude, area, and rise time. Measurements were carried out at 0 T, 5 T, 9 T at 29.1 V bias, and at 0 T and 9 T for 30.0 V bias. In addition, measurements were performed immediately after magnet quench at 9.5 T (the field was already zero during these measurements). The pole with the sensors and the LED-scintillator part was inserted into the magnet approximately 4 hours before the experiment so that it would be at the same temperature as inside the dipole. A constant stream of nitrogen was pumped through the magnet throughout the test to remove the humidity.

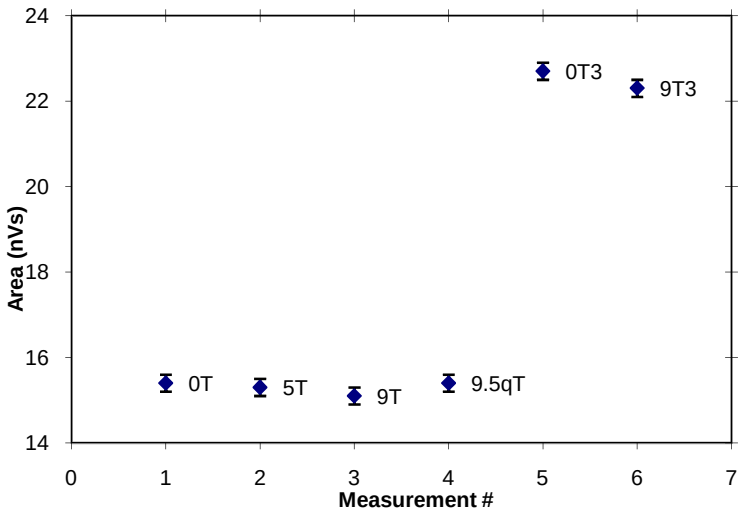

Figure 4.12: Area of the MRS output.

Figure 4.12 shows the values of the area of MRS output as a function of the magnetic field strength. The area is a measure of total charge of the output with a 50 Ω load. Each point in every figure is an average of at least few hundred measurements at each field strength value. The errors are given directly by the oscilloscope. Here and in all further plots 9.5qT label indicates a measurement done after the magnet quench at 9.5 T field, and 0T3 and 9T3 labels indicate measurements done at

30.0 V bias. The biggest difference between points at 0 T and 9 T is ~2% that is within the measurement error.

Figure 4.13 shows the values of the amplitude of MRS output as a function of the magnetic field strength. The amplitude is a measure of the peak current of the output with a 50 Ω load. The maximum of ~1.5% change in output amplitude between field strength values of 0 T and 9 T is observed.

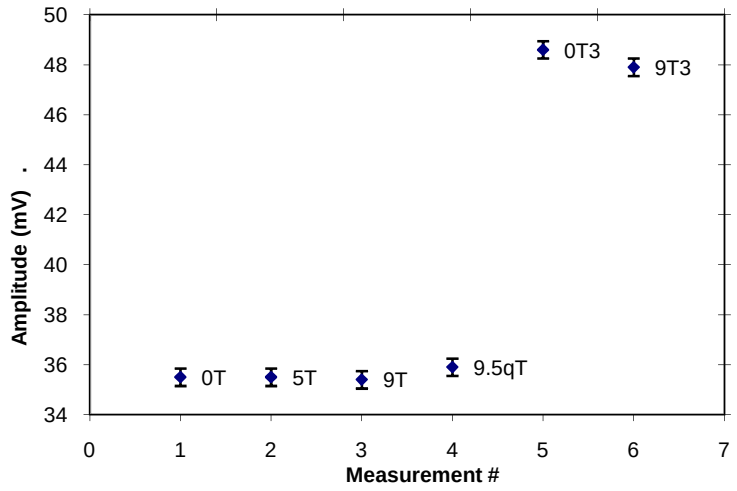

Figure 4.13: Amplitude of the MRS output.

The dependence of rise time on the magnetic field strength was also studied (Figure 4.14). The behavior of the signal rise time seems to be quite independent on the field strength with the maximum of ~1.5% change in output amplitude between field strength values of 0 T and 9 T is observed.

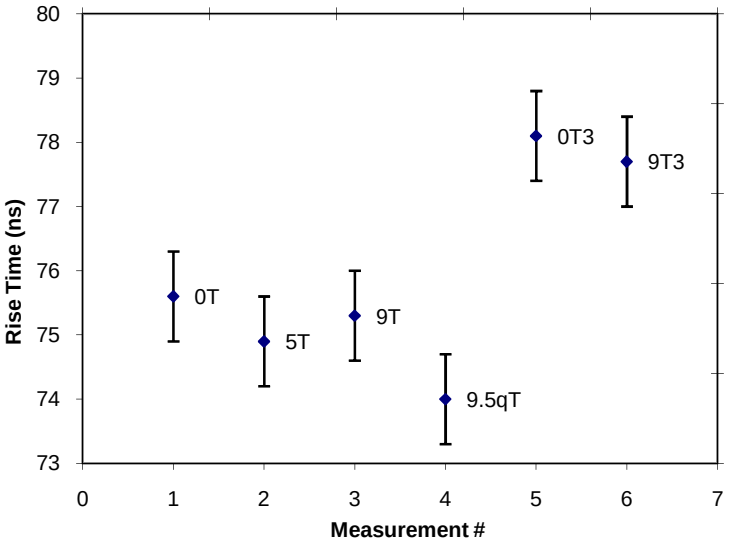

Figure 4.14: Rise time of the MRS output.

In conclusion, measurements performed using five MRS sensors in the strong magnetic field point to the insensitivity of the sensors outputs to the field strength of 9T within 1.5%-2%. In addition, measurements of the magnet quench effects on the MRS sensor indicate that magnet quench did not damage the sensors, and had none or immeasurably small lasting effect on the sensors outputs.

4.2.5 LED and scintillator testing in magnetic field

After the MRS photosensor was shown to be insensitive (within measurements accuracy) to the magnetic fields, a test of the various LEDs and the extruded scintillator was conducted [28].

A GMW Helmholtz Dipole Magnet, model 3474, by GMW Associates [29], was used. The diameter of the poles is 250mm, with maximum current of 140 Amps at 76 Volts (10.6 kW) while water-cooled. The field strength is dependent on the distance between the poles. Due to this limitation, the highest field achieved was 2.3 T.

A selection of LEDs was influence by the usage of the model in the detector, model availability and the peak emission wavelength. Also, LEDs with different manufacturing technology were picked. The following six LEDs were selected for the testing:

- Bivar [20] LED5-UV-400-30 T1 3/4 5 mm UV LED with peak emission at 400 nm;
- Lumex [30] SSL-DSP5093USBC Ultra Blue with peak emission at 475 nm, and SSL-LX5093UPGC/C Ultra-Pure Green with peak emission at 525 nm;
- Radioshack [31] 276-351 T-1-3/4 (5mm) Yellow LED with peak emission at 587 mm, 276-320 5mm White LED with peak emission not listed, and 276-041 5 mm Red LED with peak emission at 700 nm.

For the testing, special modules (probes) were constructed for the LED and scintillator placement inside the magnetic field.

4.2.5.1 LED test module

For LED test module, MRS sensor was used, arranged such that the light from the LED was incident directly onto the photosensitive area via small aperture. The sensor was biased at 30.0 V that is well within its operating range. Figure 4.15a is the detailed module photograph, Figure 4.15b shows the photograph of the module assembled, and Figure 4.15c shows its schematic.

The light pulse was produced by the easily changeable LED. The pulse from the pulse generator was ~30 ns wide. Different amplitudes for various LEDs were needed. The output of the MRS sensor was measured and recorded by Agilent [27] Infiniium 54832D MSO oscilloscope without additional preamplifier. The module was placed between the poles of the magnet in a fashion similar to shown in Figure 4.16b.

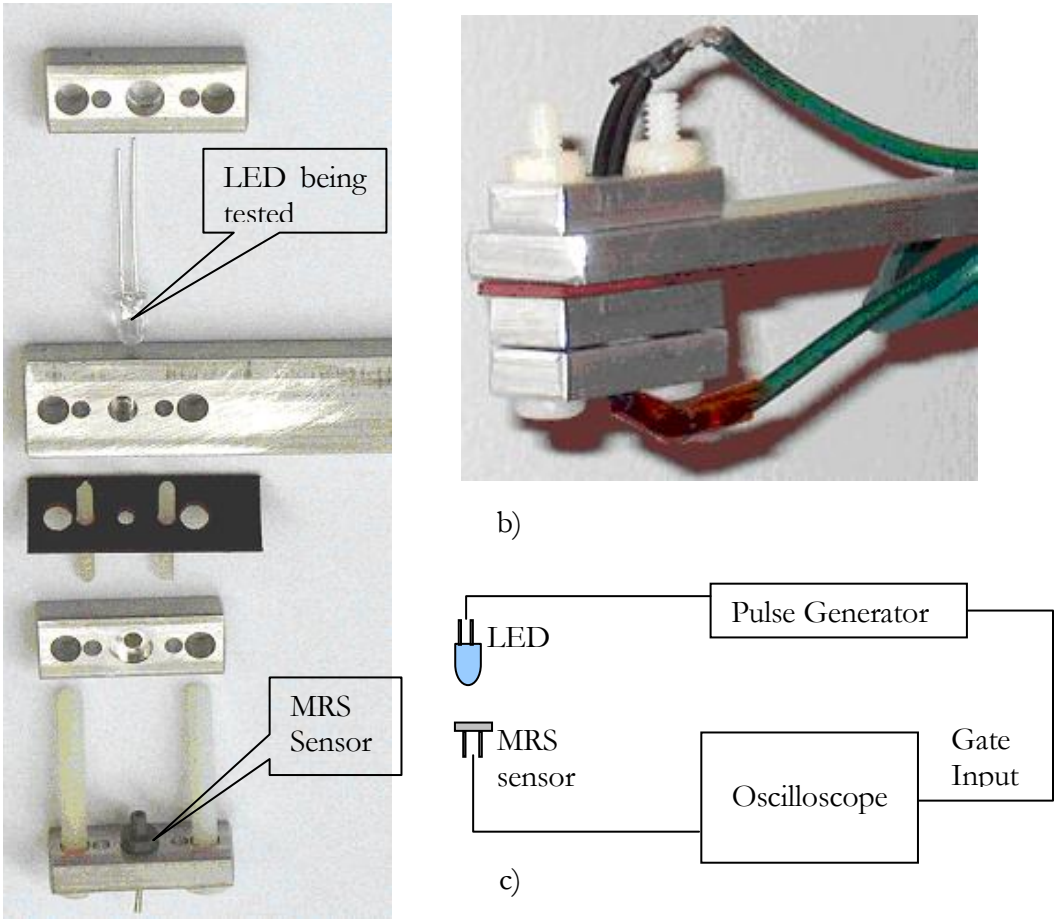

Figure 4.15: a) LED module details; b) LED module assembled; c) LED module schematic.

4.2.5.2 Scintillator test module

For the scintillator test, 10 cm x 2 cm x 1 cm extruded scintillator [12] bar covered by reflective material was used. The KURARAY [10] multiclad Y-11 1mm outer diameter WLS fiber was inserted into the co-extruded hole, also Bivar [20] UV LED and the MRS sensor were used, arranged such that the light from the LED was incident directly onto the scintillator only. This way, the WLS fiber would pick up the light only from the scintillator itself and not from the UV LED. The MRS sensor was placed in contact with the free end of the fiber, and was biased at 30.0 V that is well within its operating range.

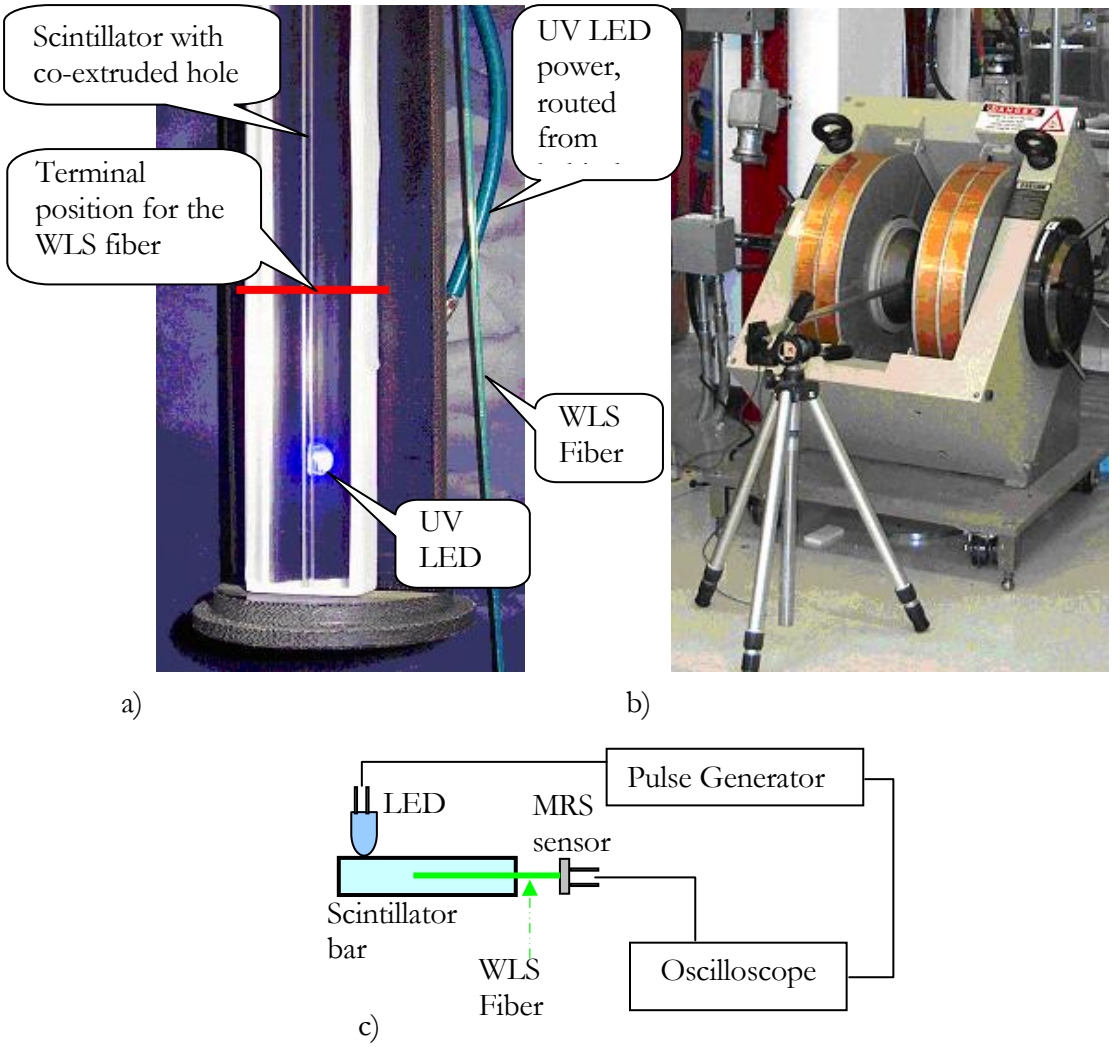

Figure 4.16: a) Scintillator module. Red line indicates the terminal position of the WLS fiber when inserted; b) Scintillator module between the magnet poles; c) Scintillator module schematic.

Figure 4.16a shows the photograph of the scintillator module with WLS fiber not inserted. Note that the fiber terminal position was above the LED and is indicated by the red line on the figure. Figure 4.16b shows the module between the magnet poles. Figure 4.16c shows the schematic of the module.

The pulse to the LED from the pulse generator was ~30 ns wide. The output of the MRS sensors was measured and recorded by Agilent [27] Infiniium54832D MSO oscilloscope without additional preamplifier.

4.2.5.3 LED testing results

The data for all LEDs listed were obtained. Because of the similarity of the results, data only for Bivar UV LED will be presented for illustrative purposes. Bivar LED is of special interest since it doesn't change the spectral characteristics of its light output with change in current [32], thus it has been chosen for PØD Light Injection system.

Here, the field is perpendicular to the LED. The amplitude and the area of the output were measured. Measurements were carried out at 0T, maximum field, 0T, maximum field again, 0T, etc. The repeated measurements at 0T are conducted in order to eliminate unknown factors like the possible temperature or time changes during the experiment. In addition, the field was increased and decreased as fast as possible. Figure 4.17 is the superposition of the MRS output for Bivar UV LED at 0T and successive measurement at 2.3 T. The full output amplitude is ~124mV in both measurements, with area ~ 4.7 nVs.

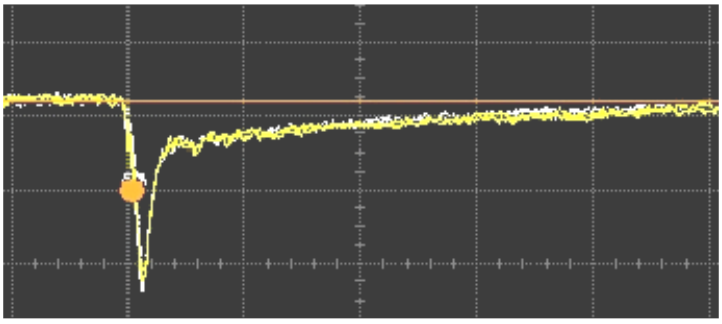

Figure 4.17: Superposition of the outputs at the field strengths of 0 T (white) and 2.3 T (yellow). The scale is 50 mV per cell on vertical axis and 50ns per cell on horizontal.

From Figure 4.17, there are no immediate indications of differences in the output that could be easily seen by the eye. Figure 4.18 shows the values of the area of MRS output for Bivar UV LED different magnetic field strengths. The area is a measure of total charge of the output with a 50 Ω load that is dependent on the total amount of incident light. Each point is an average of at least few hundred measurements. The errors are given directly by the oscilloscope. The biggest difference between points at 0 T and 2.3 T is ~1% that is within the measurement error.

Figure 4.19 shows the values of the amplitude of MRS output for Bivar UV LED at different magnetic field strengths. The amplitude is a measure of the peak current of the output with a 50 Ω load that is dependent on the peak light output from the LED. The maximum of ~1% change in output amplitude between field strength values 0 T and 2.3 T is observed.

Similar results are observed for the field being parallel to the UV LED (due to module dimensions (Figure 4.15b), the maximum achievable field was 1.8T for this test). Analogous results (Table 4.2) are observed for Lumex and Radioshack LEDs in the perpendicular field (2.3 T) as well. Note that sometimes the maximum value of output will be at 0 T and sometimes at 2.3 T.

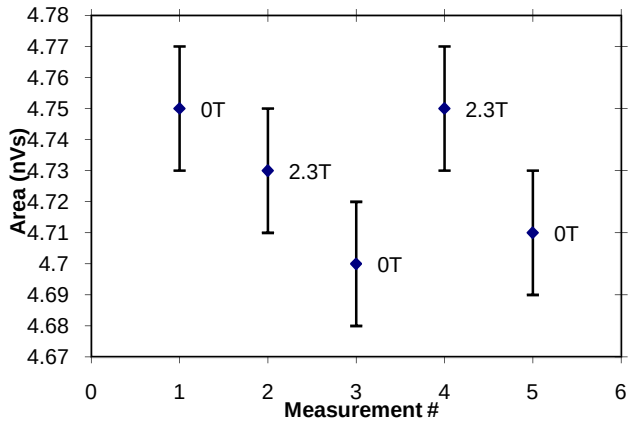

Figure 4.18: Area of the MRS output for Bivar UV LED.

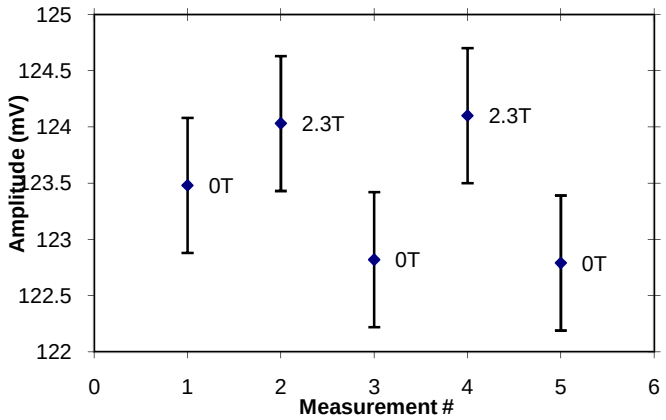

Figure 4.19: Amplitude of the MRS output for Bivar UV LED.

Table 4.2: LED response change in the magnetic field.

LED TESTED	CHANGE IN OUTPUT (%)	COLOR
SSL-DSP5093USBC	1.4	Blue Superbright
SSL-LX5093UPGC/C	0.7	Green Suberbright
276-351 T-1-3/4	1.6	Yellow Bright
276-320 T-1-3/4	1.5	White Bright
276-041 T-1-3/4	1.2	Red Regular

In addition, the dependence of LED light output on temperature was conducted using the Bivar UV LED with constant amplitude pulses (not current pulses). For this measurement, a setup similar to one in Figure 4.15c was used. The differences were that a Hamamatsu R-580 Photomultiplier (PMT) was used, and LED and the PMT were at some distance from each other, aligned in a way such that the LED would shine directly upon the photosensitive area of the PMT. The PMT was biased at 900 V for increased stability. The LED was placed on the heating element with temperature being monitored at the LED itself. At each measurement point, few minutes were given for temperature inside LED to stabilize. The result of this measurement is shown in Figure 4.20. Note that a source of constant pulse amplitude was used to power LED, and not a more commonly used current course.

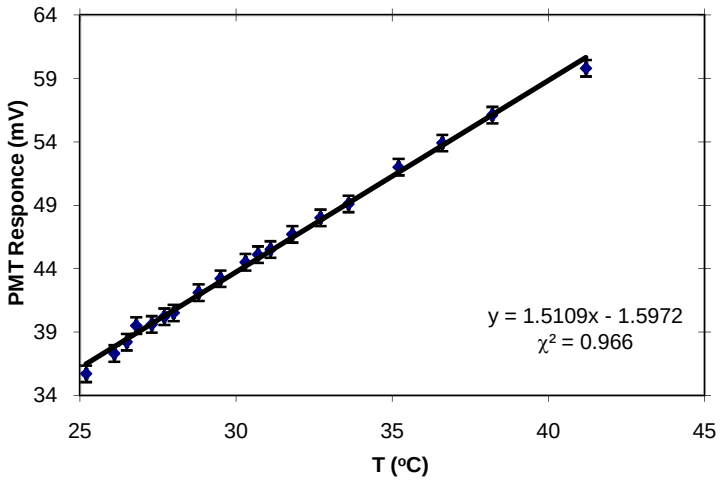

Figure 4.20: Light output of the UV LED as measured by the PMT vs. temperature.

Measurements performed using various LEDs in the magnetic field point to the insensitivity of the LED's light output on the field strength of up to 2.3 T within 1%. This result allows using UV LED in conjunction with MRS sensors to measure the properties of the extruded scintillator in the magnetic field.

4.2.5.4 Scintillator testing results

With UV LED and the MRS photosensor both being insensitive of the magnetic field presence, one can carry out the measurements for the scintillator in the B field. Even though the thorough measurements of various scintillators were done earlier [33], we have carried out the measurements for the newly available and not yet tested in the B field extruded scintillator with the Kuraray Y11 1 mm diameter WLS fiber embedded in the co-extruded hole.

Here, the field is parallel to the LED (i.e. perpendicular to the fiber). The amplitude and the area of the output were measured. Measurements again were carried out at 0 T, maximum field, 0 T, maximum field again, 0 T, etc. The repeated measurements at 0 T were conducted in order to eliminate unknown factors like the possible temperature changes during the experiment, since no thermometer was used to check the temperature. Time was given for temperature to stabilize inside

the module (~20 minutes), but some temperature shift is still unavoidable, in part due to the fact that the temperature of magnet and water cooling is not constant while working. Figure 4.21 is the superposition of the MRS output for extruded scintillator at 0T and successive measurement at 1.8 T. The full output amplitude here is ~129 mV in both measurements, with area ~ 8.4 nVs.

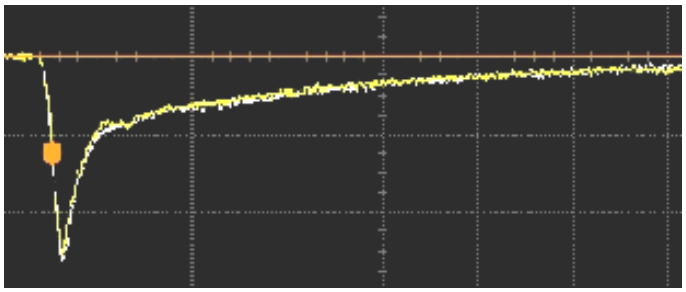

Figure 4.21: Superposition of the outputs at the field strengths of 0 T (white) and 1.8 T (yellow). The scale is 50 mV per cell on vertical axis and 50 ns per cell on horizontal. Due to technical reasons not all the cells might be visible.

From Figure 4.21 there are no immediate indications of differences in the output that could be easily seen by the eye. Figure 4.22 shows the values of the area of MRS output for extruded scintillator at different magnetic field strengths.

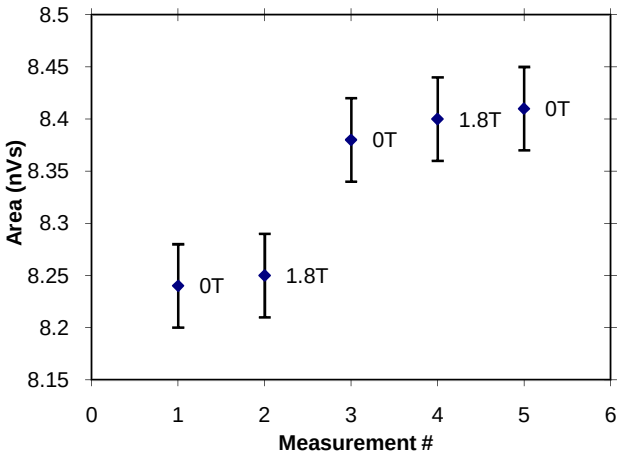

Figure 4.22: Area of the MRS output for extruded scintillator.

The area is a measure of total charge of the output with a 50 Ω load that is dependent on the total amount of incident light that depends on any changes in scintillator properties. Each point in every figure is an average of at least few hundred measurements at each field strength value. The errors are given directly by the oscilloscope. The biggest difference between points at 0 T and 1.8 T is <1%

counting in the fact that between first two points and the remaining three the temperature of the module has changed as indicated by the measurements taken at 0 T, and the difference due to the magnetic field should be calculated using points from each group only.

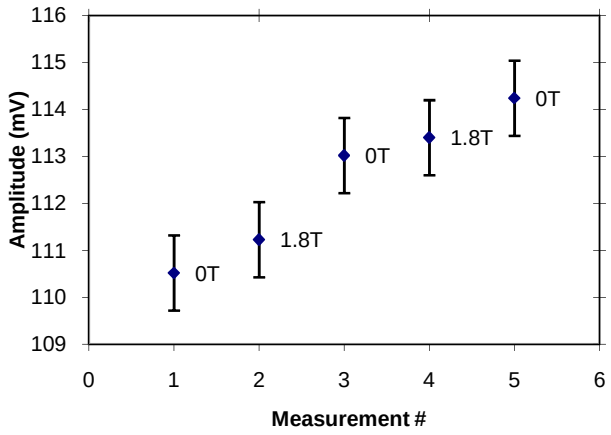

Figure 4.23: Amplitude of the MRS output for extruded scintillator.

Figure 4.23 shows the values of the amplitude of MRS output for extruded scintillator at different magnetic field strengths. The amplitude is a measure of the peak current of the output with a 50 Ω load that is dependent on the peak light output from the scintillator. The maximum of < 1% change in output amplitude between field strength values 0 T and 1.8 T is observed. Once again, the temperature of the module has changed between first two points and the remaining three measurements, and difference should be calculated using points from each group.

The results of this measurement indicate the insensitivity of the light output levels of the extruded scintillator to the magnetic fields up to 1.8 T within 1% when excited by the UV LED.

4.2.6 Sensor-fiber alignment

Due to the fact that the active area of the Silicon family detectors is, in many cases, comparable with the area of the signal-carrying fiber, an alignment issue becomes important. In the case when large number of the scintillator unit cells with such sensors will be produced, the accuracy of the alignment poses constraint on the precision of the assembly of those cells and the automation of the process. In this section, the experimental data on the dependence of the output from 1 mm^2 MRS on the fiber alignment with the sensor is presented. Sensor responses with fiber moving along and away from it were obtained. For all of the following scans, unless stated otherwise, a 0.5 mm outer diameter clear fiber was used, and the sensor was biased at 52 V, chosen following the manufacturer's recommendations.

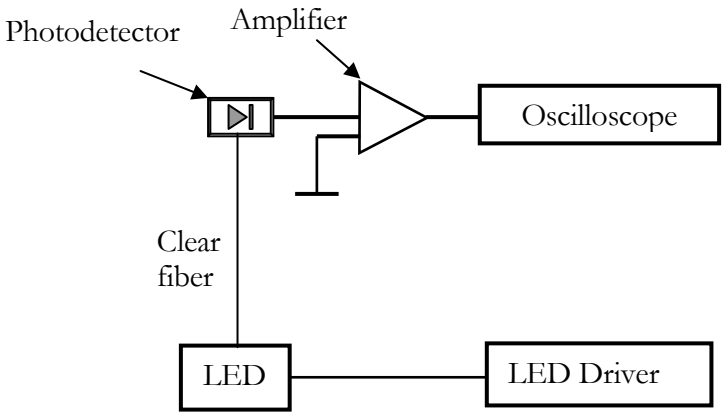

Figure 4.24: Block diagram showing the apparatus used.

A block diagram of the experimental setup used is shown in Figure 4.24. Light signals from the green LED (peak emission at ~510 nm) via a clear fiber were supplied to the MRS and readout was measured using a Tektronix [34] TDS2024 oscilloscope. Position and movements of the fiber with respect to the sensor were accomplished using Newport [35] 462 Series XYZ-M Integrated Linear Stage (Figure 4.25). This Stage allows achieving the linearity of travel better than 100 μrad about any axis and reproducible return to the same point within accuracy of ±2.5 μm.

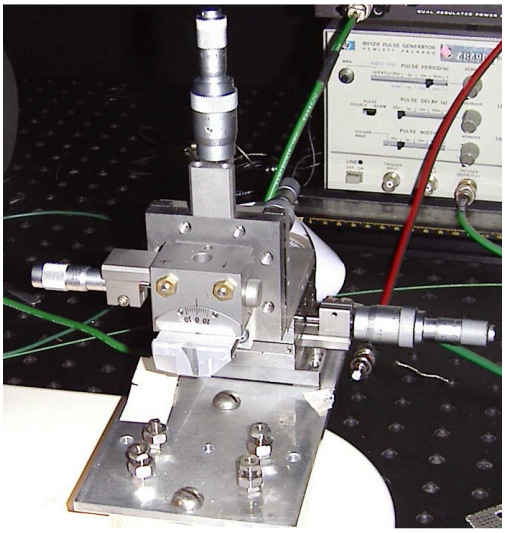

Figure 4.25: 462 series XYZ-M stage.

a)

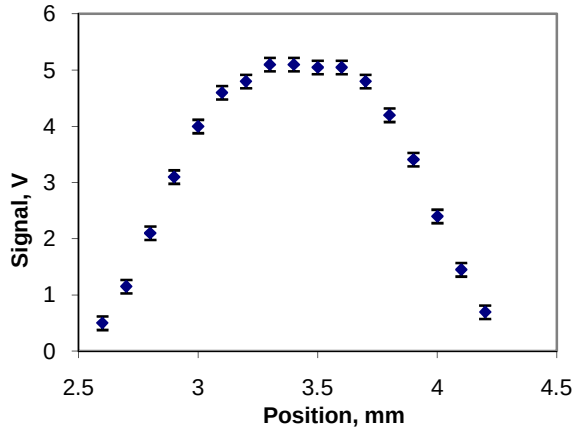

b)

Figure 4.26: a) Sensor orientation and the direction of the scan (indicated by horizontal line). b) Output signal amplitude versus position of the fiber along the MRS sensor.

The result of the scan along the sensor in the direction, indicated in Figure 4.26a, is shows in Figure 4.26b. A plateau corresponds to the region where the entire area of the fiber is within the photosensitive area of the sensor. The tails on the far right and left sides are due to the light reflection off the protective shielding and the mount of the sensor, very small but non-zero value of the response is observed when the fiber moves completely away from the photosensitive area of the MRS. Another contributing effect is due to the fact that fiber is not pressed firmly onto the sensor area so that it could be moved along the sensor without causing surface damage. Hence, as the light signal exits the fiber, it forms a cone with a larger cross-area at the surface of the sensor then the fiber itself would present. Precision of these measurements is approximately ±12 mV at each point. Positioning accuracy is ±2.5 μm. These values are the same for all further plots.

The measurements of the output signal amplitude versus the distance of the fiber away from the sensor were performed. Figure 4.27 shows the results for this scan. Point at 0mm corresponds to the fiber being physically in contact with MRS surface. Scan was performed with fiber positioned in the approximate center of the photosensitive area of the sensor, well within the plateau region (Figure 4.26b).

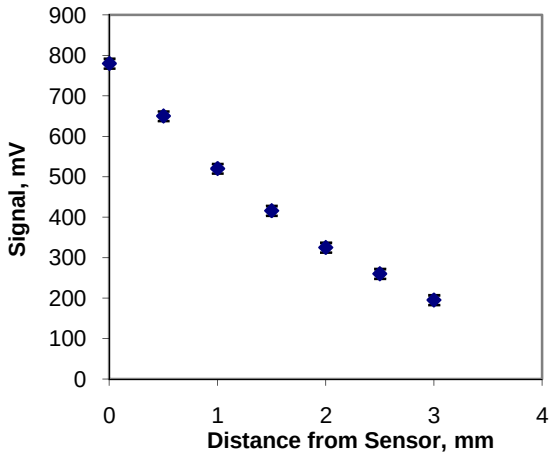

Figure 4.27: Output signal amplitude versus fiber distance from the sensor.

Additional scan along the MRS sensor was performed using the 0.94 mm outer diameter clear fiber in order to see the dependence of the output signal amplitude on the position of the fiber that has the area closer to one used for the readout and, and with the area that is close to the area of the sensor itself. Figure 4.28 shows the result of the measurement with 0.94 mm fiber. Note that there is a peak rather than a plateau. It corresponds to fiber being completely centered on the sensor and is dominated by the contribution from the cladding of the fiber. Information on the further alignment testing with silicon family photosensors can be found in [36].

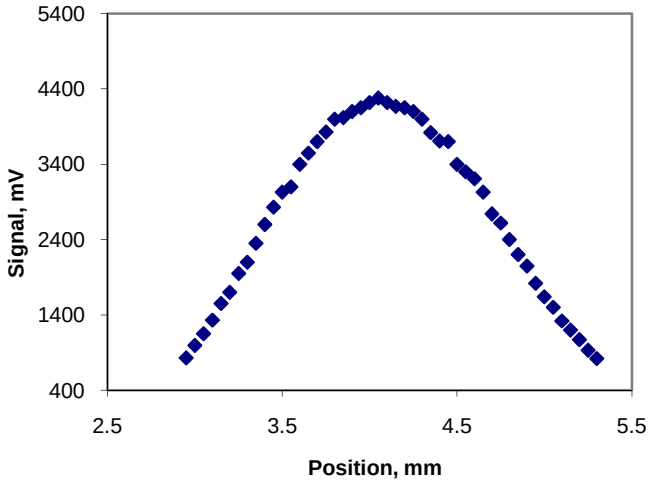

Figure 4.28: Output signal amplitude versus position of the 0.94mm fiber along the MRS sensor. Error bars are not shown so that the structure of the curve is visible.

4.3 MPPC photodetector

MPPC, or Multi-pixel Photon Counter, is one of the latest developments in the multi-pixel detector family by Hamamatsu [14]. The main characteristics for a S10361-050U model at 25 °C are given in Table 4.3, and its photograph under a microscope is presented in Figure 4.29.

Table 4.3: Characteristics for S10361-050U MPPC

Number of pixels	400 [1]
Chip size	1.5 x 1.5 mm^2
Active area	1 x 1 mm^2
Pixel size	50 x 50 μm^2
Pixel effective size	38.1×38.8 μm^2
Geometric efficiency	61.5%
Time resolution	220 ps
Breakdown voltage T coeff.	50 mV/°C
Dark count rate	~5 · 10^5/sec
Gain typ.	7·10^5
Operating voltage	~70V [2]

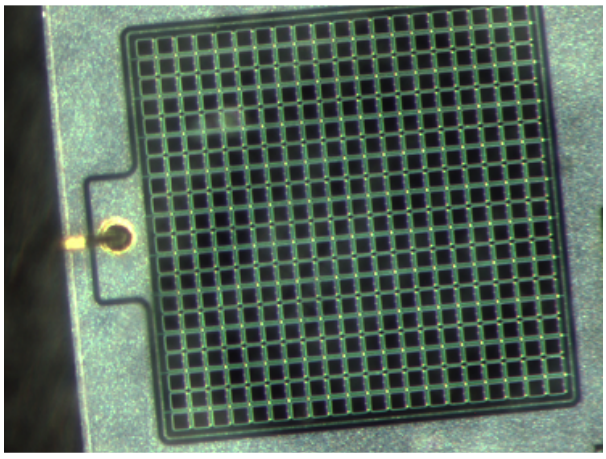

Figure 4.29: S10361-050U MPPC magnified.

[1] a sub-model S10363-050U was produced for T2K with 667 pixels, ~1.3x1.3mm^2 active area

[2] The value varies from sensor to sensor

4.3.1 MPPC Output PE Separation

Since MPPC is a multi-pixel device, with each pixel providing approximately equal output signal, the combined output of the MPPC exhibits a Photo Electron (PE) structure, such as in oscilloscope trace in Figure 4.30 [37].

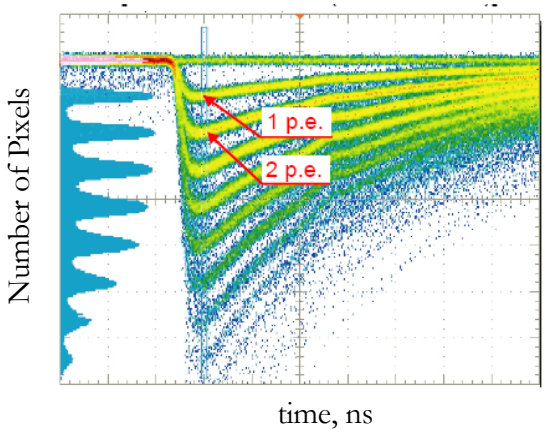

Figure 4.30: MPPC output PE spectrum.

Each line is traced when a single pixel, or two or three fire at the same time. All testing is done at room temperature (~25°C) unless stated otherwise. A similar spectrum measured by Analog-to-Digital Converter (ADC) is in Figure 4.31. This figure was obtained by flashing LED at low light level directly onto MPPC surface. The first peak is the pedestal; the second peak is a single fired pixel, with each subsequent peak representing an additional pixel fired. Here, several peaks are still clearly discernible, thus this photodetector feature can be used for the convenient calibration of the MPPC output.

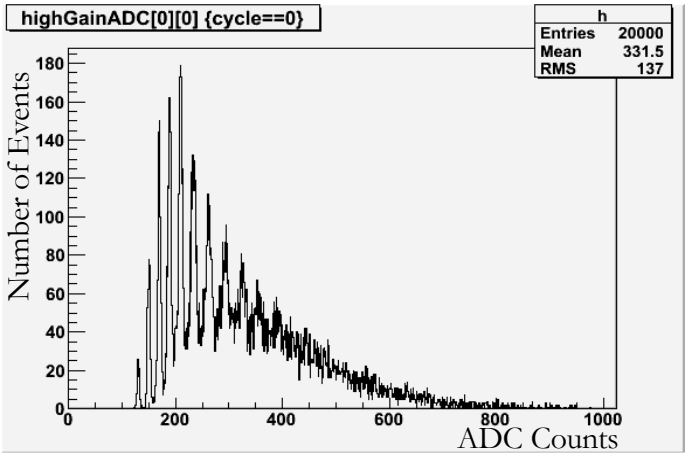

Figure 4.31: ADC spectrum of MPPC PE output.

4.3.2 PDE, Afterpulsing and Pixels Cross-talk

MPPC output has the following features that arise from its multi-pixel structure and avalanche amplification scheme. These are the cross-talk between the pixels and the afterpulsing of the pixels.

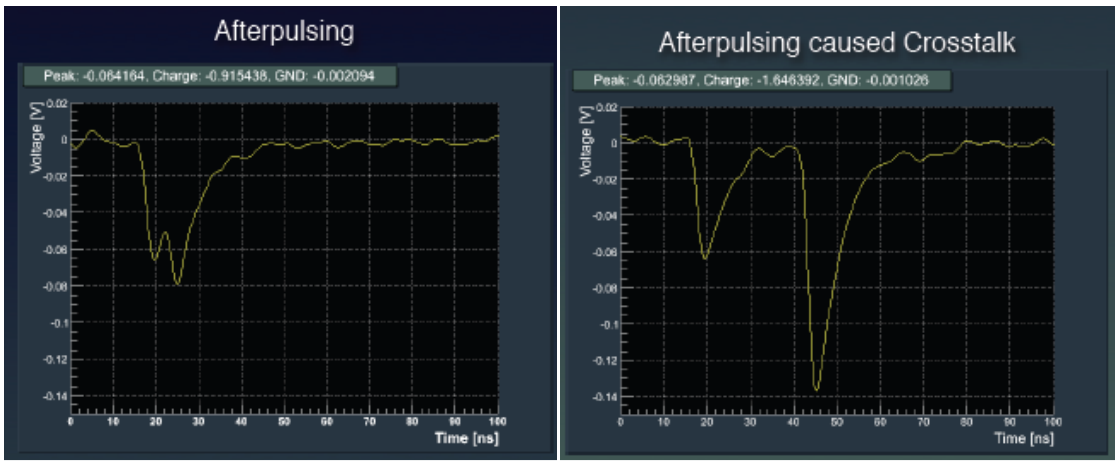

Figure 4.32: (left): Afterpulsing effect; (right): Crosstalk cause by afterpulsing.

Cross-talk occurs when, from a pixel firing from the signal detection or a dark noise, an electron or recombination photon reaches some neighboring pixel and causes it to fire effectively simultaneously. The probability of cross-talk acts as additional amplification in a sense, however, needs to be understood for detailed output understanding.

Afterpulsing is the same pixel firing shortly after it had fired due to the signal detected, dark noise or cross-talk. In majority, this is due to the electrons that get trapped on the impurities and structure defects in the pixel structure, and can cause an avalanche later. A typical lifetime of such trap states ranges from several ns to a couple of hundreds of ns. A pixel needs a certain recovery time after firing so that it can support full avalanche again. If afterpulsing occurs before that time, the output will be of partial amplitude as in Figure 4.32(left) [38]. Afterpulsing, in turn, can cause crosstalk. Figure 4.32(right) [38] shows when a full-size amplitude afterpulse causes a crosstalk of the same amplitude.

Figure 4.33(left) [38] shows the full trace of the MPPC dark noise output. The afterpulse and cross-talk are clearly visible; in Figure 4.33(right) [38] one can notice the amplitude change in the afterpulses. These can be fit [38] with double exponent to get two recovery times:

- Short time const - ~19 ns
- Long time const - ~85 ns

After-pulsing probability can also be obtained:

- (short) - ~6.1%
- (long) - ~5.9%

And the cross-talk probability is ~5.7%.

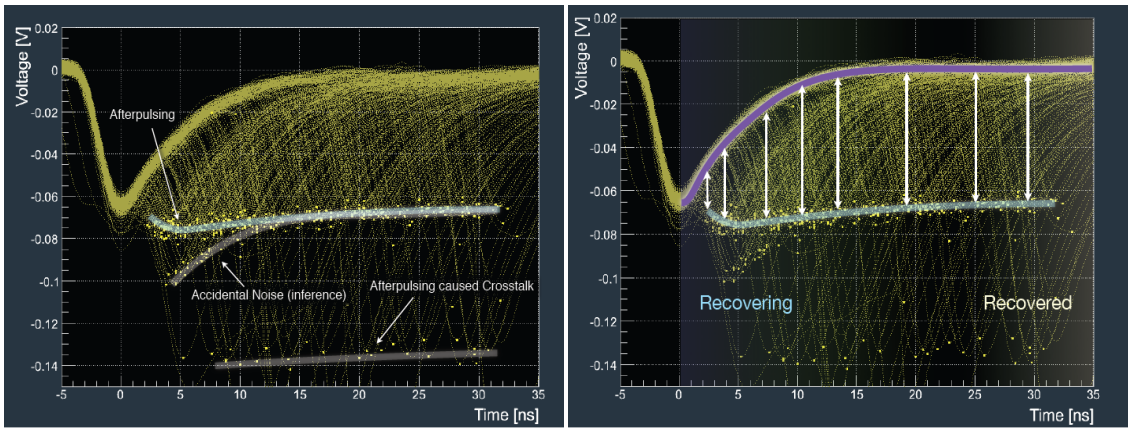

Figure 4.33: (left): Scope trace shows MPPC output structure; (right): Afterpulse amplitude as a function of recovery time.

Temperature and bias dependence of cross-talk rate was studied. The temperature seems to be a low factor with effect dominated by bias voltage above a breakdown (i.e. voltage at which an avalanche can be sustained in the pixel, denoted usually VB or V_{bd}). Figure 4.34 [39] shows the result of that study.

Additionally, a simple and more visual way for the cross-talk and afterpulse check is presented in Figure 4.35. Here, ~100x amplifier was used. This is a graph of average dark noise frequency (averaged over a minute at room temperature) for different biases at different threshold values of the discriminator. Each plateau length is the amplitude of single PE, the slope at the ends of plateaus shows the effects of afterpulsing (otherwise it would be more vertical, with a slope due mostly to pixel to pixel output variations). Ratios between frequencies of each plateau give the approximate rate of the cross-talk. Note that for some high noise sensors (~1 MHz), the accidental coincidence of different pixels with dark noise may be significant.

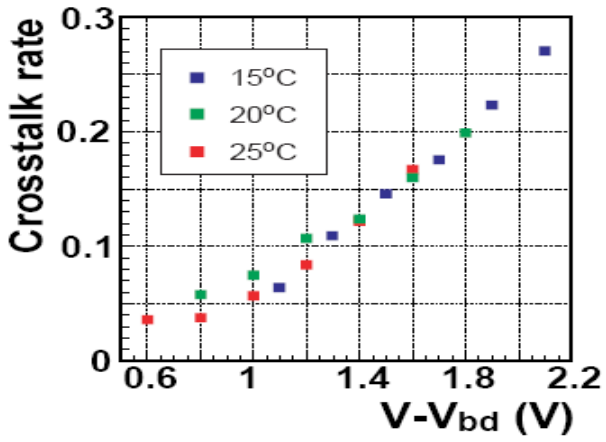

Figure 4.34: Cross-talk rate dependence on biasing voltage and temperature.

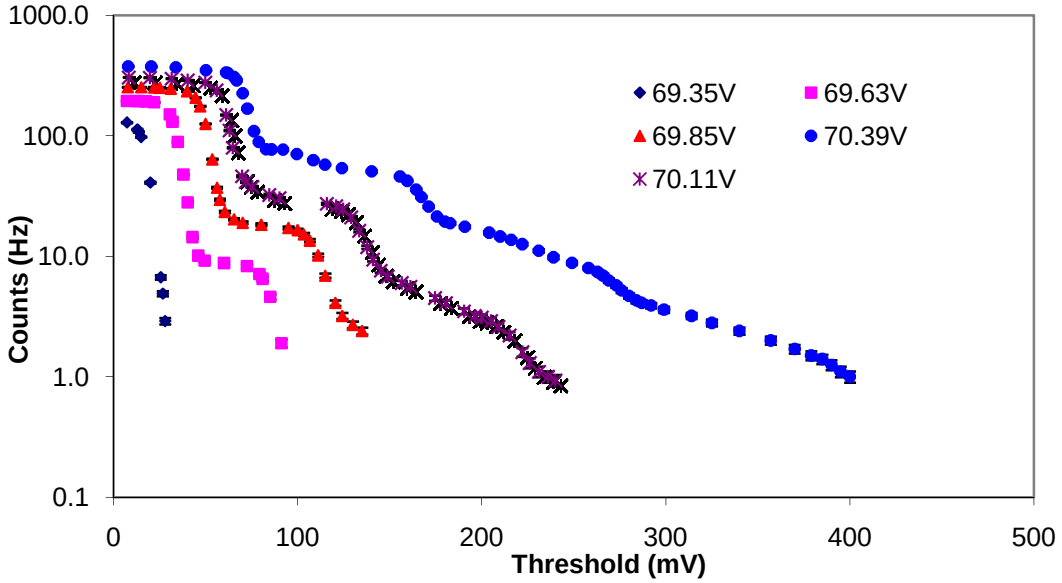

Figure 4.35: MPPC noise rate vs. biasing voltage and discriminator threshold.

In addition, the dependence of the dark noise on the bias voltage and the temperature was measured at threshold of 0.5 PE. The result is presented in Figure 4.36 [39].

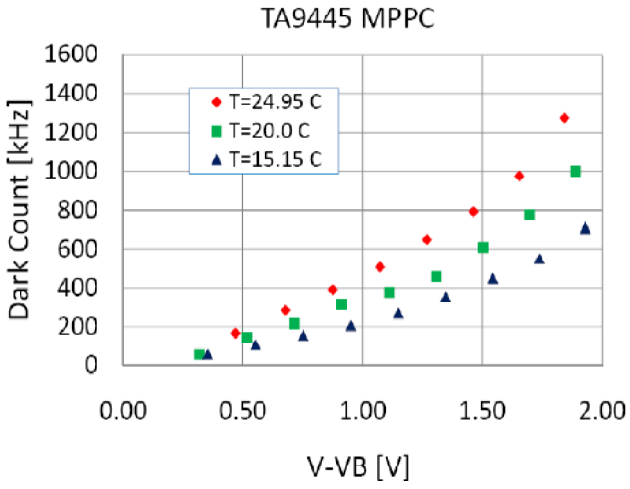

Figure 4.36: Dark noise vs. bias and temperature. VB here denotes breakdown voltage.

4.3.3 Dark Noise, PDE and Gain

The photosensor dark noise rate, gain and Photon Detection Efficiency (PDE) dependence on temperate and biasing voltage were studied.

The dependence of gain on biasing voltage and temperature is shown in Figure 4.37 [40]. The temperature coefficient of bias change with T here is ~ 50 mV/°C.

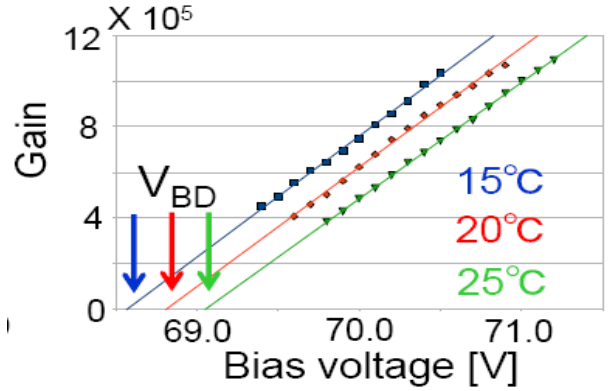

Figure 4.37: MPPC gain vs. biasing voltage and temperature.

Figure 4.38 [39] presents the measurement results for the dark noise rate at 0.5 PE threshold dependence on the temperature and biasing voltage. For a single PE, Figure 4.39 shows the amplitude growth with biasing voltage, measured at 50 Ω with ~100x amplifier.

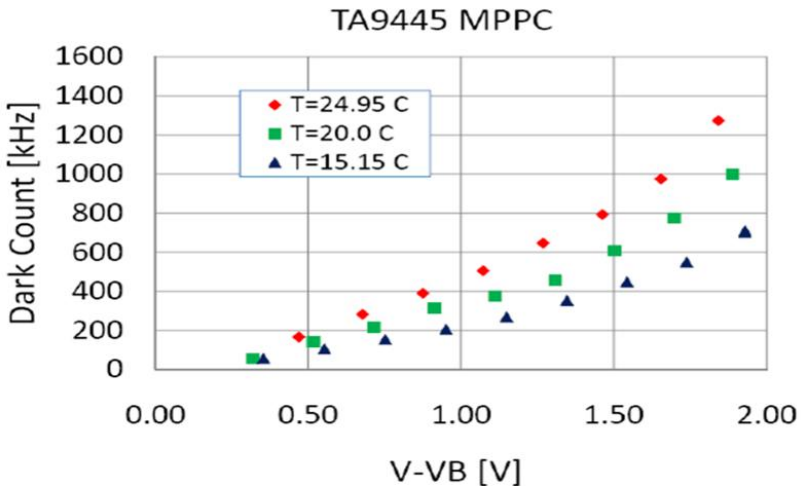

Figure 4.38: Dark noise rate dependence on the temperature and biasing voltage

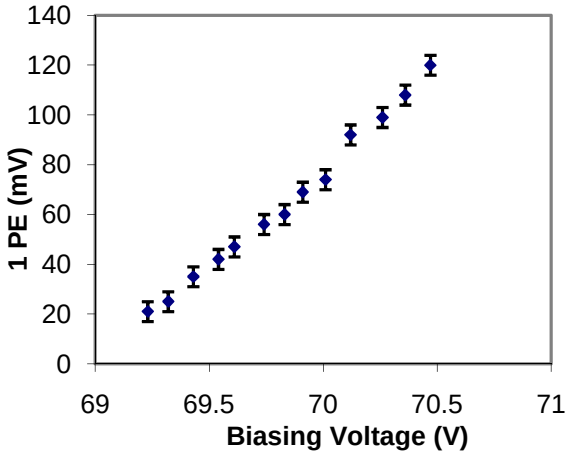

Figure 4.39: MPPC single PE amplitude vs. biasing voltage.

Figure 4.40 [39] is the PDE of the sensor vs. gain at 470 nm (that is linear with bias voltage). The bottom and top lines in the figure illustrates the difference of the apparent from intrinsic PDE caused the effects of cross-talk and afterpulsing. Thus, afterpulse and cross-talk act to increase the apparent sensor output. No noticeable change of PDE with temperate has been observed [39].

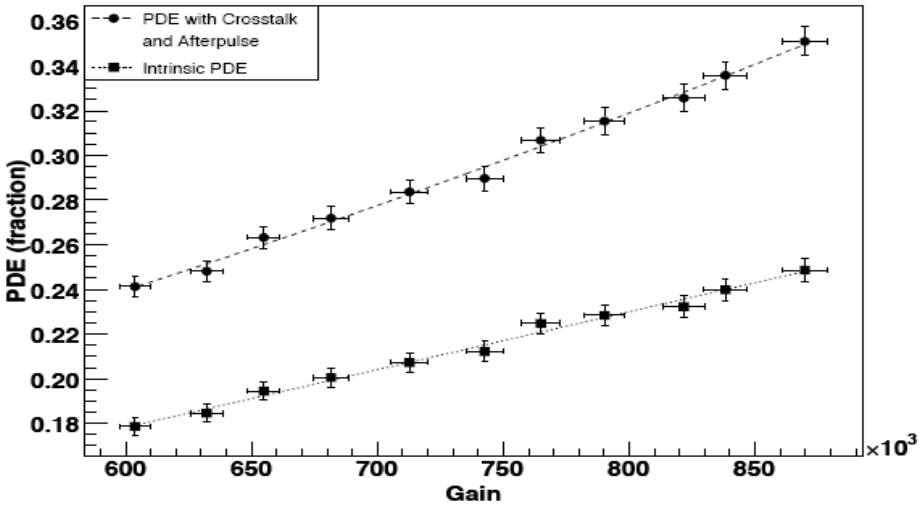

Figure 4.40: PDE vs. MPPC gain.

With bias, the dark noise rate grows, so it's not practical to use these sensors at the upper bound of the operating range. In addition, as bias increases, the PDE, cross-talk and afterpulse increase as well (Figure 4.41).

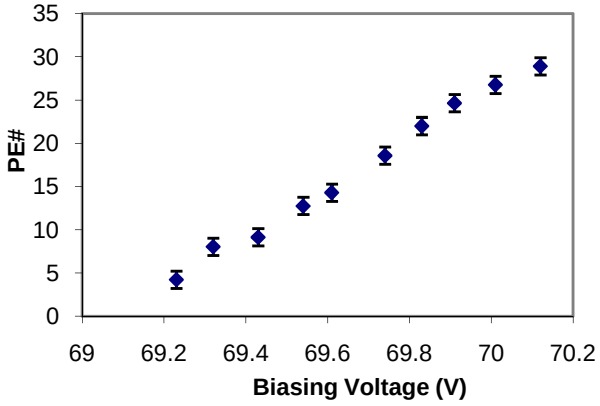

Figure 4.41: Signal amplitude in PE vs. biasing voltage.

PDE is strongly dependent on the wavelength of the incident light. This dependence for MPPC is presented in Figure 4.42 as measured by the manufacturer. When choosing between the Y11 and Y7 WLS fibers (discussed in Section 3.3), this was one of the considerations since the approximate output peak of Y11 fiber is ~490 nm, and ~520 mn for Y7. Thus the choice of Y11 is supported by the PDE argument as well.

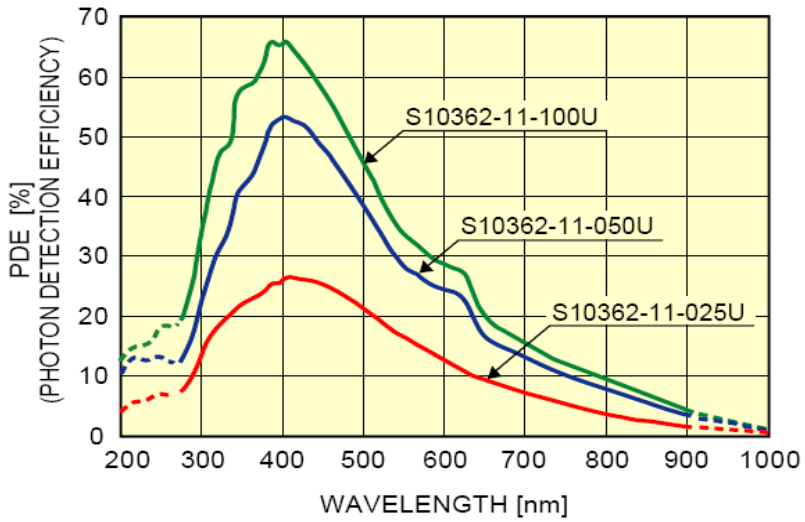

Figure 4.42: MPPC PDE vs. wavelength.

4.3.4 MPPC Linearity of Response

The MPPC has a limited number of pixels. As it is assumed that the incoming photons spread equally over sensor surface, each pixel's output doesn't increase if more than one photon is detected at the same time (or before pixel recovers). This non-linearity of the output to the applied signal vs. bias is illustrated in Figure 4.43 [39] for 400 pixel device.

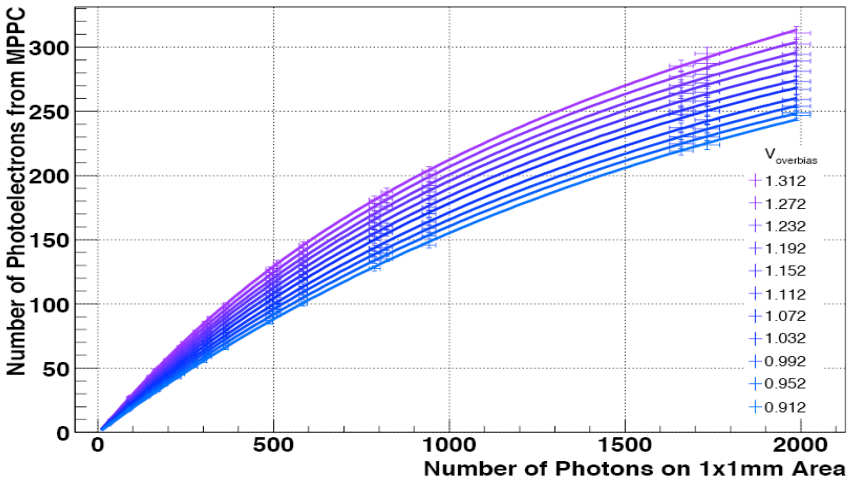

Figure 4.43: MPPC output vs. applied signal for a range of biasing voltages.

This dependence could be fitted by an empirical formula to be used later with the MPPC software simulation package. The simplest form for that formula is presented in 4.14.1. Here Z is the number of PE in the sensor output, N is the MPPC number of pixels (400 for above model), γ is the number of incident photons, and δ is the PDE of the photosensor.

$$Z = Ne^{-\delta\frac{\gamma}{N}} \qquad 4.1$$

4.3.5 MPPC Testing and Deployment with PØD

For PØD, ~11k MPPC were ordered and tested by the PØD group. This testing involved obtaining ADC spectra using LED before sensors installation, dark noise ADC spectra after installation, a signal from a radioactive source during each module post-assembly scanning, and dark noise spectra again after shipping the detector to Japan. During initial testing, approximately 14 sensors were found to be bad, 2 with damaged surface. Four more sensors were replaced for various reasons after testing in Japan.

Figure 4.44 is the spread of biasing voltages among all PØD MPPC sensors [41]. The biasing voltage values on the x-axis are the manufacturer recommended ones.

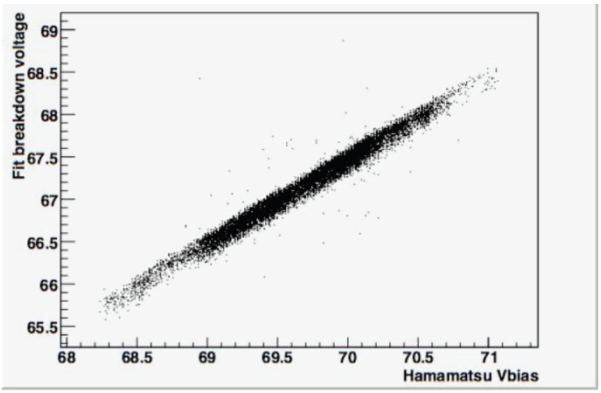

Figure 4.44: MPPC biasing voltage spread for ~11k sensors.

As additional testing, PØD runs with cosmic rays have been carried out in Japan. An average PE output from each scintillator bar (~17 mm active material, averaged over bar length) was ~20PE/MeV. This testing will be discussed further in PØD calibration.

4.3.6 MPPC Output Software Simulation

As a part of the simulation software package used for PØD, there is a software simulation of electronics components that converts the energy deposited by a particle in the scintillator into the PE output of the photosensor. This section briefly describes the functioning of the simple and fast version of this simulation code. This code was intended for use with cosmic rays simulation and is designed to process small to intermediate signals (that is up to ~300 PE in the output). For larger signals, the simulated value increasingly deviates from the supposed value due to simplifications used in the code.

The first step is to recover a number of photons incident onto the photosensor surface using the position along the scintillator bar and the value of energy deposited. This is done using the experimentally determined sensor PE output from a known position along the bar, corrected for average values of dark noise and cross-talk, and using equation 5.3 to correct for the position. Then this value is multiplied by the PDE to recover "true" number of incident photons.

For each incident photon, a random number is drawn with the number accepted being within the value of PDE. Then dark noise is added by picking a Poisson random number with a mean of integer of probability of dark noise occurring during the integration gate of the ADC (that is, the integer of noise_rate/gate_width). Next step is to simulate the cross-talk. Since not only the original pixels can produce crosstalk, but also the ones that were fired due to crosstalk itself, a loop is carried out a number of times equal to an integer part of ADC_gate/pixel_recovery ratio. In the first loop run, the pixels with detected incident photos and with dark noise have a chance to crosstalk and afterpulse using the probability for these processes to occur. In the subsequent loops, only newly fired pixels are allowed a chance to crosstalk, including ones from crosstalk and afterpulsing. At this step, no check is done to limit crosstalk for the case of high signals, when the number of pixels with signal and dark noise is such that the number of neighbors available for cross-talk is limited.

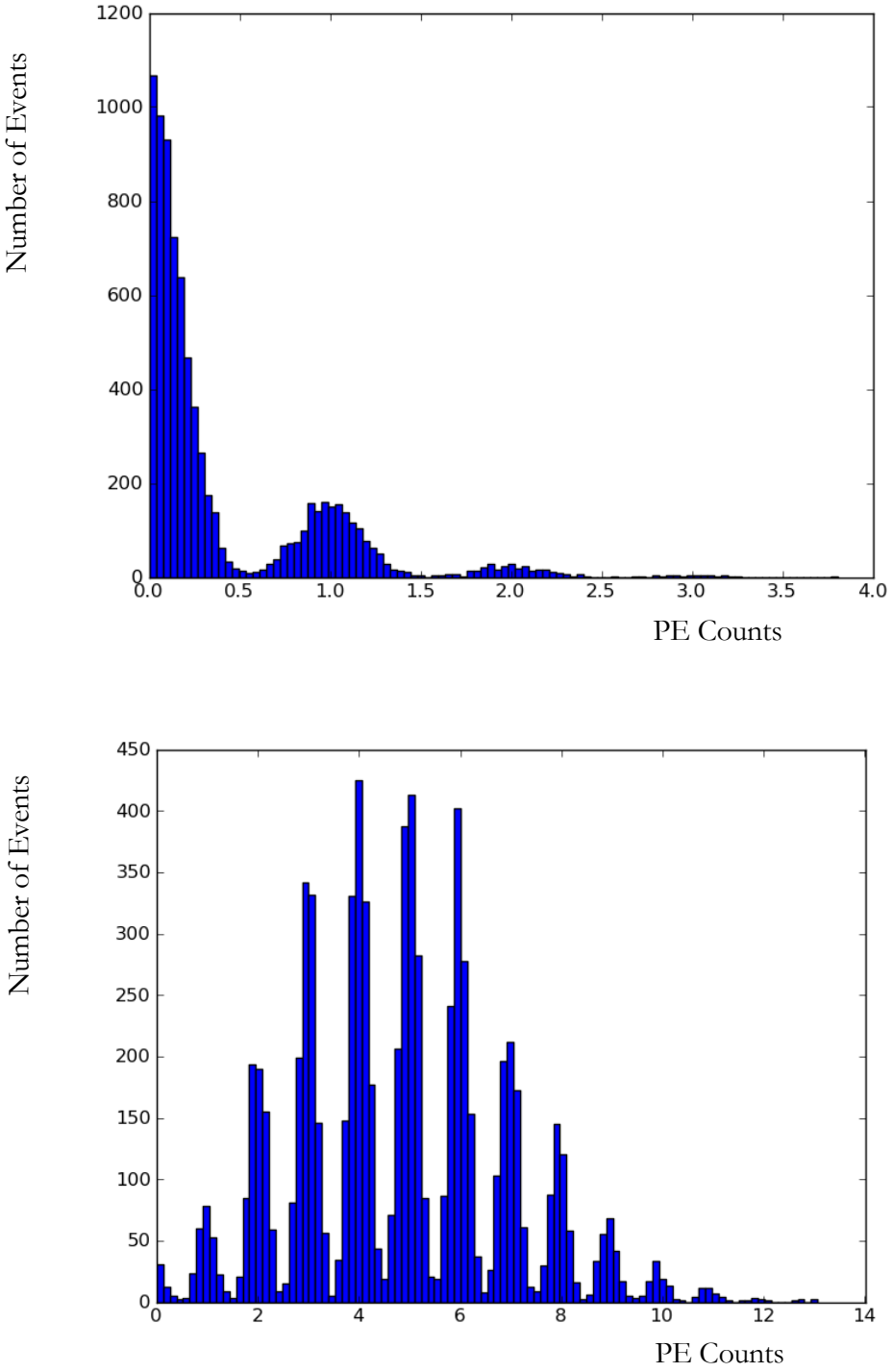

Figure 4.45: MPPC output simulation for 8000 runs with no light signal (top) and with low light signal input (bottom).

Next step is to limit the output of the MPPC due to finite number of pixels. The equation 4.1 is applied to the resulting number of PE from the above steps. This process also limits the errors resulting from the crosstalk calculations for large signals, thus extending the useable energy range with this simulation.

Final step is to include the effects of the ADC and other electronic components. This is done by converting the number of PE into the ADC channels using an average gain value for ADC. Then a Gaussian random number is picked with mean being the above ADC channels, and width picked as obtained from the electronics calibration. Afterwards, the resulting value is converted back into PE using same gain value.

Figure 4.45 shows the sample output of the code with 2MeV input energy at the position of 500mm from the MPPC for 8000 events generated. For the histogram in the figure, 36.35 is the average in units of PE, 6.03 is a square root of the mean, and 5.42 is the standard deviation. The values of standard deviation and square root of the mean are expected to be close to each other but not equal due to the correlated noise such as crosstalk and afterpulsing, and the limited number of pixels on each sensor.

5. PØD COMPONENTS, ASSEMBLY AND CALIBRATIONS

5.1 TFB

TFB, or Trip-t Front End Board, is based on the TRIP-T [42] chipset (each chip with 32 channels). Four of these form 64 input channels, each with low and high gain splits. An amplification difference between the two is ~10 times set by capacitors on the on-board preamplifiers. Each channel is coupled to the ADC, and with each trigger, the signal is read out 23 times (or cycles) using the build-in pipeline. Each readout cycle gate could be from ~100ns to several μs. This is a charge ADC so the expectation is that the charge increases linearly with time with some constant input. However, change is being lost from the storage capacitor during large integration times (Figure 5.1).

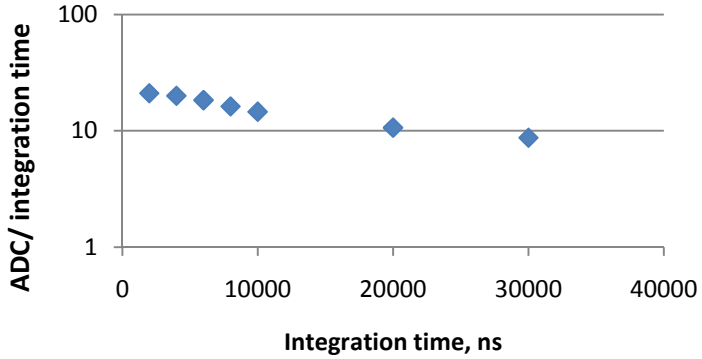

Figure 5.1: ADC output linearity vs. integration time.

The TRIP-t chip itself was designed at FNAL by Abderrezak Mekkaoui, Tom Zimmerman and Jim Hoff as part of the front end of the D0 electronics [43] for the VLPC (Visual Light Photon Counter – it's a APD-like photodetector) based detectors. Its inputs are the analog pulses from the fibers after amplification by the VLPCs and digital timing inputs to control e.g. the time window over which the system should be sensitive to pulses. The outputs of the TRIP-t are: (1) a digital signal to use for triggering; (2) an analog pulse (~1V) that is proportional to the amplitude of the input from the VLPC, called the A-pulse; (3) an analog
pulse (~1V) that is proportional to the time between the firing of the discriminator and the closing of the time-gate, called the t-pulse. The chip contains an analog pipeline just before the final output drivers.

These features allow using both the ADC output for high and low gain channels, but also a timing output that is triggered when a certain amount of charge is reached on each input. The value of this charge and other parameters are uploaded into the chip during the initialization stage from the Data Acquisition (DAQ) system.

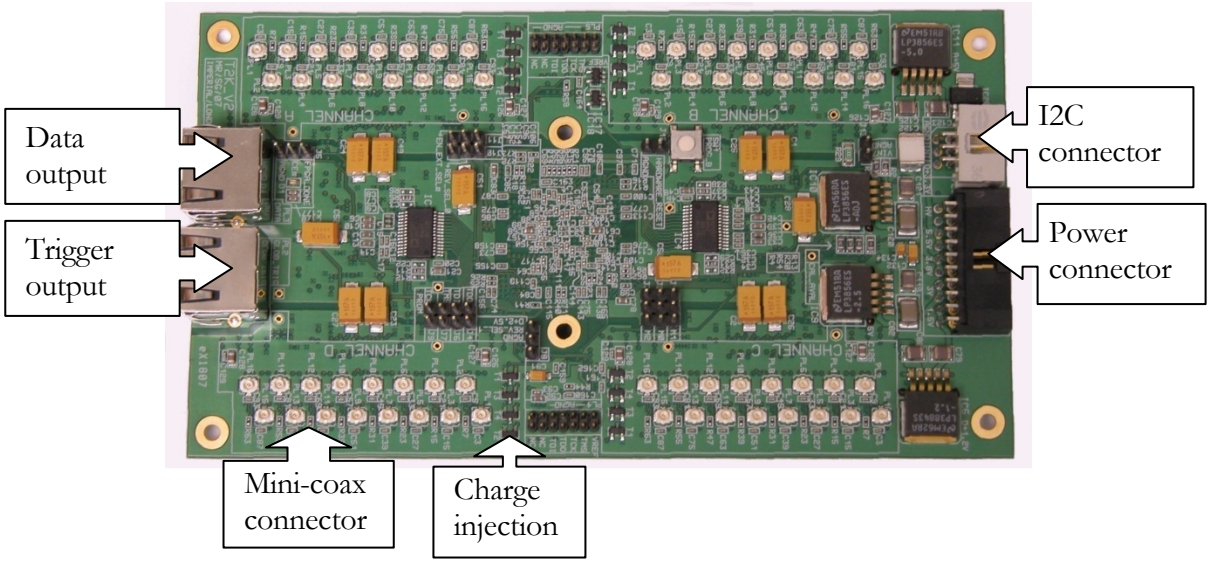

Figure 5.2: TFB Board, top view.

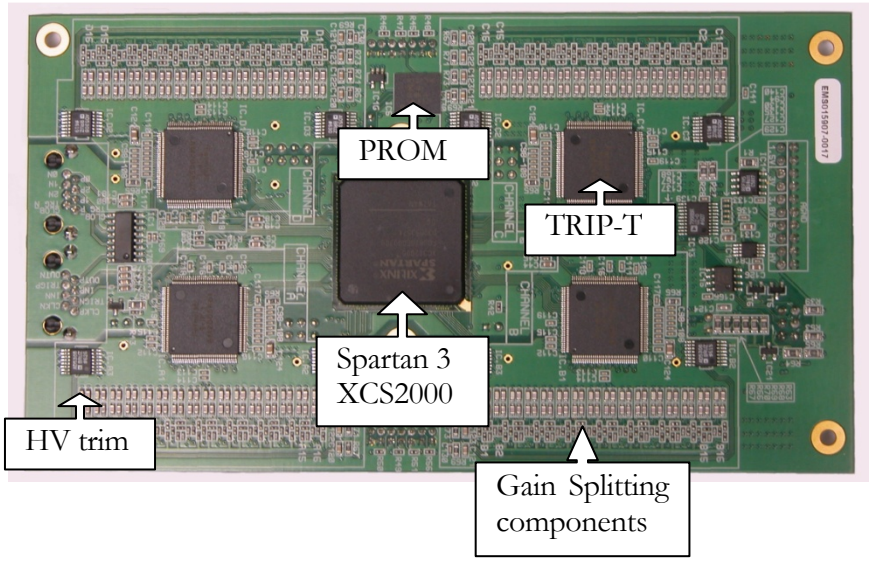

Figure 5.3: TFB Board, bottom view.

The view of the TFB board is presented in Figure 5.2. This is a top view, showing the mini-coax connectors for the MPPCs, charge injection transistors, I2C connector that is used for external temperature sensor readout, power connector for both TFB power and MPPC high voltage, and two RJ45 connectors for data communications and external triggering/trigger output. The other side of the board (Figure 5.3) has four Trip-T chips, XILINX [44] Spartan 3
XCS2000 FPGA (Field Programmable Gate Array) and the gain splitting capacitors for each channel and each preamplifier. In addition, it contains a PROM (Programmable Read-Only Memory) for the FPGA, and the high voltage trim circuit that allows the per-channel MPPC biasing voltage adjustment from 0V or -5V from the supplied value in 256 steps.

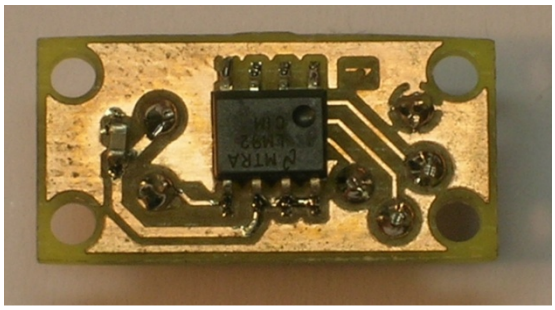

Figure 5.4: LM92 external temperature sensor.

Since MPPCs are sensitive to the temperature, external temperature sensors are used to monitor the temperature of the PØD. Figure 5.4 shows a sample design of such sensor board. These are pasted onto the PØDules (two per each side of every second module, connected in pairs) and are read out using I2C port on the closest TFB.

5.1.1 TFB Charge Injection Calibration

Each TFB channel has a feature called a charge injection system. It is used to inject the programmable charge amount to check for the ADC linearity over the entire working range of charge values. This is used for non-linearity correction of the ADC per each channel, and for time-walk correction.

The ADC nonlinearity is an effect when at high charge the ADC saturates and outputs increasingly smaller value per charge increase. This is illustrated in Figure 5.5.

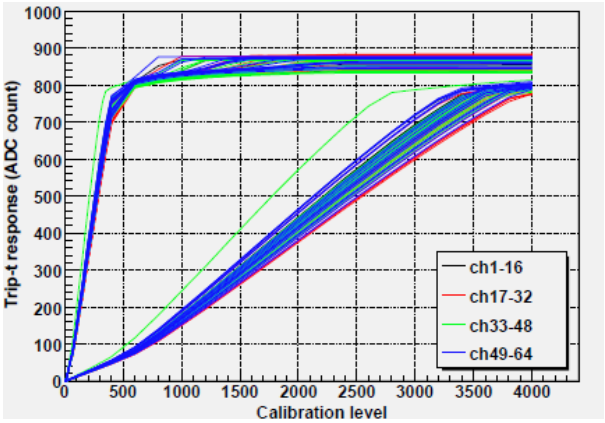

Figure 5.5: TBF ADC non-linearity calibration for high (top curves) and low (bottom curves) gain channels.

Time-walk is a result of the TDC (time-to-digital converter) threshold being reached at different times for signal of small and large amplitude. These data are later fitted to equation 5.1. The example

of the raw TDC data with a fit vs. the injected charge is shown in Figure 5.6. Using the result, the corrected time resolution is shown in Figure 5.7.

$$p_0 + \frac{p_1}{(ADC - Ped)^{p_2}} \qquad 5.1$$

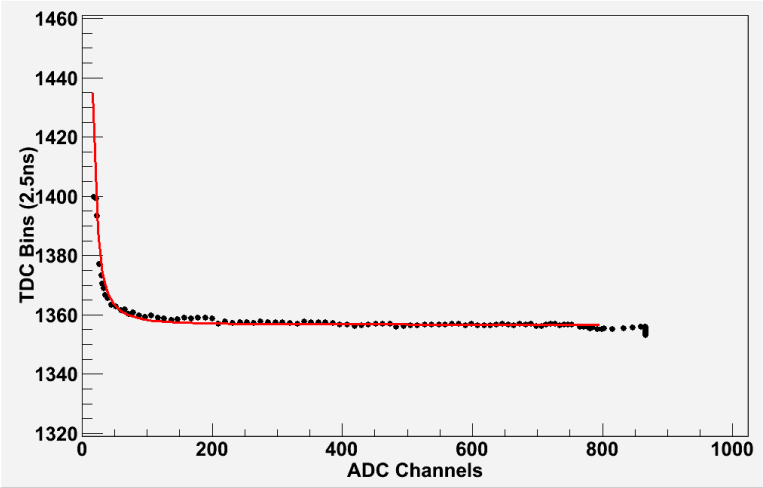

Figure 5.6: Charge injection timing data with a fit curve.

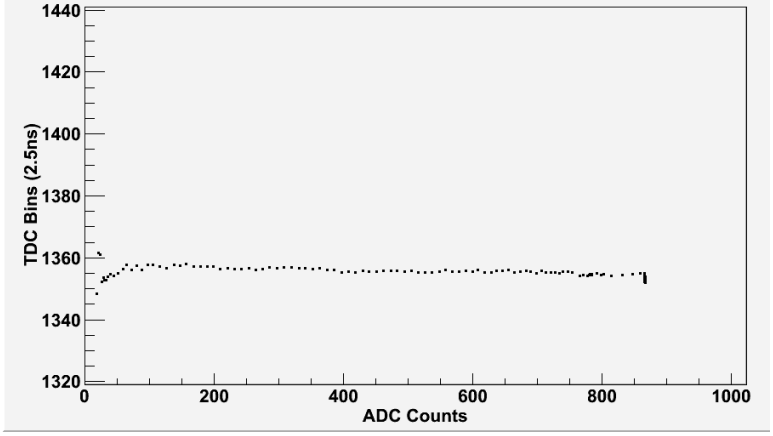

Figure 5.7: Charge injection with corrected timing.

5.2 In-situ Signal Attenuation Calibration

The calibrations explored further in this chapter are the minimum ionizing particle (MIP) energy deposition within the detector's scintillator bars, light attenuation from energy deposition point to the photosensor and the hits efficiency in each detector layer for long muon tracks in PØD. This section deals with the study of light attenuation within a single channel.

For the calibration purposes, long muon tracks are selected. A long track is defined as a track that has a hit in either an X or Y plane of the first and the last PØDule. An average energy deposition is checked to be uniform so that the selected tracks will have muons exiting the PØD and not decaying in the last PØDules.

In addition to the initial light attenuation measurements of WLS fiber, the watch is kept on the total signal attenuation within the scintillator bar together with the fiber. For that, the hit coordinates and energy deposition normalized to the path length of cosmic rays within the scintillator are plotted for each bar in order to obtain the calibration constants to the fit function in equation 5.2 that is the simplified version of equation 5.3. This method also yields the averaged over the bar energy deposition for a MIP.

$$p_0\left(e^{-x/4634} + p_1 e^{(x-2*fiberL)/4634} + p_2 e^{-x/322}\right) \qquad 5.2$$

The parameters for short and long light attenuation are hardcoded for the stability and simplicity of the fit. These are the values used in the software thus achieving the use of the same function both in the simulation of the detector and the calibration of the data. This also reduces number of free parameters allowing the better fit performance on the smaller datasets. These parameters are later used for energy calibration and detector simulation software.

The main purpose of this function is to fit the data, thus p[0,1,2] are just parameters. However, p0 can be related to the average bar amplitude, p1 – to the fiber end-mirror reflectivity, and p2 – to the fractional contribution of the short attenuation component to the total.

The sample fit is presented in Figure 5.8. The parameter values are 16.7061, 0.774 and 0.355, with corresponding errors of 0.33, 0.043 and 0.027. The degrees of freedom (dof) value is 42, and χ^2/dof is 1.19.

5.3 Channel to Channel Light Yield Variation

Using the signal attenuation parameters and the cosmic muons data, it is possible to normalize all the energy deposits from the muons in each bar to a particular point along the bar, and study the spread between the light yield (or, rather, signal output) between all the detector channels. The normalization applied was to adjust all the energy deposits as if they happened at the center of each bar, and take the energy per 1 cm of track length within the bar. This process produced the energy deposition in the center of each bar per 1 cm (~2 MeV). The resultant distribution has two components to it – Gaussian spread from the electronics and other statistical effects, and Landau

distribution for energy deposition in the thin materials. The output for each bar is fitted with a convolution of the two, generically called a LanGaus distribution Figure 5.9 (top).

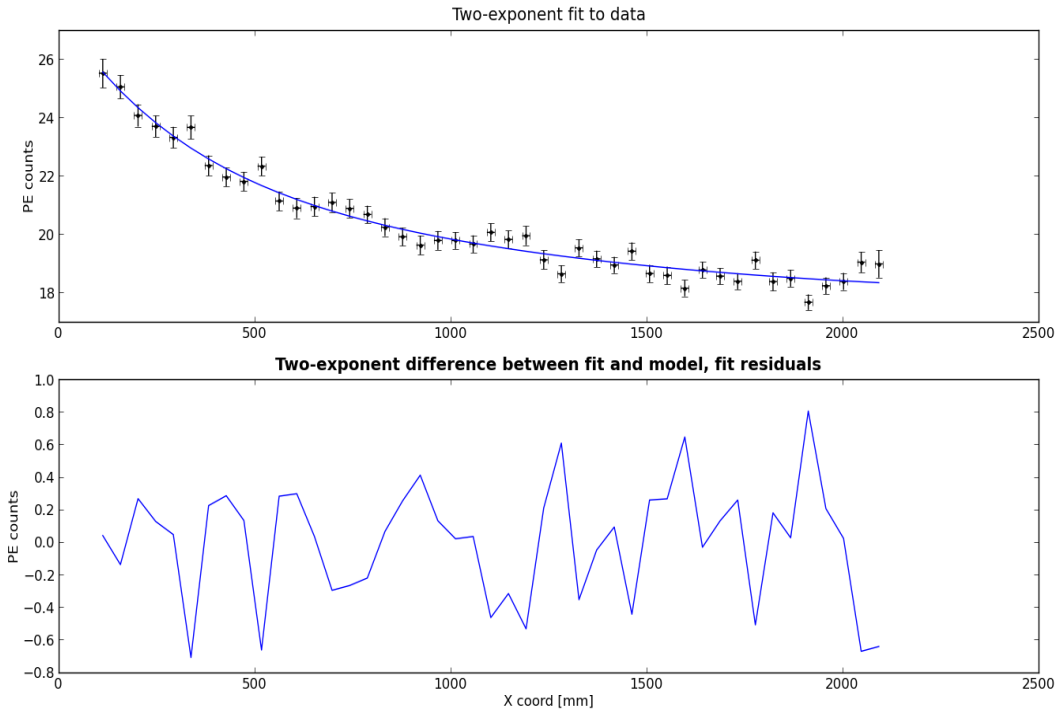

Figure 5.8: Signal Attenuation for a single channel.

The MP values (that is the mean for this type of distribution) for each bar are obtained. Ratios of these are to be used in final energy calibration. In Figure 5.9 (bottom), the sample histogram of such values for different bars is presented with a fit to a normal distribution indicating the spread.

5.4 Detector Layer Hits Efficiency

The calibration described in this section finds the hits efficiency in each detector layer for long muon tracks in PØD. As described before, each module in the detector that consists of a set of X and Y layers is designated as a PØDule. Each X or Y layer is composed of the triangular scintillator bars with purpose of providing a better hit position by means of deposited charge weighting. In the ideal geometry, there are two hits per layer for a track that passed through it regardless of the incident angle and energy deposited. In the real detector, bar shape, alignment and detection threshold may influence the detection of the hit pair.

For this purpose, long muon tracks are selected. A long track is defined as a track that has a hit in either an X or Y plane of the first and the last PØDule (a module set of X-Y planks). An average energy deposition is checked to be uniform so that the selected tracks will have muons exiting the PØD still in the MIP (minimum ionizing particle) regime and not decaying in the last PØDules. In

particular, 'sand' muons (that is muons originating from beam neutrino interactions in the magnet and surrounding concrete and sand) are used rather than cosmic rays due to the abundance of the horizontal tracks in PØD they provide.

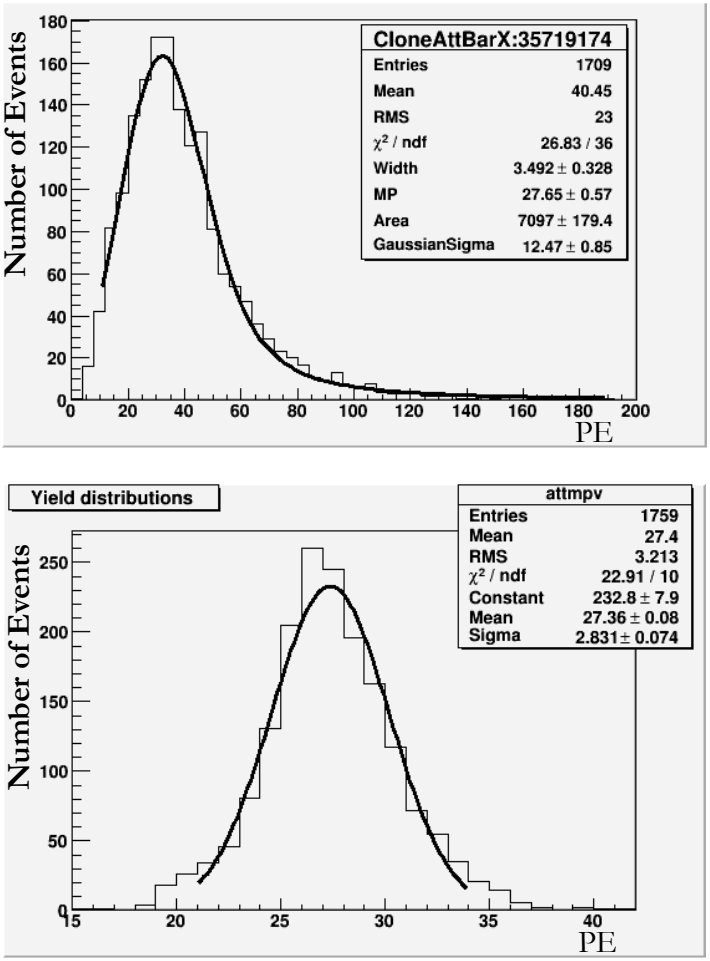

Figure 5.9: (top): LanGaus fit to energy deposition in a single scintillator bar;
(bottom): Spread of fit values between bars.

Data from the available runs were analyzed. The reconstruction information is used to identify the long tracks with at least one hit in both first and last PØDule. Then the search algorithm is run on the track, layer by layer separate for X and Y, to identify the double, single and missing hits.

If a double hit is found in the reconstructed track contained, it's recorded and the algorithm is advancing to the next layer.

If only a single hit per layer is identified by reconstruction information, a search for a missing hit is attempted using all hits for the event. A missing hit may occur in some instances, for example, when the timing of that hit is earlier due to dark noise, if a track has a sharp turn due to scattering, or a bad photosensor. So, attempt is made to find this missing hit with the following criteria: it must be in the

same layer in the bar next to the exiting hit, and within the same integration cycle. If a second hit is found, the occurrence is recorded as a double, or otherwise as a single hit.

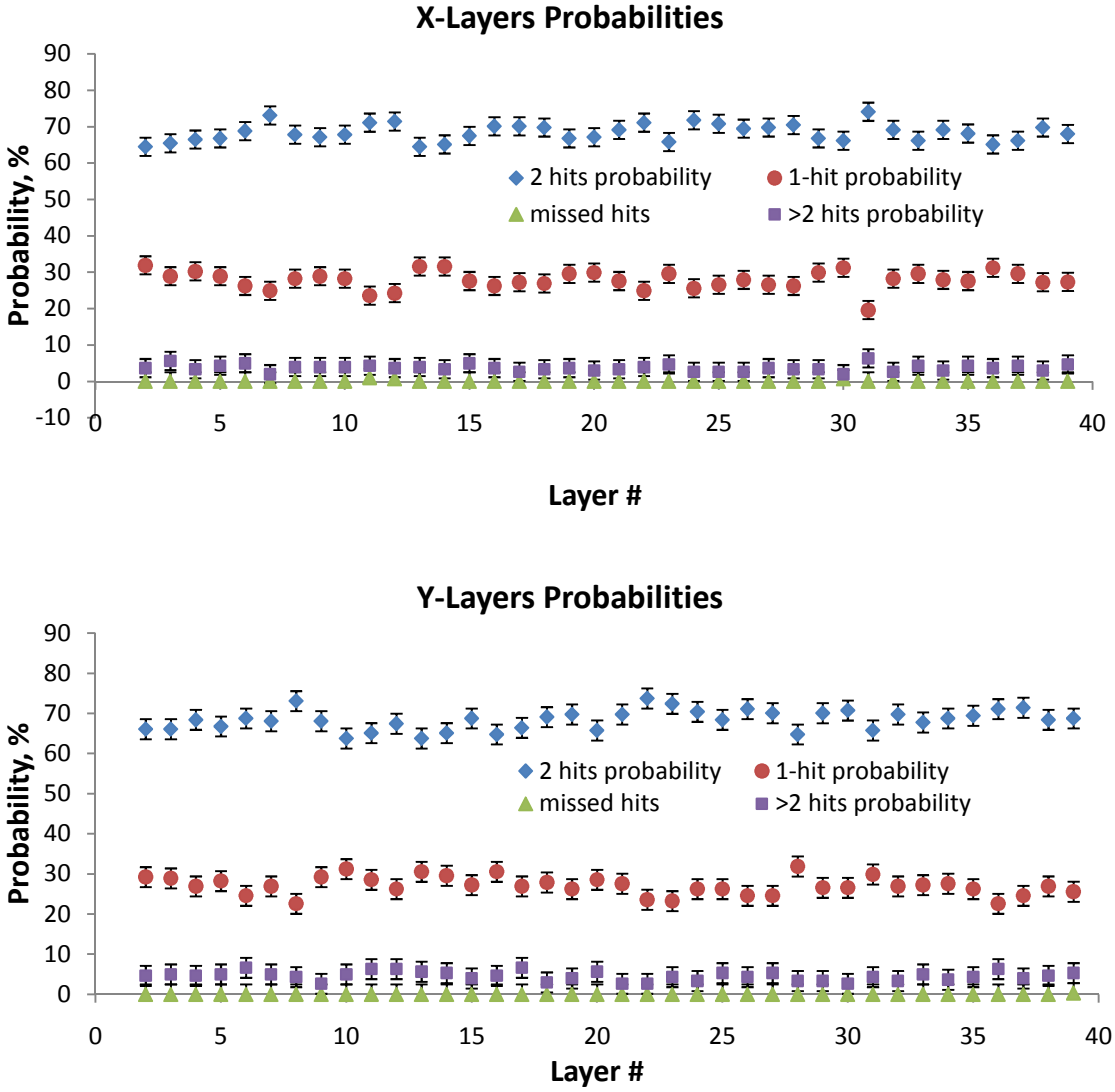

Figure 5.10: The efficiencies of >2, double, single and missing hits for X layers (top) and Y layers (bottom) for PØD.

If a layer has no hits, then a search for a possible skipped hit or hits is attempted. This happens rarely when a muon suffers strong scattering and is reflected at a large angle, a different track has passed previously through the same bars and triggered them with a different time stamp, or a bad photosensor makes a single hit appear farther from the track. In this case, the search algorithm is looking for a single or a pair of hits near the line connecting hits in adjacent layers. If two hits are found, they must be in neighboring bars. The time stamp should be closest to the average time of adjacent hits, with position within several bars (normally no larger than 2-3 bars from the connecting

line). If no hits in the event that match the selection criteria are found, a missing hit occurrence for the layer is marked; otherwise a single or double hit is recorded.

Due to the selection rules requiring at least one X or Y hit in a first PØDule and at least one X or Y hit in the last, the efficiency values are biased for both X and Y layers in those PØDules. Therefore, the results of 4698 muon tracks for only 38 from total 40 PØDules are presented. These are plotted separately for X layers in Figure 5.10 (top), and Y layers in Figure 5.10 (bottom).

The averaged efficiency values for all 38 PØDules are as follows: 4.112% for hits >2, 68.367% for double hits, 27.475% for single hits, and 0.035% for layers with missed hits. The last value agrees with the number of the bad channels in the detector (~15).

5.5 PØDules Alignment

Using the long muon tracks, a check for the PØDule-to-PØDule alignment is done by plotting the residuals from the track fitting in each layer. The results of this study are presented in Figure 5.11[3].

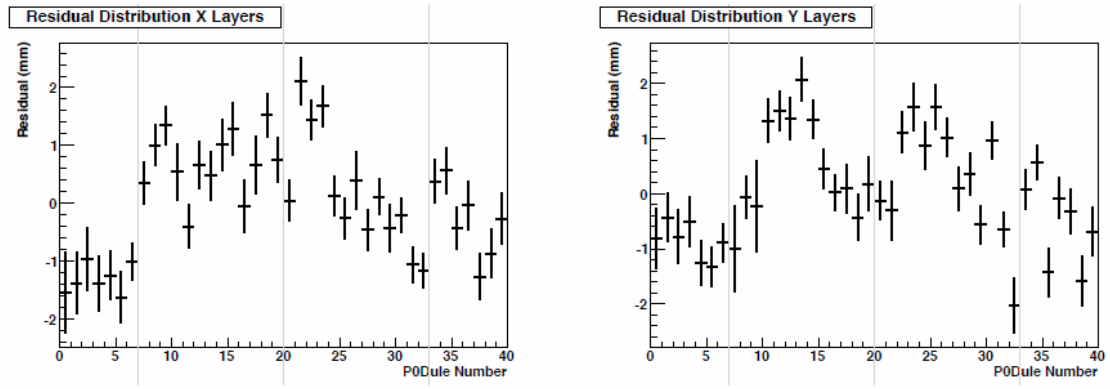

Figure 5.11: Residuals distribution for long tracks in PØD.

5.6 RMM, MCM, CTM and Slow Control

For PØD and other sub-detectors using MPPC photo detectors and TFB-based ADC boards, the following components complete the DAQ system chain:

- Readout Merger Module (RMM)
- Cosmic Trigger Module (CTM)
- Master Clock Module (MCM)
- Slave Clock Module (SCM)
- Computer-based front end readout.

[3] From the work by Karin Gilje

The three modules above are based on a same board design with different firmware and attached connectors. Each has 48 RJ45 network connectors, several Gigabit optical network connectors and power input.

The RMM module allows up to 48 TFB connections via their data outputs. It handles their communications and merges together the data outputs forming the data stream for the computer front end. The CTM module forms a cosmic trigger based on the data from the pre-selected TFB modules that are directly connected to it via their trigger outputs. A simple measure of the total hits in each board and their coincidences forms a cosmic trigger between the detectors (e.g. PØD and SMRD, PØD and DSECAL, SMRD and DSECAL), or between the SMRD towers.

The MCM initializes the time stamp for each TFB via the broadcast through the RMMs. It also issues system-wide triggers such as a beam trigger, pedestal trigger, light-injection trigger and other maintenance or internally used trigger types. It also connects to the GPS time synchronization system for the correct time stamp for the events between ND280 and SK detectors. The SCM duplicates the MCM functionality, allowing each sub-detector to be run in a stand-alone mode.

Slow Control is a monitoring system with a slow, on the order of once a second, readout of the operational parameters and environment conditions. These include but not limited to the MPPC and TPC high voltage lines, electronics power lines, light injection status, water level status in PØD and FGD, TFB on-board temperatures and the external temperature sensors. This data is read via a special slow control system and front end (except PØD water system that has its own line and the TFB temperature sensors that are read via RMMs) and is connected to the alarms system if any of the monitored parameters gets out of the pre-defined allowed ranges.

5.6.1 PØD Electronics Overview

PØD has 6 RMM modules: both ECALs have 1 each, and water targets have 2 each, with 29 TFBs connected to each RMM. This allows some number of channels to be left to be used as spares in the future. These are mounted on the aluminium extrusion cooling loops on top and left side of each SuperPØDule. The cooling system employs a negative-pressure water circulation to avoid leaks in case of any damage.

About a quarter of the TFBs have an external temperature sensor board (Figure 5.4) with two temperature sensors connected to it. These sensors and the TFB on-board temperature sensors are part of the PØD slow control system. Additionally, the bias voltage, the TFB and RMM power voltages and the water levels in the water target region are being monitored as well. The electronics for water level monitoring is mounted on top of water targets between the cooling loops, and it read out via a separate line.

5.7 PØD Prototype Assembly and Testing

A single PØD scintillator module (or PØDule) was built as a prototype using the first batch of triangular scintillator bars available. It was tested with cosmic rays using the provided for testing photosensors and with the electronics available utilizing the external triggering scheme. The assembly techniques were developed using this prototype as well.

5.7.1 Assembly

The process was carried out in three major steps. Arrays (named planks) of 15-17 scintillator bars were pre-made for this assembly. These planks were glued from individual cut-to-size bars in alternating arrangement, as in Figure 5.12, and cured under the vacuum film. This simplifies the PØDule assembly needing only 16 planks vs. 240 individual scintillator bars (126 Y, or vertical bars of 2272 mm length, and 134 X, or horizontal bars of 2133mm).

For all component assembly, a flat-surface gluing table was built. The full PØDule includes two outer PVC skins, eight of each X and Y planks and four PVC frames. The frames are precision machined to have the scintillator location matching holes. There are four types of these frames – X and Y sensor side, X and Y fiber mirror side. The mirror sides include the machined pieces for the light injection system assembly, not used for the prototype. Using the epoxy, the planks are sandwiched between the skins and enclosed between the frame pieces. Then the module is cured under the vacuum overnight.

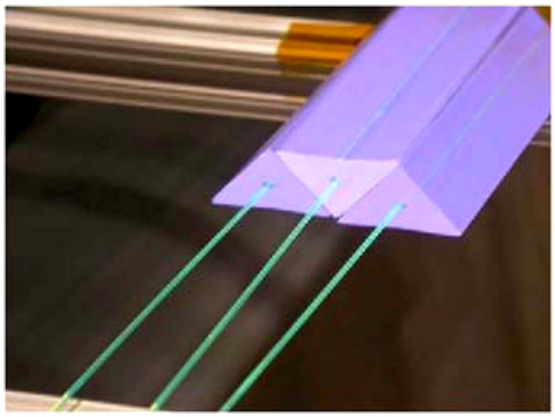

12: Triangular scintillator bars in the
g arrangement.

The last step is the WLS fiber and photosensor insertion. The 1mm outer diameter multiclad Kuraray Y11 WLS fibers were used, diamond-polished at photosensor side, and cleaved at 45° and blackened at the opposite side (Figure 5.13 left). Mirrored fibers were not yet available at the time of this measurement. Fibers were glued in ferrules and polished to length together (Figure 5.13 center). Three Hamamatsu MPPC photosensors described in chapter **Error! Reference source not found.**4 in detail were available for this testing. The PØDule with inserted WLS fibers is shown in Figure 5.13 (right).

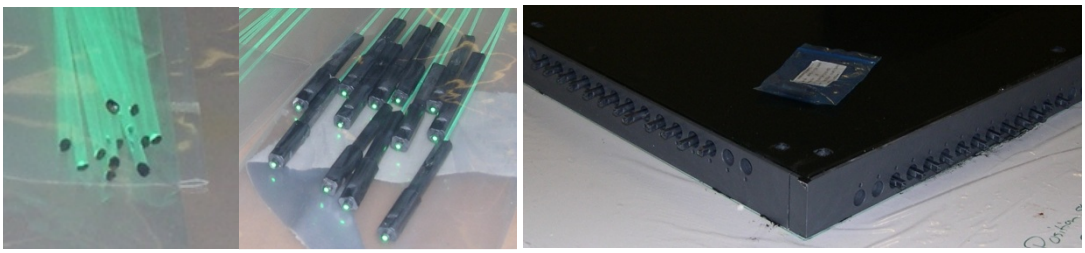

Figure 5.13: WLS fiber ends cleaver at 45o and blackened (left); WLS fiber glued and polished with ferrules (middle); PØDule with inserted WLS fibers and MPPC sensors on top (right).

5.7.2 Cosmic Rays Testing

A cosmic rays measurement was conducted using the above-mentioned PØDule prototype. The data were taken with the three different bar sets of three, using the same photosensors and readout electronics.

The two closest matched (in V_{bias}) sensors were used in each measurement. LeCroy [45] 2249A ADC used were installed in the CAMAC crate. Two 20x non-inverting ORTEC [46] VT120C amplifiers, connected in series, were used per each channel for the combined gain of ~148 due to input capacitance of long cables to the sensors. Biasing circuit for sensors with two shielded coax cables per sensor (separate for bias and signal) was used to reduce pickup noise and remove signal shape distortion since no impedance matching was used in a simple bias circuit. Ability to finely adjust the bias per each sensor was introduced into the circuit but not used since biases of two sensors picked were closer than the adjustment precision (~0.1V). Suggested by manufacturer biasing voltage value was used. Two scintillator pads (49cm x 35mm and 1cm thick) with PMTs attached were used as a trigger, one placed on top of the PØDule and one on the floor ~1m below. The schematic for the setup is in Figure 5.14.

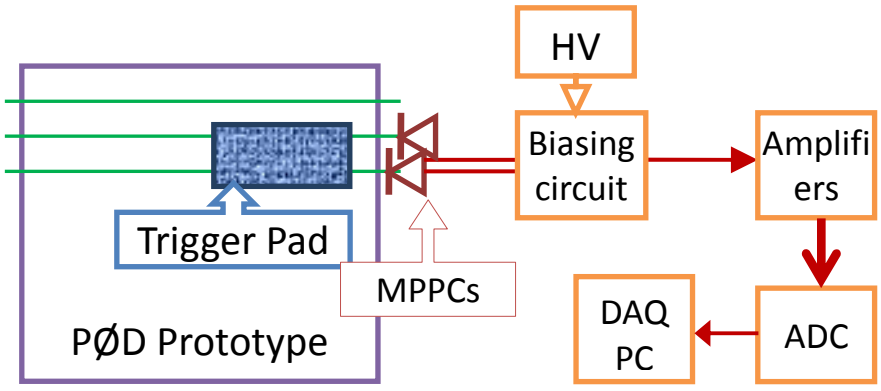

Figure 5.14: Schematic for prototype PØDule cosmic rays testing setup.

From Figure 3.2, active material length is estimated to be ~15mm vertically since there is a fair amount of the coating on the bar's corners. In addition, the size of trigger pads will contribute to this length by allowing muons to cross the scintillator bars at different angles. This will bring the average track length in the scintillator bar active material to ~16mm.

The results are presented as MPPC response in PE per 1 MeV of energy deposition, at two distances from the photosensor.

Below is a direct result that was obtained using the fibers with blackened ends:

- 25 cm from MPPC: 19.8±0.5 PE/MeV
- 205 cm from MPPC: 8.7±0.2 PE/MeV

The estimated effect of the mirrored fiber end with a mirror with reflectivity of 0.8 is added using equation 5.3. The measured previously light attenuation length of Y11 fiber is used (chapter 3.3.2). Here, Att_l and Att_s are long and short attenuation lengths in Y11 fiber, x is the position along the fiber, L is total fiber length and *r_mirror* is the assumed reflectivity that is taken to be 0.8. Factors A and B are such that for *r_mirror*=0, value equals to that of the direct result at 25cm and 205cm from the photosensors.

$$Ae^{-\frac{x}{Att\_l}} + Be^{-\frac{x}{Att\_s}} + r\_mirror(Ae^{-\frac{L-x}{Att_l}} e^{-\frac{L}{Att\_l}} + Be^{-\frac{L-x}{Att\_s}} e^{-\frac{L}{Att\_s}}) \quad 5.3$$

The corrected values yield:

- 25 cm from MPPC: 23.8 PE/MeV
- 205 cm from MPPC: 15.7 PE/MeV

This is comfortably above the design requirements (i.e. > 5 PE/MeV). In addition, this shows that these photosensors could be used at the reduced biasing voltage for noise reduction and extension of the detection range as the noise rate, gain and detection efficiency decrease at lower biasing voltage. For example, from PØD calibration, the average yield from Figure 5.9 (top) is ~9.2PE/MeV.

5.8 PØD Assembly

The required 40 PØDules (and 4 spares) were assembled in the similar fashion as the prototype. During the assembly, 25 water bags and led and brass radiators were installed as well. The detailed description of this process is presented in [47].

5.8.1 Scanner Description and Operation

An expanded description is presented for the scans that were conducted for each PØDule after its assembly, for the fibers and MPPCs insertion. The same set of 5 TFBs with a temporary RMM and necessary power supplies was used for all scanning operation. The coaxial cables were already attached

to the MPPC correction mini-boards so they needed to be connected and disconnected to the TFBs for each scanning.

Thus the main results expected from the scanning are:

- Check for possible connection errors, bad or broken WLS fibers
- Check for bad cable connections at MPPC board side, broken cables
- Measure a channel-to-channel output spread.

The scanner frame was a 9' x 10' custom CNC router by ShopBot [48]. The router spindle was replaced with a radioactive source with a shielding and collimator, a computer video camera for scanning alignment on the PØDule fiducial marks (corners). Each scan was conducted in 1.7cm steps along the eleven equally spaced lines for both X and Y coordinates to test both scintillator layers. A 0.7 mCu ^{60}Co radioactive source housed within a 4" lead shield with a collimator opening at the bottom with an opening angle of ~22.7^{o} was used. The PØDule corners were used as reference points for the scanning and viewed using a web camera mounted on the moving scanner element next to the source shielding. The scanner control and DAQ computer would then provide the coordinates for the next scanning position and collect and process the data.

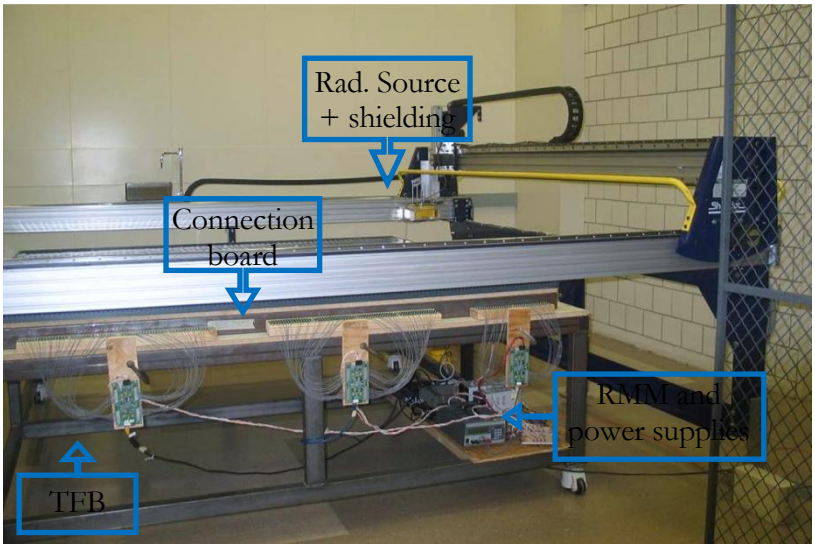

Figure 5.15: Scanner with a PØDule ready to be scanned.

5.8.2 Analysis of scanner data

Since a gamma radioactive source was used for the scanning process, a random trigger was used. Without the source, the dark noise spectrum will be obtained for the MPPC sensors. With the source, the shift in the pedestal position will be indicative of the signal level in each channel as the channel with the signal will have the pedestal at lower ADC count (due to AC coupling) than without it.

This is illustrated in Figure 5.16. Here the five outputs of every 30th bar of Y layer along a single line of scan are shown. The negative peaks correspond to radioactive source position above each bar. Vertical lines indicate the centers of the fitted peaks to better then ±0.5 mm.

The dark noise testing allows the independent from scanning check of the MPPC sensors. Then, during the scan process, the radioactive source crosses each bar in eleven points. These points should lie on a smooth exponentially decaying curve corresponding to the light attenuation in a WLS fiber with a mirrored end. A sharp step in this curve will indicate damage along the optical fiber. Only two such fibers had to be replaced out of 10400 PØD channels.

Additionally, the spread of the channel outputs is obtained. For this, the output amplitudes of each bar (that is, a pedestal position without source minus a pedestal position with a source over bar's center along each PØDule's center scan line) are plotted in Figure 5.17. The manufacturer suggested biasing voltage values were used for each sensor without any additional tuning. The output values are centered on a mean of ~14.0 with an RMS of ~1.9 ADC channels.

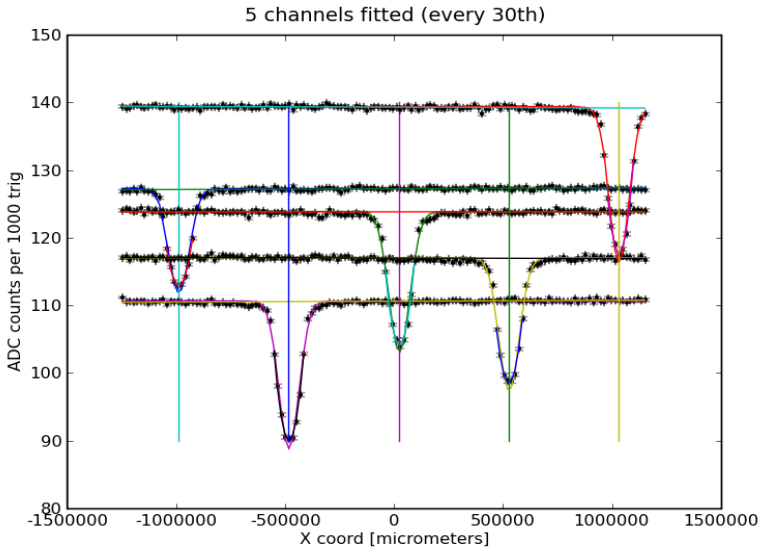

Figure 5.16: Outputs of 5 Y-layer bars for a single line of scan.

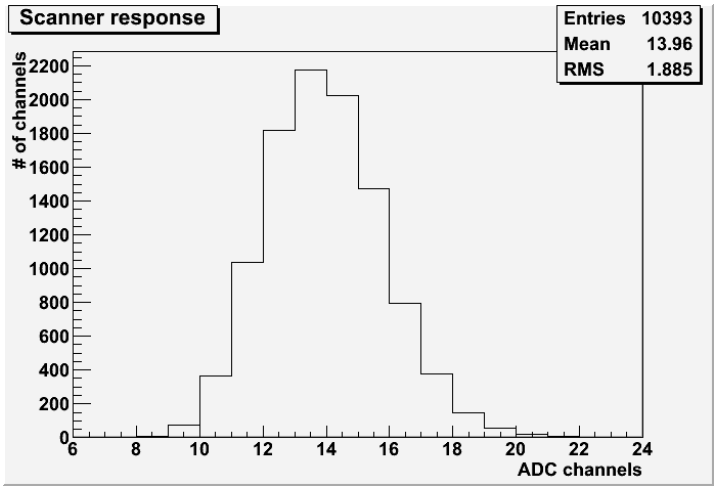

Figure 5.17: All PØD channel outputs.

5.9 PØD post-assembly QC

5.9.1 Dark Noise Testing

The dark noise of the MPPC detectors is a good measure for a quick check of the photo sensor itself and the electronics channel it is connected to. This check of all PØD channels before installation into the ND280 detector was carried out in two steps.

The first step included the dark noise testing during the scanning. Because the scanning procedure was carried out with the same set of the electronics that was known to be correctly functioning, the results were indicative of the actual MPPC performance after their installation into the detector modules. 14 MPPCs had to be replaced at this stage (out of total 10400). The typical bad sensor signature is either no output (that is no pedestal plus the two-three clearly separated PE peaks on the amplitude histogram), or an output with many barely separable PE peaks or a similar deviation. The testing was done at the manufacturer recommended biasing voltage values per each sensor.

The second step for this pre-installation check was performed after all the TFB boards were installed on the sides of each four superPØDules and shipping to the JPARC facility. A separate setup including the portable RMM module, power supplies and computer readout was connected to each TFB board and the dark noise histograms from a random trigger were plotted for each channel with a photo sensor connected to it.

In the first-pass check three TFB boards were found to be defective and were replaced (example of a bad TFB channel is shown in Figure 5.18). Additionally, two MPPC photo sensors were replaced for displaying too high value for dark noise. Same biasing voltage values were used as in a first step. A second-pass check was undertaken after the water system level sensors installation. This was deemed necessary since some electronics has to be moved to allow access to the water target volume. The check revealed that several coaxial cables between the MPPCs and the TFB boards had to be reconnected or replaced. After this was completed, all 10400 PØD channels were operational.

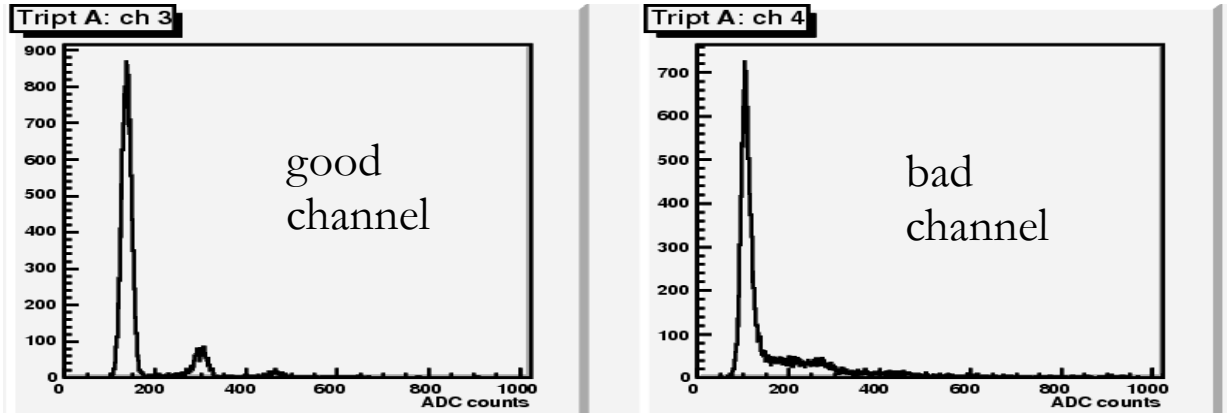

Figure 5.18: Example of good (left) and bad (right) TFB channels with MPPC dark noise spectrum.

5.9.2 Cosmic Muon Calibration and Channels Output Spread

After the shipping to JPARC facility, testing using cosmic muons was carried out as well. SuperPØDules were connected using a self-trigger based on the internal triggering of the TFBs with a CTM. The results of this testing are in described in Sections 5.2 and 5.3.

5.10 Other PØD Systems and Calibrations

Any further description of the PØD systems and their calibrations and operational parameters is presented in [47].

6. PØD SIMULATION AND EVENT SELECTION

6.1 ND280 Software

The ND280 software comprises of about 60 individual packages. It is based on the standard high energy packages, primarily on the ROOT [49] analysis package for data storage and underlying framework, and the simulation library from the GEANT4 [50] software package. For the data, the processing chain is the unpacking into software internal format (oaUnpack), calibration (oaCalib), reconstruction (oaRecon calling individual sub-detector reconstruction packages such as PØDRecon) and final reduced simple ROOT tree output by oaAnalysis package. All physics analysis is done using the oaAnalysis files.

6.2 MC Simulation

The MC simulation is divided into several steps as well. First, a kinematics file of neutrino interaction with the detector material is created using the neutrino interaction generators (NEUT [51] [52] {official generator}, and GENIE [53]) and the output of beam simulation that provides the neutrino beam flux and the neutrino energy spectrum at the near detector site. This file then is processed by the detector MC package (nd280mc, using GEANT4 for simulation of particles interactions with the detector geometry and materials) and the elecSim package (electronics and photo sensor simulation package). The output is in the same format as the unpacked data and is processed down the package chain (e.g. calibration, reconstruction and output formatting) same way as the data files.

The nd280mc package also supports a 'particle gun' feature – an ability to simulate a single particle with given start point, energy and direction. These can be a set of numbers or a set or rules, such as a range of energies, directions and starting point/plane/volume. Detailed information on the ND280 software packages and on the SK software suit is provided in [7].

6.2.1 PØDRecon

PØDRecon is the ND280 software package that handles the reconstruction tasks for the PØD detector. Its main features include hits cleaning (to reduce noise hits above threshold), track and shower reconstruction and particle identification (PID). Additional features include muon decay tagging, shower total energy reconstruction and others are planned, such as muon track momentum from range, etc. In this chapter, only a brief track reconstruction related features overview is included.

The noise hits can appear in the data files in two ways: if it is an MC file, then noise hits are simulated by the elecSim package photosensor simulation, and if it's the detector beam data file, then noise hits are present there as photosensor dark noise with higher amplitudes that pass the threshold cut of 2.5PE. The main feature of these noise hits is that they are typically low amplitude (just above the threshold) and randomly distributed in time, being uncorrelated to the higher charge hits from

particle track. Thus a set of simple cuts can drastically reduce the amount of these hits while keeping the hits from the neutrino events.

The hits are kept during the cleaning if any of the following hits selection criteria implemented in PØDRecon is true:

- Hit charge > 15 pe.
- Hit charge > 7 pe, &has a neighbor in same view within ±30 ns & ±10 cm.
- Has a neighbor ± 30 ns & ± 3.5cm in space (with no charge requirement).

Noise cleaning effectively removes the dark noise hits from the tracks. With only <10 hits of low charge (thus weight) left on average within the event time window and between the 10400 channels, the contribution of the dark noise hits to the reconstruction is minimal.

The actual track reconstruction process uses a Hough Transform to find the track first, then a road following algorithm with a ~60 mm wide road (within water target). This allows for a correct track length reconstruction in both the magnetic field present and without one, and is tolerant to the possible faults like a missing single hit within a track (either a bad channel or with charge below threshold) or possible misalignments. From chapter 5.5, we see that the alignment residuals are much smaller than the algorithm 'road width' or the distance between the hits in adjacent bars; thus is not affecting reconstruction.

The next step is the assignment of the particle identification based on a number of parameters such as the track width, length and energy deposition profile, etc. The following PIDs are used: 11 for heavy, or proton like (11 is unused in the current software version), 8 – light, or muon-like, 3-EM, or electron-like and 1 – other, all that don't fit under previous categories. Any additional features can be run after this step.

6.2.2 MC Track Hits Reconstruction Efficiencies

Reconstructed MC track hits efficiency in each detector layer has been studied. For each long MC track, a number of hits associated with a track in each detector layer is checked. Due to the triangular shape of the scintillator bars used, most layers are expected to have double hits per each layer.

Here, an efficiency of the reconstruction algorithm is tested. For this purpose, long muon tracks are simulated using the particle gun MC. 0.7GeV and 0.8GeV muons starting just in front of the PØD were simulated, 1000 events each. These energies were picked as corresponding to approximate "sand" muons and as the lowest values for which muons pass through the entire PØD.

The reconstruction information is used to identify the long tracks with at least one hit in both first and last PØDule. Then the algorithm is run on the hits within the track, layer by layer with X and Y separate, to count the double (or more), single and missing hits.

Due to the selection rules requiring at least one X or Y hit in a first PØDule and at least one X or Y hit in the last, the efficiency values are biased for both X and Y layers in those PØDules. Therefore, the results for these layers are excluded from the total. Also note that for some layers, three or more hits can be found due to the delta rays being emitted.

The averaged efficiency values for all 38 PØDules are as follows: 0% (0 from 71239) for layers with missed hits, ~21.64% (15414 from 71239) for single hits, and ~78.36% (55825 from 71239) for double (or higher) hits with ~0.85% (605 from 71239) of triple and higher number of hits being included.

6.2.3 Muon and Pion Energy Range Study

The NEUT and GENIE MC files contain numerous events that have a single muon or a positively charged pion in a final state. Thus it is possible to plot the dependence of the particle energy vs. the reconstructed track length and vice versa.

The tracks with a reconstructed vertex in a fiducial volume are used in this study. All tracks were required to be contained within PØD.

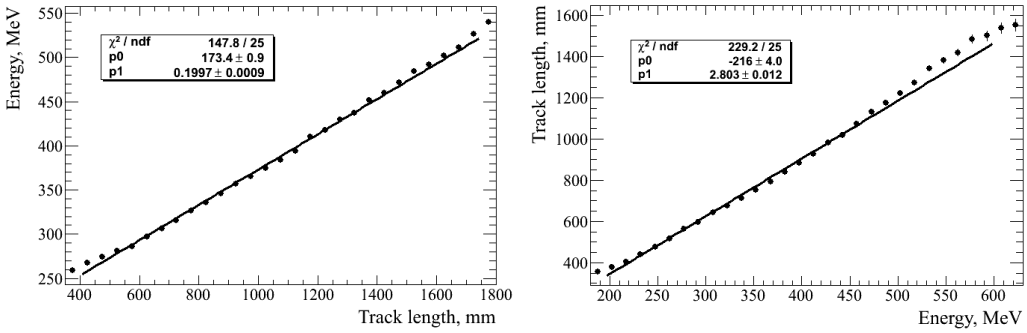

Figure 6.1: Energy vs. reconstructed track length (left) and reconstructed track length vs energy (right) for muons in PØD.

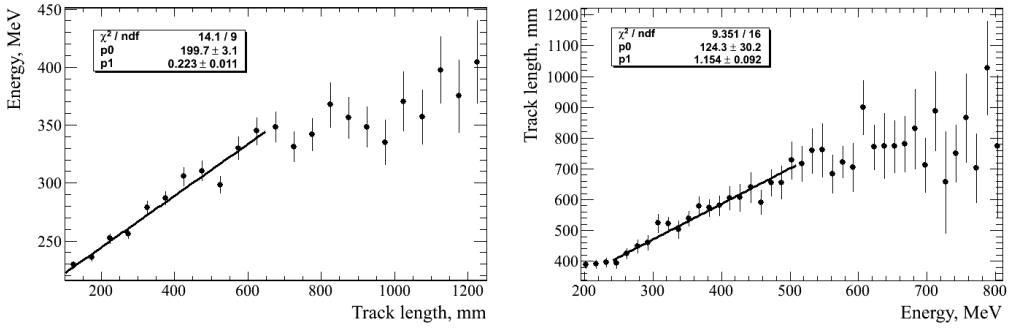

Figure 6.2: Energy vs. reconstructed track truth trajectory (left) and reconstructed track length vs energy (right) for pions in PØD.

For the muons, a linear dependence is expected. The deviation from the linearity is due to the non-uniformity of PØD (water target region and CECAL region) and to the increase of energy deposit per unit length dE/dx at low energies. Other contributions are the lack of high energy events (due to the track containment requirement), scattering and nuclear absorption for the pions.

The fitted result for the muons is shown in Figure 6.1 and for the pions is in Figure 6.2. Note that this is a study of this dependence as a test of the MC performance; it is not detailed enough to be used in the final reconstruction of the tracks energy from range that will require careful treatment of track angles and amounts of different materials passed. Also, the pion linear range is limited, thus a fit is done only on that part. In addition, the histograms for the contained muon track length from truth and the corresponding truth MC muon energy are presented in Figure 6.3.

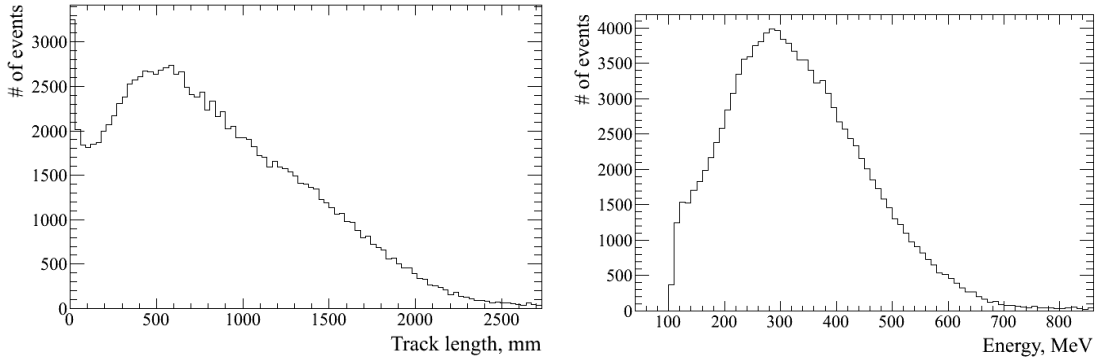

Figure 6.3: Contained muon track length (left) and the corresponding truth MC muon energy (right).

6.3 Event Selection Criteria

In PØD, due to the specifics of the design, the reconstructed events will be subdivided into the one, two and three-track types, with and without reconstructed showers. With T2K low energy neutrino beam, protons will be below PØD detection threshold in the majority of events. Thus, a study will be done on the CCQE and CC1π^+ events purity and efficiency under different selection criteria accounting for that fact.

Selected events are expected to contain the following signatures for the wanted processes: a single muon-like track for CCQE and two muon-like tracks for CC1π^+ events. Additional criteria will include requirements for a vertex in a fiducial volume (to be explained in section 6.3.2) and zero showers presence to suppress the contributions of other events and increase selection purity. Also, three-track event option will be looked at for the energetic events where a proton can leave a detectable track. All selected events will also be contained within the PØD volume (explained in the next section).

6.3.1 Processing oaAnalysis File Format

After the calibration and reconstruction, the data files are converted into the compact format of the oaAnalysis package within the ND280 software. In essence, this format is the ROOT [49] tree

structure that compactly stores the output from the reconstruction, with the additional truth information tree for MC generated events.

The advantages of this format are:

- Smaller file size (~1/10) since only final reconstruction information is kept,
- Ability to open for analysis using only oaAnalysis package and ROOT
- Option for using PyROOT, ROOT extensions for use with Python programming language.

For the analysis tests, a simple framework for using both MC and data files was developed for all the analyses presented further. Combining all analyses types into a single file allows for both the simplification of the code and the usage of the same parts of the code for both MC files and data files that is important for any comparative studies. Technical details mentioned here will be further explained later in this chapter.

Thus the analysis framework is a single python script that accepts oaAnalysis format files as input and produces various outputs from the analysis section. Multiple input files are accepted and treated as a single input source. The framework will recognize between NEUT, GENIE and particle gun MC files, and data files, and process them accordingly. Possible analyses include calibration routines, physics data analysis and presented further in this chapter truth-to-reconstruction comparison. The latter can be realized only using MC files produced from the events kinematics supplied using NEUT or GENIE event generators for it requires the presence of both the event truth and reconstruction data in a file.

This format also contains the data quality flags that are set to display the accelerator and detector status on per-event basis. Value of 1 means normal operations, value of 0 or below are errors codes specific for each subsystem. For all further analyses, the data quality flags in the beam data oaAnalysis files should be equal to 1 for all selected events (the flags used are as follows: BeamSummaryData.GoodSpillFlag, beamSummary.BeamSummaryDataStatus and dataQuality.P0DFlag).

Additional feature for the oaAnalysis format is the assessment of whether the event is contained in PØD. Two values are calculated, EndDeposit and SideDeposit. Both must be zero for the event to be fully contained within PØD detector.

For the EndDeposit, if hits that are associated with a track lay in the last PØDule #40, then the light deposition is summed up from all such hits. This deposition is left in the units of PE. SideDeposit is the sum of light deposit for all hits that occur in the several outermost bars of both X and Y layers. For illustration, the X layer that has 126 bars total and two are taken from each side, these will be bars 1 and 2, and 125 and 126.

Graphically, EndDeposit values are shown in Figure 6.4 (left) and SideDeposit values are presented in Figure 6.4 (right). These plots were obtained from a particle gun MC with 1000 2GeV muons sent at angles between 0 and 25 degrees from the 10cm x 10cm square at the beginning of water target for EndDeposit, and between 30 and 75 degrees for SideDeposit. Figure 6.5 shows the number of muon tracks falsely identified as contained (out of 1000). At 2GeV, all muons leave the detector. The mis-id occurs when a track exits between the bars in the water target modules via the water bags region. Increasing number of bars reduces this mis-id, but it also reduces the usable detector volume. Two bars reduce it by ~5cm from each side, and 6 by 15cm that is rather excessive. Thus, a value of 4 bars was chosen to set the mis-id of the side exiting tracks as contained in water target region at ~12% for high angle tracks.

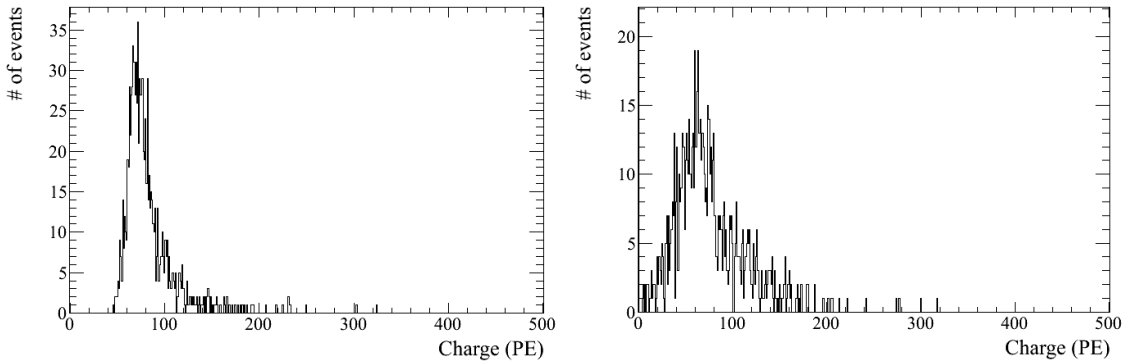

Figure 6.4: EndDeposit (left) and SideDeposit (right) values for 1000 MC muons.

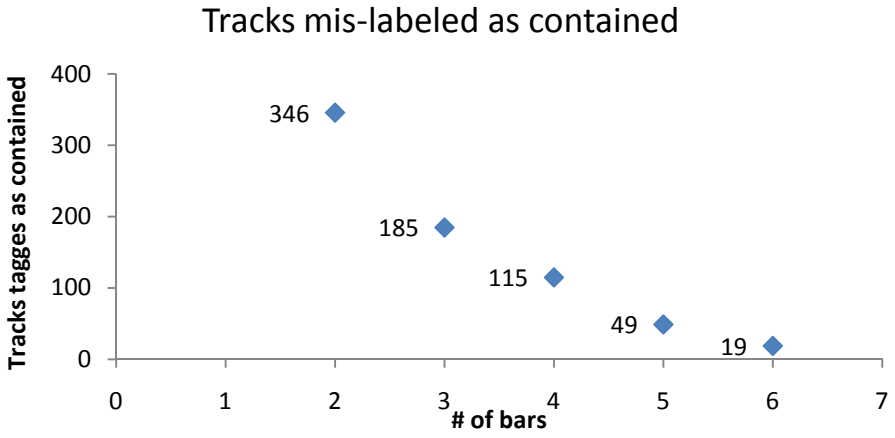

Figure 6.5: Number of tracks mis-labeled as contained vs. number of SideDeposit contributing bars for 1000 large angle side exiting MC muons.

6.3.2 Fiducial Volume Optimization

As the events occur progressively closer to the detector edge, the probability for a track to be marked as non-contained is increased even if it actually stops within physical PØD boundary. This is due to the fact that a track may hit the four outermost bars in a detector that comprise the .SideDeposit value in the event file and make it non-zero, thus marking a track as non-contained. Near the boundary marked by these four bars, the probability for single track and double/triple track events to be marked as non-contained is different. Thus, a choice of fiducial volume may impact the physics result.

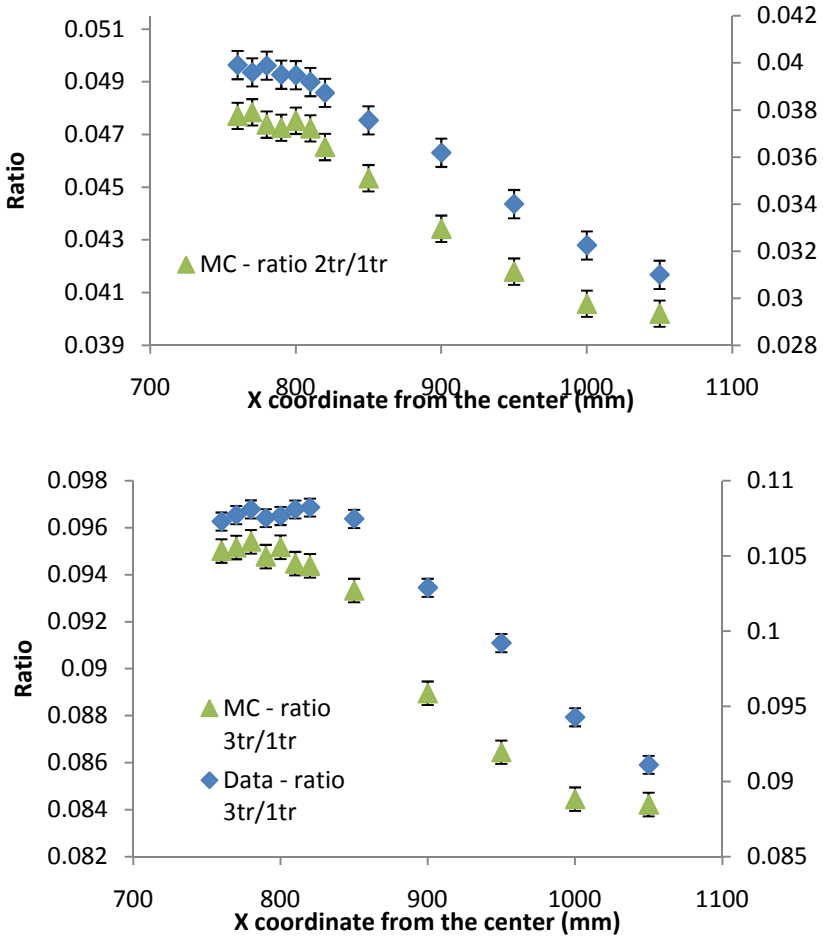

Figure 6.6: Two-track to single-track events (top) and three-track to single track events (bottom) ratio vs. X coordinate.

A study was conducted using NEUT MC and beam data with different sizes of the fiducial volume in PØD. Only contained events with no showers were selected.

The X and Y side lengths are different by ~7cm in PØD, so corresponding adjustment was added into the definition. The slight shift between detector center position and 0,0 of the coordinates is accounted for as well. The fiducial volume was changed in 5cm steps except around the suggested value where step was 1cm. The ratio of two (top)/three (bottom) track events to single track events vs. the X (shortest) coordinate from the center is shown in Figure 6.6. As it can be seen, the simple ratio of two-track to single track events (top) and three-track to single track events (bottom) starts to shift for X values larger than the 810mm value, thus the fiducial volume was chosen to be 810mm in X, or ~25cm from the PØD edges. Thus formal fiducial volume definition that will be used further on is such: event vertex should be in water target region at least 25cm from the detector edges.

6.3.3 MC Event Interaction type Definition

Two definitions of the MC event interaction type are used: the generator level (g.l.) and the final state interaction (f.s.i.). In g.l., the stamp from the neutrino event generator is honored; for example, for NEUT g.l. codes, code 1 stands for the CCQE, and codes 11 and 13 (that is both neutrino interaction with a proton and a neutron) are for CC1π^+. For the f.s.i., the CCQE event type is defined as an event with a single muon in the after-the-nucleus final state using the MC truth information, and the CC1π^+ - as an event with a single muon and a single pion with any number of protons and neutrons present for both types. These definitions are processed for events that first pass the application of the selection rules below. A code excerpt defining the f.s.i. reaction as NEUT 1, 11, 13 and 200 for all others is in Appendix I.

6.3.4 Application of Selection Rules

After incorporating the selection rules discussed in section 6.3, the analysis was run in the truth-to-reconstruction comparison mode on the oaAnalysis NEUT MC4B MC files with event type defined using the g.l. reaction codes. The number of events for the corresponding rules for 'water-in' beam data dataset from Runs I and II is added for comparison. The p.o.t (protons on target) calculated from the oaAnalysis files for this dataset is 9.89E+19.

The results from this study are shown in Table 6.1. The selection rules reflect the expectations that the CCQE events should leave 1 or 2 tracks with a single muon-like track, and the CC1π^+ events can have either a single muon-like track reconstructed, or two muon-like tracks, or three-track events for the CC1π^+ events energetic enough to have a proton track reconstructed as well.

Table 6.1: Efficiency and purity for the different event selection criteria.

SELECTION RULE	DATA EVENTS	MC EVENTS	CCQE	CC1π^+	EFFIC. (%) CCQE|CC1π^+	PURITY (%) CCQE|CC1π^+
Vertex in fiducial, contained with constituents	43401	281640	109226	51240	100|100	38.79|18.19
Single light track, no showers	6042	72376	46370	9441	42.45|18.43	64.06|13.04
Two tracks with at least one light, no showers	1610	20360	7631	6567	6.98|12.82	37.48|32.25
Two muon-like tracks, no showers	226	3553	1268	1384	1.16|2.70	35.69|38.95
Three tracks with at least one light, no showers	197	2672	109	835	0.10|1.63	4.08|31.25

The efficiencies are with respect to the number of events that have their vertices in the fiducial volume (e.g. water target, 25cm from detector edge) and have any constituent tracks contained in the PØD, ignoring any showers. From that, the total efficiency for the selection rule 'three tracks and no showers' events requirement is very low (below 1%), thus it is not appealing for final analysis due to low statistics but can be used to verify the results obtained. No cut on track angle(s) or length(s) besides containment requirement is made as not to cut on any kinematic variables.

6.3.5 CC1π^+ and CCQE Selected Events Study

Firstly, let's take a look at the interplay between the f.s.i. types events that are defined by their final state that is by particles that exit the nucleus and can leave a detectible signature and the g.l. typed events that are assigned by the event generator when event is being generated. .

As an example, the g.l. CC1π^+ type events may have the f.s.i. that has just a muon (protons and neutrons are not being counted here), a muon and a positive pion, or a muon with any other pion due to the charge exchange of it before leaving the nucleus. For the defined using the f.s.i. CC1π^+ type events, a two muon-like track final state is expected. The backgrounds can be from a number of generator level event types that have a muon and a charged pion or two charged pions in a final state, or CCQE events where proton track is mis-labeled as a light (that is a muon-like) track.

A pion that has left the nucleus still can have the energy that is below detection threshold, or can be absorbed by any other nucleus in its way thus leaving a very short or no reconstructed track. Again, only a single track may be reconstructed. These events present background to the f.s.i. CCQE reaction type that is defined as a single muon-like track. Additional contributions can come from any events with an energetic muon or charged pion with other particles below detection threshold. Thus it is important to consider the single muon-like track events. In addition, a small amount of high energy parent neutrino CC1π^+ events will leave the three reconstructed tracks. The simple interplay between the g.l., f.s.i. reaction types and the one, two and three-track reconstructed events is shown graphically in Figure 6.7. Note that 'no shower' selection rule is applied by default.

Next, we want to obtain an estimate on which generator level types of events leave the one, two and three-track signatures in PØD. For that purpose, NEUT MC files are processed through the event selection rules mentioned in 6.3.4. This yields the reaction codes that can be a background to the CCQE and the CC1π^+ events in PØD detector.

The g.l. reaction codes for the interactions and their contributions to each selection rule are listed in the Table 6.2 below. The negative values are for the muon anti-neutrinos. A full list of all reaction codes for NEUT is in the Appendix II.

For the single light track events, we see that it is a rather pure charged current quasi-elastic (CCQE) sample with the second largest contribution from the charge current single positive pion (CC1π^+) events and background contributions from all other.

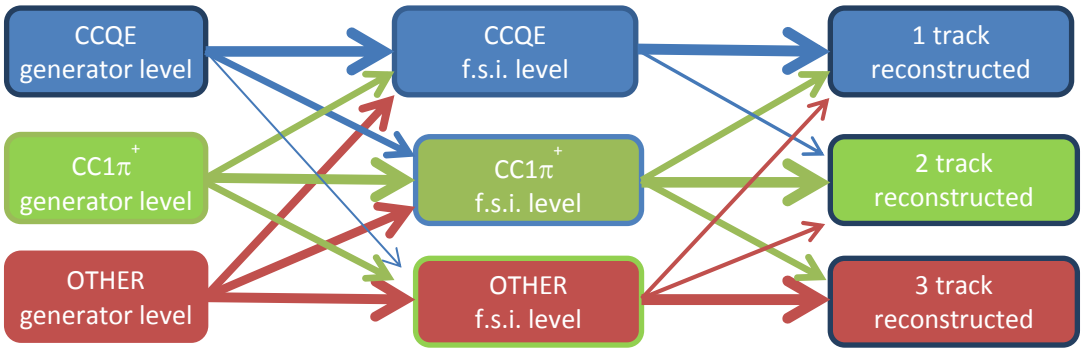

Figure 6.7: Generator level and final particle state event types relation to the number of the reconstructed tracks.

For the two-track events with at least one light track, the major single contributors at the g.l. selection are the CC1π^+ reaction and the CCQE reaction, for which both the muon and the proton are reconstructed. If two light tracks are required, only those CCQE event will contribute for which the proton track is mis-identified as a light one; however, this reduces the selection efficiency due to the muon PID without benefits for the purity, thus it is not used. An additional possible criterion is an angle between the tracks for it is strictly determined by the particles' momenta in the two-particle final state. However, this is based on the momentum measurements of the reconstructed tracks in PØD that is still in the development. For CC1π^+ events, an approximately uniform distribution of angles is expected since it's a three-particle final state with one particle not visible in the reconstruction.

Another contribution to single and two-track comes from the CC1π^0 reaction. Due to pion charge exchange or re-absorption and re-emission in the same nucleus, this reaction may end up with a π^+ in the final state or no pion at all, thus serving as background for both CCQE and CC1π^+ reaction types. Otherwise, there is a muon and a possible proton track plus one or two showers from the π^0 decay. Thus, requiring no showers in addition to the two muon-like tracks should mostly exclude the reactions with π^0s in a final state.

The rest of the events are comprised of various charged or neutral current coherent pion and deep inelastic scattering (DIS) reactions. These backgrounds are suppressed by the simple selection rules: requirements to have one or two muon-like tracks and no showers. However, the events with two charged pions, or muon and single energetic charged pion with others below the detection threshold will leave the two muon-like tracks signature as well.

For the high energy parent neutrino, the CC1π^+ events will leave the three reconstructed tracks as well as the DIS and NC events.

Table 6.2: Neutrino interactions, reaction codes and their contributions.

EVENT CATEGORY	INTERACTION	NEUT REACTION CODE	SINGLE TRACK EVENTS (%)	TWO TRACK EVENTS (%)	THREE TRACK EVENTS (%)
CCQE	$\nu_\mu n \rightarrow \mu^- p$	1	64.07	37.48	4.08
CC1π^+	$\nu_\mu p \rightarrow \mu^- p \pi^+$ $\nu_\mu n \rightarrow \mu^- n \pi^+$	11 13	10.66 2.38	27.34 4.88	26.01 5.24
CC1π^0	$\nu_\mu n \rightarrow \mu^- p \pi^0$	12	2.37	5.35	9.84
CCOπ^+	$\nu_\mu O \rightarrow \mu^- O \pi^+$	16	1.49	4.92	1.05
CC multiπ	$\nu_\mu (n\|p) \rightarrow$ $\mu^- (n\|p)$ (mπ)	21	1.06	4.56	15.12
DIS	$\nu_\mu (n\|p) \rightarrow$ $\mu^- (n\|p)$ (mesons)	26	0.11	1.39	7.75
CC Other		22, 23	0.09	0.59	3.22
NC1π^0	$\nu_\mu n \rightarrow \nu_\mu n \pi^0$ $\nu_\mu p \rightarrow \nu_\mu p \pi^0$	31 32	1.11 2.14	0.90 2.81	1.20 5.01
NC1π^-	$\nu_\mu n \rightarrow \nu_\mu p \pi^-$	33	1.50	1.87	1.65
NC1π^+	$\nu_\mu p \rightarrow \nu_\mu n \pi^+$	34	1.58	1.19	1.68
NCOπ^0	$\nu_\mu O \rightarrow \nu_\mu O \pi^0$	36	0.17	0.32	0.19
NC multiπ	$\nu_\mu (n\|p) \rightarrow$ $\nu_\mu (n\|p)$ (mπ)	41	0.88	2.72	7.30
DIS	$\nu_\mu (n\|p) \rightarrow$ $\nu_\mu (n\|p)$ (mesons)	46	1.18	1.13	5.91
NC Elastic	$\nu_\mu p \rightarrow \nu_\mu p$ $\nu_\mu n \rightarrow \nu_\mu n$	51 52	6.61 2.00	0.41 0.40	0.45 0.44
NC Other		42, 43, 44, 45	0.11	0.38	1.20
All $\overline{\nu_\mu}$		All negative	1.47	1.27	2.47

6.4 PØD MC Contained Event Parent Neutrino Energy

The 'containment in PØD' requirement for the selected events additionally sets a limit on the primary neutrino energy for each event type. This yield different energy ranges detected for the various-track number selections and for different reaction types within each selection.

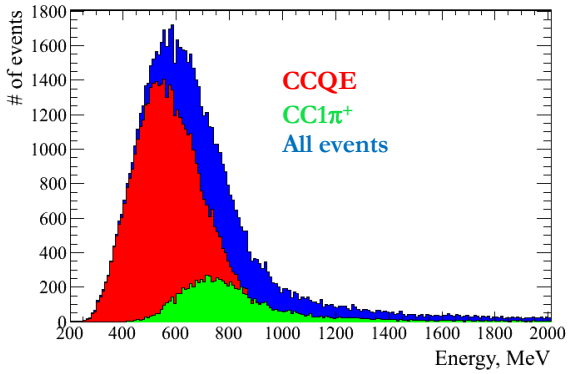

Figure 6.8: MC truth neutrino energy for single track events.

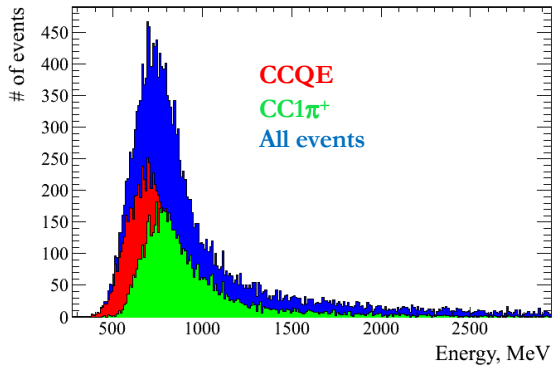

Figure 6.9: MC truth neutrino energy for two-track events.

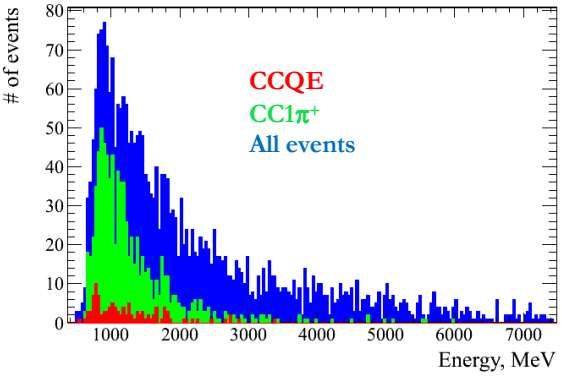

Figure 6.10: MC truth neutrino energy for three-track events.

6.4.1 Single Track Events

This selection rule includes all events that have a single light track, no showers. The overlay of the parent neutrino from MC truth (using NEUT g.l.) is shown in Figure 6.8. The prominent difference in energy between the CCQE and CC1π^+ events is also translated into the track length difference that will be fitted later to obtain the ratio.

6.4.2 Two-Track Events

Only the selection rule requiring at least one light track (e.g. muon-like) is used. The reason is being that requiring two light tracks reduces efficiency but not affecting the purities as to support this reduction (see Table 6.1). This selection includes the CCQE events with a proton track reconstructed as well as CC1π^+ events with the tracks from both a muon and a pion. The overlay of the neutrino energies for this selection rule is presented in Figure 6.9.

6.4.3 Three-Track Events

The three-track selection used requires at least one of the tracks to be tagged as light and no showers. This is a very pure CC1π^+ selection with minimal CCQE contamination that can be treated as part of the background. Thus this sample is not used in the final fit for the ratio. The Figure 6.10 shows the MC parent neutrino energy for this event selection rule.

7. WATER-IN DATA ANALYSIS

7.1 Datasets used

The dataset used for this analysis includes both Run I (Jan-Jun 2010) and Run II (Nov 2010 - Mar 2011). There are two further sub-divisions – running with water in the water target, and without it.

The run numbers for the Runs I and II for 'with water' operations are from 4165 to 7663 for the total p.o.t of 9.89×10^{19}. This value is calculated using the oaAnalysis file information and honoring the following data quality tags as this is a PØD-only analysis using contained events: BeamSummaryData.GoodSpillFlag, beamSummary.BeamSummaryDataStatus and dataQuality.P0DFlag.

The run numbers for the Run II 'water out' operations are from 7665 to 7754 for the total p.o.t. of 3.57×10^{19}. Same data quality flags were honored.

Currently, the 4B data processing is being used. The corresponding MC is being used as well. The main MC sample is the one generated from the NEUT v5.1.0 kinematic files using the jnubeam11a ND6 flux, with the ND280 software version. This MC has a total of 99.2×10^{19} p.o.t. Where applicable, it will be noted that GENIE MC is used. The p.o.t. for these files is 106.0×10^{19}. The version of GENIE package was v2.6.2; same ND280 v9r7software version was used as well. As the goal is the CCQE/CC1π^+ ratio and the scaling factor cancels, the MC histograms are scaled to data using the total number of entries for each selection rule data sample. The scaling using the p.o.t ratio between the data and the MC was also used to verify that same results are obtained. Further details on this data production can be found on the T2K website[4].

7.2 Fitting explained

The main goal of this work, the CC1π^+/CCQE ratio difference between the data and the MC prediction can be defined as:

$$R_{data/MC} = \frac{R^{Data}}{R^{MC}} \qquad 7.1$$

where the top and bottom parts of the fraction are the individual CC1π^+/CCQE ratios for the data and the MC separately.

The data and MC analysis outputs for the selection rules are histograms for the quantity selected. For each bin for the data histogram, there are contributions from the CCQE, CC1π^+ and background events. For the selected event type definition (g.l. or f.s.i.), the relationship between data and MC for each type will be:

[4] http://www.t2k.org/nd280/datacomp/production004/mcp/mcp4

$$N_{Exp}^{CCQE} = C^{CCQE} N_{MC}^{CCQE} \quad 7.2$$

The equation 7.2 gives the example for the CCQE events type but is valid for all other as well. The C^{CCQE} is the difference coefficient between the MC number of the events and the expected number of the events of this type in data; it is determined from the fit. We can rewrite the equation 7.1 in terms of this number of the expected events as:

$$R_{data/_{MC}} = \frac{N_{Exp}^{CC1\pi+}}{N_{Exp}^{CCQE}} / \frac{N_{MC}^{CC1\pi+}}{N_{MC}^{CCQE}} = \frac{N_{Exp}^{CC1\pi+}}{N_{MC}^{CC1\pi+}} \times \frac{N_{MC}^{CCQE}}{N_{Exp}^{CCQE}} \quad 7.3$$

Also, from we can express the C coefficients as:

$$C^{CC1\pi+} = N_{Exp}^{CC1\pi+} / N_{MC}^{CC1\pi+}, C^{CCQE} = N_{Exp}^{CCQE} / N_{MC}^{CCQE} \quad 7.4$$

Plugging equation 7.4 into the equation 7.3, we get this result for the CC1π^+/CCQE ratio difference between the data and the MC prediction:

$$R_{data/_{MC}} = C^{CC1\pi+} / C^{CCQE} \quad 7.5$$

The equation 7.5 provides us the expression for the obtaining the final result, where the coefficients $C^{CC1\pi+}$ and C^{CCQE} are the only components.

The data and MC analysis histogram outputs for each selection rule can be processed to obtain these coefficients. The following functions will be used for the minimization:

$$N^{exp} = C^{CCQE} N_{MC}^{CCQE} + C^{CC1\pi+} N_{MC}^{CC1\pi+} + C^{bkg} N_{MC}^{bkg} \quad 7.6$$

$$N^{exp} = C^{CCQE} N_{MC}^{CCQE} + C^{bkg} (N_{MC}^{CC1\pi+} + N_{MC}^{bkg}) \quad 7.7$$

$$N^{exp} = C^{CC1\pi+} N_{MC}^{CC1\pi+} + C^{bkg} (N_{MC}^{CCQE} + N_{MC}^{bkg}) \quad 7.8$$

The equation 7.6 is for obtaining all three coefficients simultaneously, while the equations 7.7 and 7.8 will treat the CC1π^+ and the CCQE events correspondingly as part of the background and will be used for the verification of the results obtained from the first equation.

A Poisson likelihood method for the fitting procedure will provide the C coefficients by maximizing the likelihood between the N^{exp} from the MC histograms and the actual values of the bins N^{obs} in the data histogram. This procedure will be performed using the ROOT Minuit package [54].

7.3 Data to MC and MC to MC Comparisons

The two direct variables that are immediately available for the data samples after the selection rules are the track lengths and track angles (to detector Z axis, between tracks). These are compared

between the data and the MC samples. In particular, the track length samples are expected to have a better correspondence than angle ones as the track length that is directly defined by the detector hits and reconstruction (using a "walking" algorithm) is more robust in the magnetic field presence for the curved tracks than the angle one (calculated by the Kalman fit.). In addition, there is always a fraction of the low-momentum (low-Q) events affected by the uncertainty in the nuclear Fermi momentum model for the materials used in the detector, and that will introduce differences in the angle data.

The track length and the angle to Z axis for a single light track selection from a water-in data are presented in Figure 7.1. The results of the Kolmogorov-Smirnov test probabilities for the data and MC are presented as well. The K-S test was chosen as a comparison measure over other statistical tests as the most suitable for this assessment whether the data and MC distributions can be coming from the same parent distribution. Due to the K-S test sensitivity on the binning of the data, checks with different binning were done to ensure result validity (the PØD 'step' size is ~4 cm in ECALs, ~7cm in water targets because of the water bags; the sum $\sqrt{7^2 + 4^2} \approx 8$cm sets a 'natural' scale for the PØD single track length resolution).

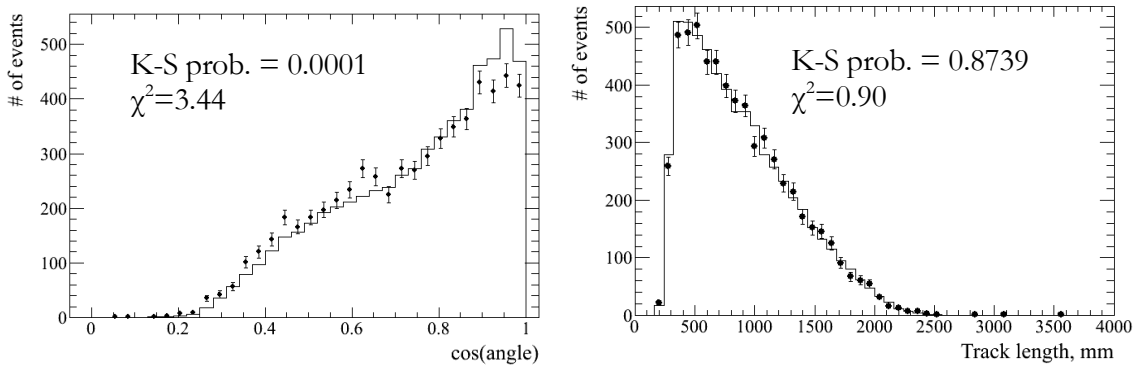

Figure 7.1: Data to MC comparison for single light track events:
angle to Z axis (left) and track length (right).

A similar comparison is done using other selected samples. The histograms with best K-S probability are chosen for the further analysis.

Before the actual fit, a validation test using the g.l. CCQE events is performed. For that, a CCQE enriched selection from the single light track sample is produced using the optimized cuts on the track length and angle to Z axis. Since these are kinematic variable cuts, this sub-sample is only used for the check of the results and not as part of the final analysis.

The cuts are optimized using the signal over the square root of the background criterion. For both the track length and the angle, this is presented in the Figure 7.2. The track length cut is carried out first. The best cut values were to select the track lengths longer than 720 mm and at the cosine of the angle smaller then 0.86.

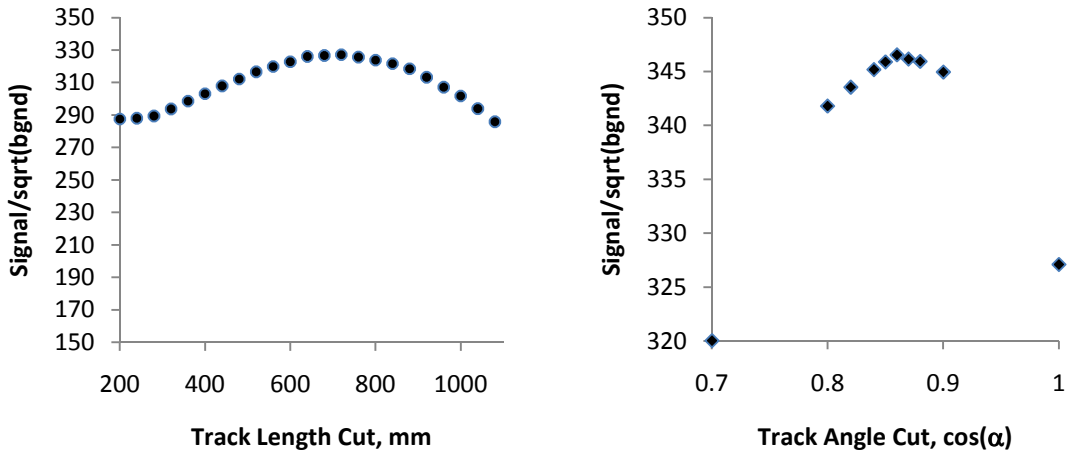

Figure 7.2: Cut optimizations for the track length (left) and the angle to Z axis (right).

After both cuts, a ~83% purity of the CCQE events is reached. The corresponding composition of track length (Figure 7.3 left) and the angle to Z (Figure 7.3 right) for the result are presented. The K-S test values between the data and the MC for this sub-sample are calculated to be 0.9998 and 0.1085 respectively for the track length and the angle histograms.

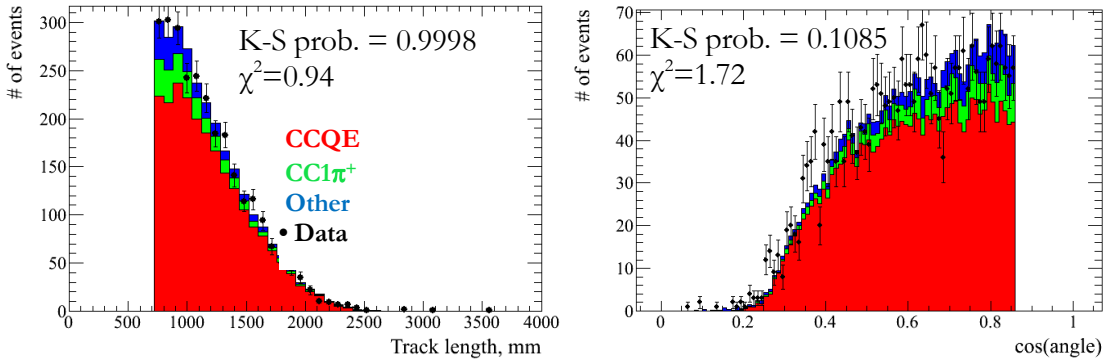

Figure 7.3: Data to MC comparison for single light track selected CCQE sample: track length (left) and angle to Z axis (right).

Thus we see that the g.l. CCQE events for the NEUT based MC has a very good correspondence with the data for the track length variable. Note that this is a direct comparison, thus no systematics cancellations as in the ratio case is expected. This result hints also on a low systematics contribution from the ND280 MC software chain as the NEUT files are processed, such as possible calibration or reconstruction effects.

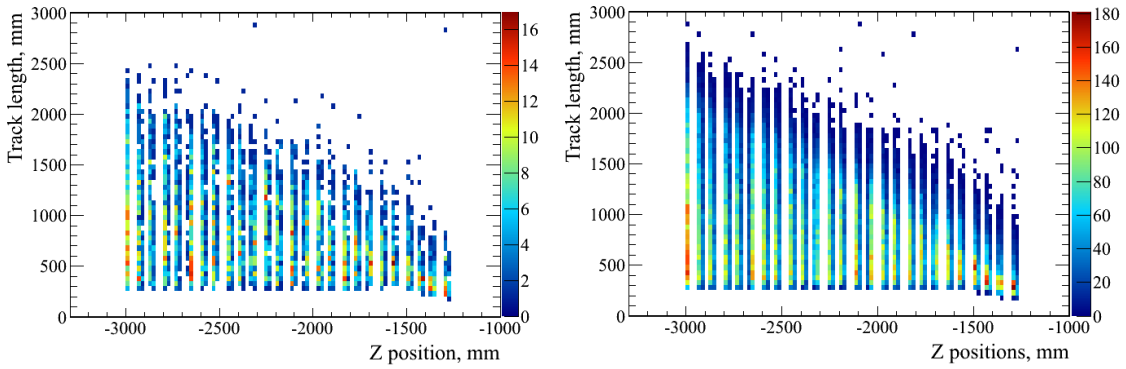

Figure 7.4: Track length vs. Z position for single light track sample. Data (left) and MC(right) are presented.

As only the tracks contained in the detector with the vertex in the water target are selected, the limit on the maximal track length will be imposed by the detector physical size depending on the vertex position. Thus, a plot for the different track lengths for each Z position within water target is presented for both the data Figure 7.4 (left) and the MC Figure 7.4 (right).

Another comparison that can be done at the MC level is to check the difference between the track lengths for the reaction types within the same selection sample. If the difference is small, or there is a high correspondence between the two or more reaction type sub-samples, then the fitting process will be highly correlated for such samples and will not be able to separate them during the fit to the data.

Table 7.1: Reaction types comparison for single track MC selection.

CHI2/DOF|K-S	CCQE	$CC1\pi^+$	BACKGROUND
CCQE	0.00|1.000	9.02|0.000	25.23|0.000
$CC1\pi^+$	9.02|0.000	0.00|1.000	9.27|0.000
Background	25.23|0.000	9.27|0.000	0.00|1.000

Table 7.2: Reaction types comparison for two-track MC selection.

CHI2/DOF|K-S	CCQE	$CC1\pi^+$	BACKGROUND
CCQE	0.00|1.000	3.99|0.000	4.01|0.000
$CC1\pi^+$	3.99|0.000	0.00|1.000	1.36|0.002
Background	4.01|0.000	1.36|0.002	0.00|1.000

Table 7.3: Reaction types comparison for three-track MC selection.

CHI2/DOF|K-S	$CC1\pi^+$	BACKGROUND
$CC1\pi^+$	0.00|1.000	1.65|0.098
Background	1.65|0.098	0.00|1.000

The correlation results between the background, $CC1\pi^+$ and CCQE reaction types for the MC single track selection is given in Table 7.1, for two-track selection – in Table 7.2 and for three-track selection – in Table 7.3. The relatively close comparisons for the $CC1\pi^+$ and the background for the latter two are expected to result in large fit uncertainties.

7.4 Data Fitting

Shown in the Figure 7.5 are the g.l. MC reaction code composition (or shape templates) for the water-in single light track sample, and the fit to data using the eq. 7.7. The initial guess values in this and subsequent fits are chosen to be a unity for all coefficients. The resultant p_0 parameter that corresponds to the CCQE coefficient and is very close to one (1.038±0.028) as it is expected from the direct comparison using the CCQE-enriched selection in Figure 7.3. The main value of this step is a low error associated with the p_0 parameter for CCQE.

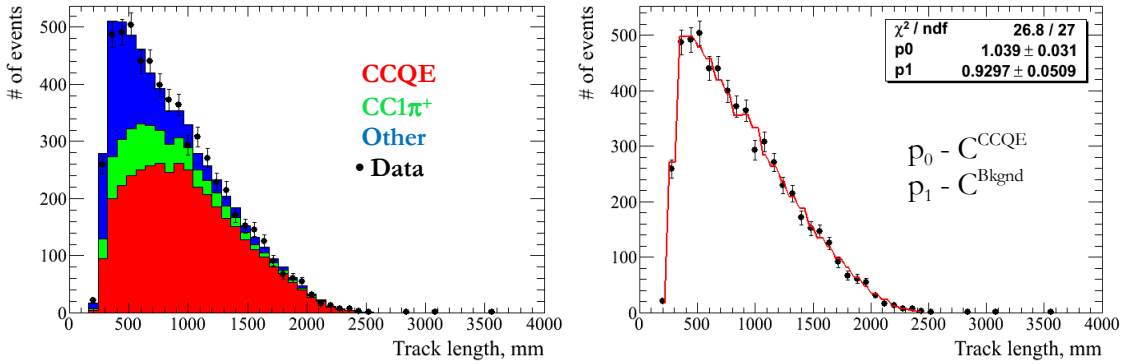

Figure 7.5: Single light track sample MC composition (left) and two-parameter fit to data (right).

The Figure 7.6 presents the full 3-parameter fit (using eq. 7.6) for the water-in single light track sample using the g.l. definitions of the reaction types. Here, the p_1/p_0 is the result being sought for this MC generator and reaction type definition comparison to data (1.24±0.08). The same process is later used for all other generators and reaction type definitions.

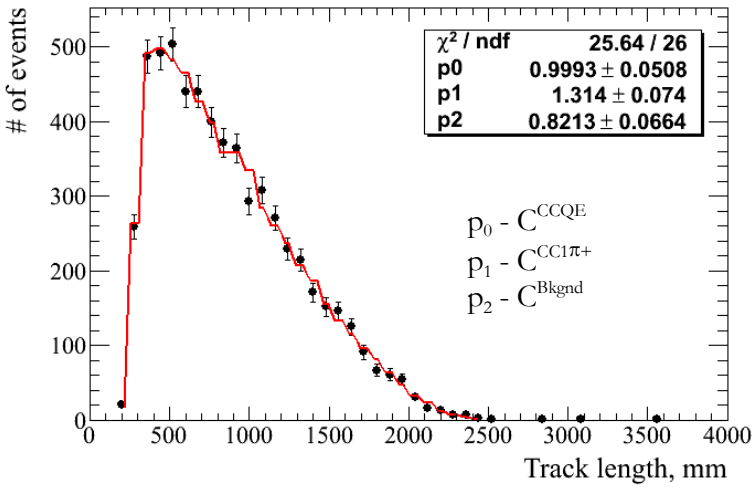

Figure 7.6: Single light track sample three-parameter fit.

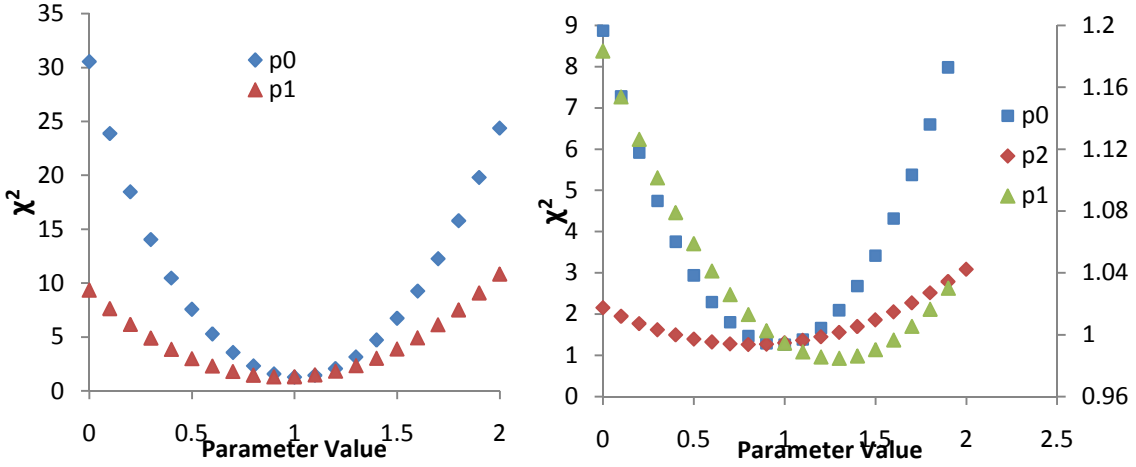

Figure 7.7: Parameter value vs. the χ^2/n.d.f for the single light track sample two-parameter fit (left) and three-parameter fit (right).

7.4.1 Fit Validity Check

For the fit validity checks, plots of the parameter value vs. the χ^2/n.d.f are produced. That is, each fit is repeated with one of the parameters being fixed within a range of x-axis values, for all the parameters in the fit. For the single light track sample, on the left in Figure 7.7 is the plot for a two-parameter fit (that is shown previously on the right of the Figure 7.5) and on the right – for the three-parameter fit (that itself is shown in Figure 7.6).

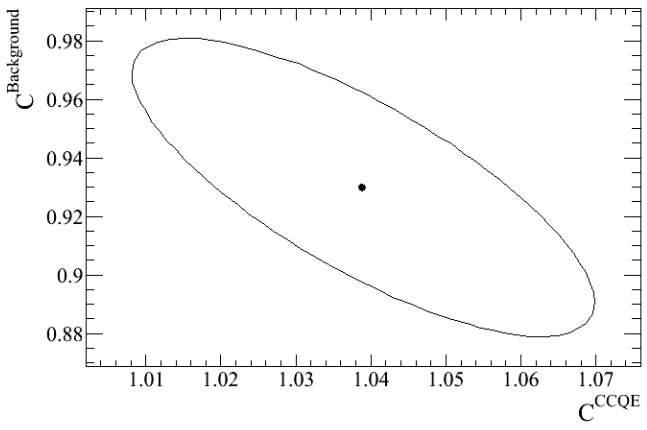

Figure 7.8: The 1-σ contour plot for the single light track sample 2-parameter fit.

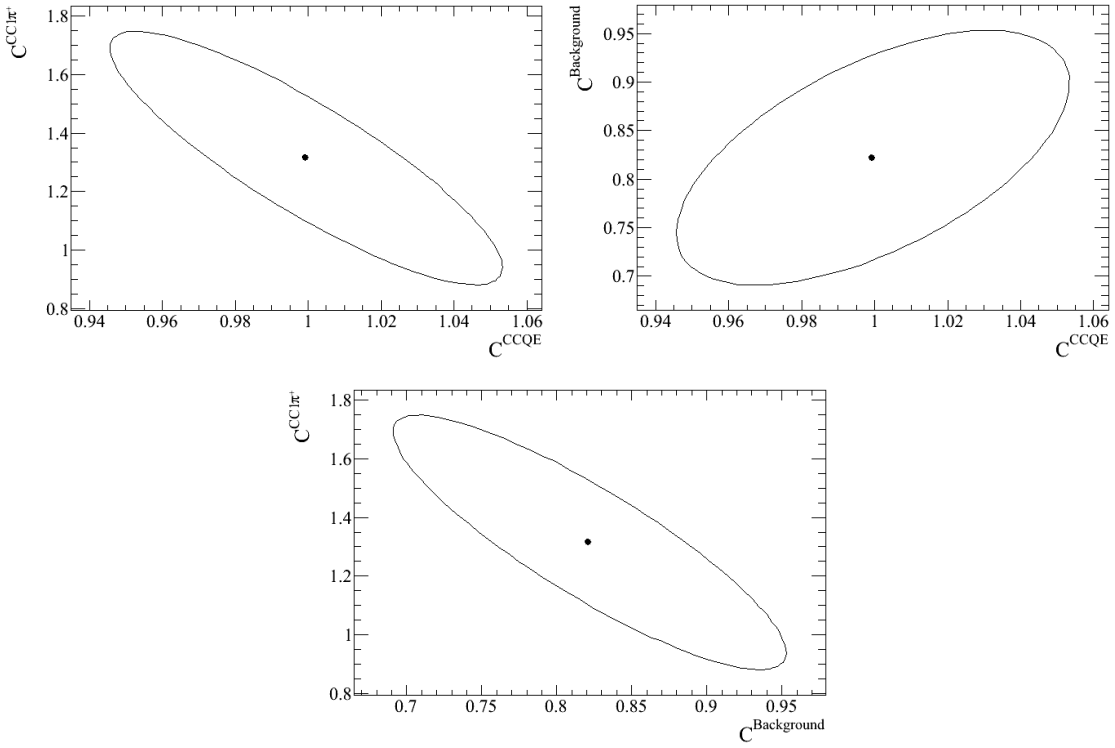

Figure 7.9: The 1-σ contour plots for the single light track sample 3-parameter fit.

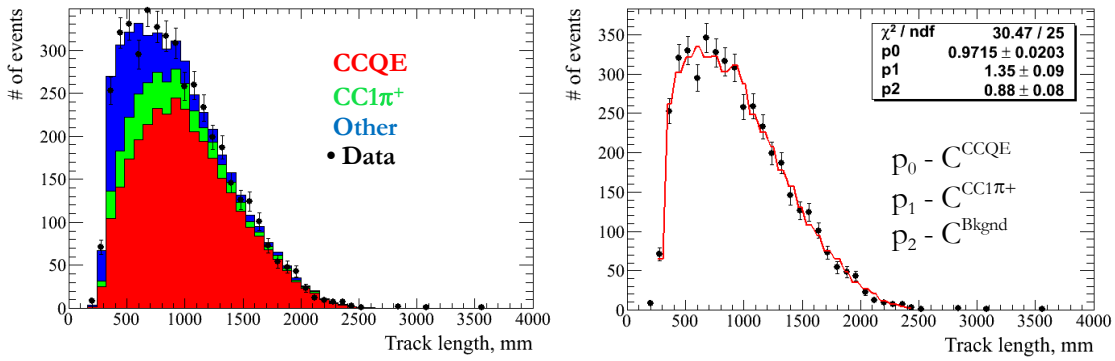

Figure 7.10: Single light track angle cut sample MC composition (left) and fit to data (right).

Each plot displays the expected quadratic behavior with the best fit being achieved at a non-zero parameter value, indicating that it is not a simple linear combination of the remaining parameter(s). No other local minima are found. For the three-parameter fit, a value for the p_1 is plotted using the secondary vertical axis. The smaller effect of the parameter is expected due to smaller number of events in $N_{MC}^{CC1\pi+}$ with respect to others (that is, N_{MC}^{CCQE} and N_{MC}^{bkg}).

Also, the 1-σ contours are drawn for the interactions between the fit variables for the single light track sample 2 and 3-parameter fits. The contour for the 2-parameter fit is presented in Figure 7.8. The marker in the center is at the best fit parameter values. The plot corresponds to the correlation of ~-0.77 between the parameters indicated from the fit correlation matrix.

In the Figure 7.9, the 1-σ contours between fit variables from the 3-parameter fit are shown. These correspond to the ~-0.86 correlations between the C^{CCQE} & $C^{CC1\pi+}$, and $C^{CC1\pi+}$ & $C^{Background}$, with ~0.58 between the C^{CCQE} & $C^{Background}$.

Additionally, the single track angle to the Z axis discrepancy effect on the fit is explored. A cut is made to exclude all the points above cos(angle)>0.89 chosen to remove the large discrepancy region; the resultant plot for the track length is also fitted as shown in Figure 7.10 (right). The results for C^{CCQE} & $C^{CC1\pi+}$ are the same as in Figure 7.6 (within the errors), indicating a very low effect of this cut on the result. The large change is observed in the $C^{Background}$ indicating that the cut removes a sizable part of the background; the resultant is in a better agreement between the data and the MC files. The stacked MC histogram with data is shown in Figure 7.10 (left). The comparison with Figure 7.5 (left) shows the clear background reduction.

To firther elaborate on this, a plot for the cosine of the angle to the Z axis vs. the track length is presented in Figure 7.11 for both the data (left) and MC (right). It illustrates that shorter tracks tend to be at the smailler values of the angle. This reduction of the shorter tracks affects the events with reaction type labeled as 'other' the most as presented in the Figure 7.12.

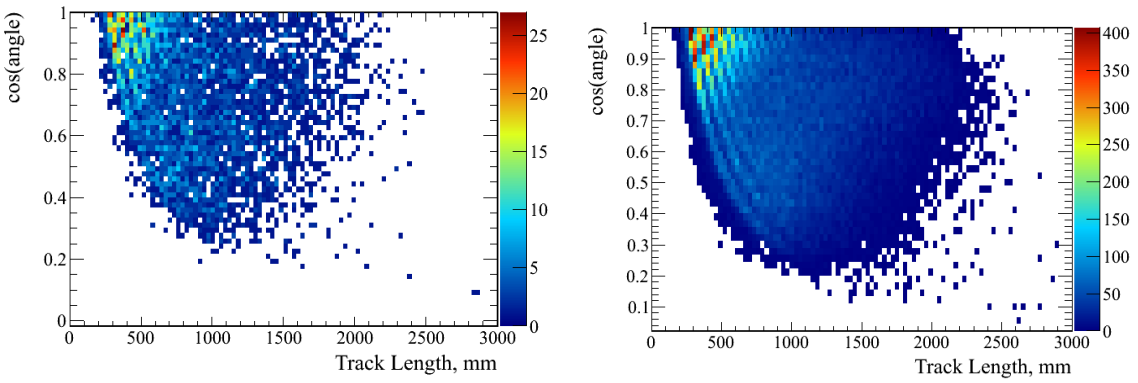

Figure 7.11: Cos(angle) to Z axis vs. the track length. Left plot – data, right plot - MC.

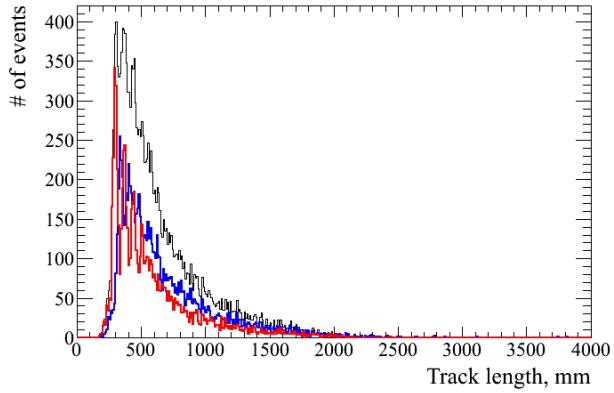

Figure 7.12: Track lengths for 'other' reaction type events using MC truth information. Black line - before the cut, red - cos(angle)>0.89, blue - cos(angle)<0.89.

7.4.2 Fitting of Other Selection

In addition to the single light track sample, other samples have been fitted as well; both the track length and angle histograms. The results of these fits agree with the ratio obtained above within errors. The angle histograms, having more discrepancy between data and MC, tend to have larger errors from the fit. The two fits with best errors are presented below.

For the water-in three-track sample with at least one light track and no showers, Figure 7.13 shows the g.l. MC reaction code composition (left) and the fit to data using eq. 7.8 (right). This sample has much fewer events than a single track sample and coarser binning is used; larger errors for the fit parameters are expected.

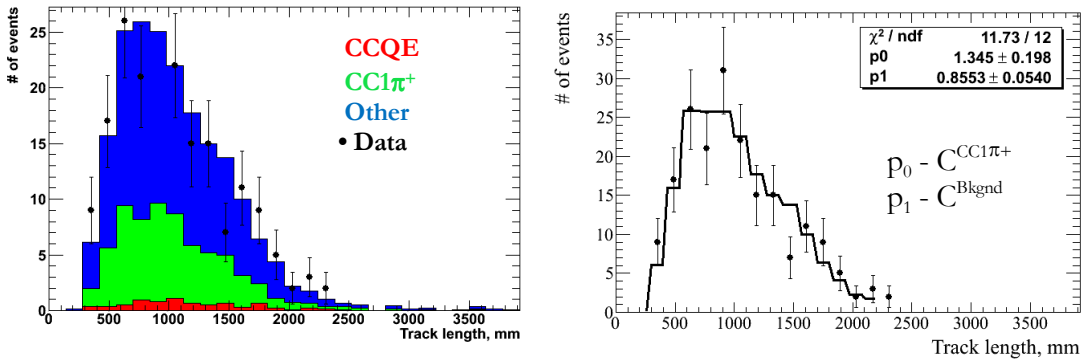

Figure 7.13: Three-track sample MC composition (left) and fit to data (right).

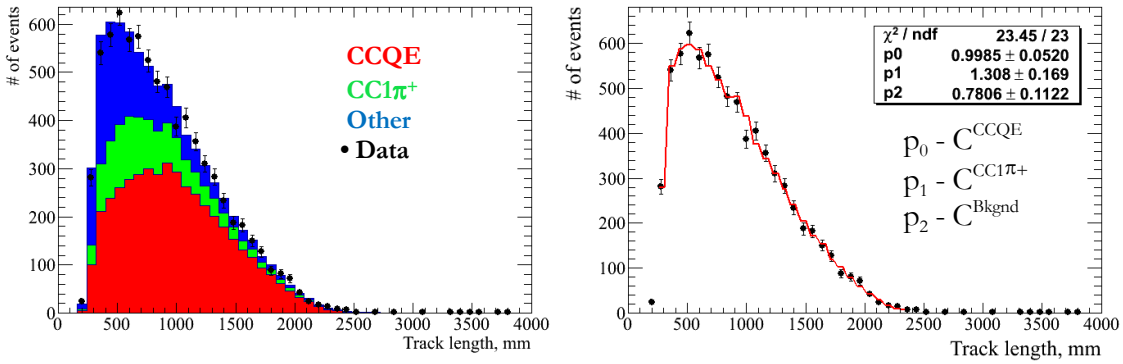

Figure 7.14: Combined one-track and two-track sample track length MC composition (left) and fit to data (right).

The p_0 parameter corresponds to the CC1π^+ coefficient. The peak of the parent neutrino energy for the CC1π^+ in this sample is higher than for the single track one; thus no exact coincidence for the coefficient is expected a priori, but it is in agreement with the fit for the single track sample within errors; same is true for the coefficient for the background contributing event. None of the three-track samples is fitted using eq. 7.6 as the amount of the CCQE events in them is not sufficient for the reliable fit. Note that the correlation between the parameters was 0.982.

All the water-in two-track samples with at least one light track have a very high correlation between the CC1π^+ and the 'other' template histograms >0.96. At the same time, the content of both the CC1π^+ and CCQE is sufficient for the fit. Thus, a combined 1-track and 2-track lengths sample fit using eq. 7.6 is presented in Figure 7.14 (right) with the g.l. MC reaction code composition in Figure 7.14 (left). The parameters ratio (p1/p0) is also in the agreement with the result obtained from the fit of the pure single light track sample.

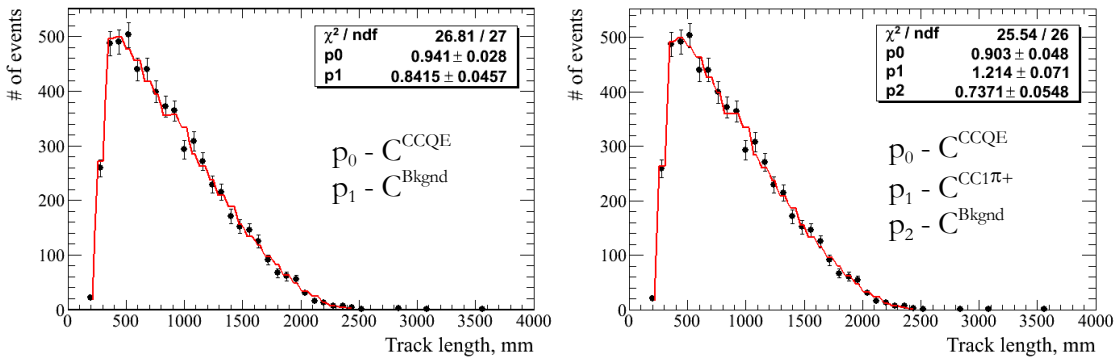

Figure 7.15: The 2-param (left) and 3-param (right) fits for the v3.1 flux reweighted 1-track sample.

7.5 Flux Reweighting

The correction for the flux reweighting released by the beam group was applies (11bTuned-v3.1). The reweighting is due to the improved beam model with NA61 data on pion and kaon production in beam-target collisions. This reweight is a correction applied to the beam flux files used to generate the MC as the beam parameters and decay modes are adjusted. Then the reweight file is released to adjust the existing MC version before a new production is generated. The expectation for the reweight effect for the result is that the fit values should shift; however, their ratio should remain somewhat similar as the reweight values are the same for each MC template histogram bin-by-bin, but vary between the bins.

The reweighting is done by assigning a weight to each MC histogram entry based on the neutrino type and energy from the reweight file. Then the fitting process is done using the new MC templates. The results for v3.1 using the 1-track sample are illustrated in the Figure 7.15.

On the Figure 7.15 left, the 2-parameter fit can be directly compared with the result from Figure 7.5. The p_0 parameter has a low fit error associated with it, thus illustrating the reweighting effect on the CCQE result. Background is affected as well.

The right plot in Figure 7.15 presents the full 3-parameter fit. The same trend is observed here – the values of the parameters are reduced. However, the p_1/p_0 ratio is 1.34 ± 0.09 that corresponds to the ratio before the reweighting within the associated errors. The reweighted results for all the MC generators and event types are produced.

7.6 Systematics

This section is the overview of the systematic errors and their calculations. Since the result is the comparison of the ratios (see eq. 7.1, 7.3), numerous systematics tend to cancel. The largest contributions come from the differences between the MC and the data that arise due to the uncertainties of the MC input parameters or the ways some values are simulated, etc.

Since the $CC1\pi^+$ to CCQE ratio is taken within each selection sample (e.g. single light track), this cancels systematics related to the track reconstruction and PID efficiencies; the data to MC ratio

removes the total flux uncertainties (e.g. normalization), and also the difference in the energy deposition in the detector between data and MC (last part of eq. 7.3).

The Table 7.4 lists all the considered systematics that do not cancel, and their contributions to the final result. A large number of them will have a negligible contribution; for them, the actual value is not calculated after the smallness of the effect is established.

Table 7.4: Systematic errors and their contributions.

SYSTEMATIC	CONTRIBUTION
Track hits inefficiency	very small contrib.
Dark Noise	very small contrib.
Alignment	very small contrib.
Fid. Vol definition and entering tracks (fidvol veto efficiency)	very small contrib.
The uncertainty in the fid.vol. water volume in PØD	Est ~1%
Energy uncertainty between mc flux files and data	Est ~9%

7.6.1 Track hits Efficiency

The MC has perfect hits efficiency, that is, all channels in the simulated detector are operational. If the real detector has a large number of the dead channels, they will affect the data reconstructed tracks by altering their length or splitting then in two.

This calibration is carried out using the long tracks from the 'sand' muons (described in detail in paragraph 5.4). Extremely high efficiency coupled with absence of the 'double-bad' channels (e.g. two neighboring ones, from the bad channels map) point to the extremely small contribution of this effect.

7.6.2 Dark Noise

The effect of dark noise may manifest as increase in track length if a noise hit falls before the track's beginning or the track's end. However, this will happen only if the noise is excessive, and there is a large discrepancy between the data and MC.

The reconstruction package (PØDRecon) has a hit selection procedure that was described in paragraph 6.2.1. The noise hit, being of low charge, will need to occur within a 60 ns window and with a neighbor within 3.5 cm. For the production 4, the MC files lack the noise rate present in the data, however, being random in time and channel, the probability for the noise hit in the data to be exactly

in the right place and time to affect reconstruction process is very small. Figure 7.16[5] shows the noise hits rate both in data and MC for production 4 files.

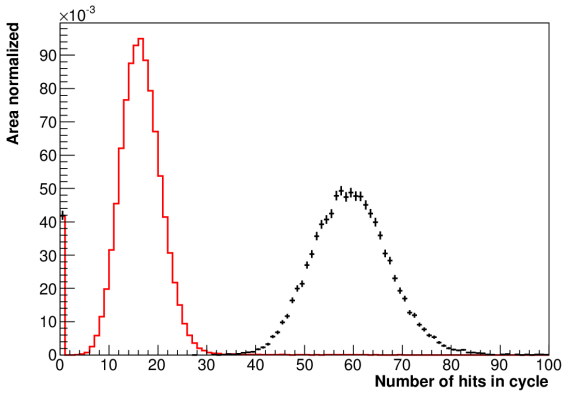

Figure 7.16: Dark noise rate in MC (red) and data files.

7.6.3 Alignment

As the detector is composed of 40 PØDules, the possible misalignments between the layers may affect the track reconstruction (e.g. reconstructing one track as two) if it is large compared to the detector scale. The measurement of the alignment is done in subsection 5.5. As explained in subsection 6.2.1, the width of the 'road' for the track finding algorithm is ~60 mm, and the maximal residuals from the measurements are on order of ~2 mm, thus not affecting the reconstruction.

7.6.4 Fiducial Volume Definition

As the ratio is taken within each selection sample, the effect of the fiducial volume choice cancels for data and MC separately. A check done in subsection 6.3.2 verifies that there is no noticeable effect from the existing fiducial volume choice as it is on the plateau of the ratios between the samples. In particular, due to the event geometry, three-track events are most sensitive to this choice, thus serve as a good cross-check measure. Also the fid. vol requirement provides a veto for any outside events, like cosmics or sand muons.

[5] From the presentation of Phillip Rodrigues, Rochester U.

7.6.5 PØD water volume uncertainty

The uncertainty in the total water in fiducial volume of PØD directly influences the result as it changes the number of the neutrino events that occurred in the water target for the MC generators. But the water is ~1/3 of the fiducial volume thus its effect to the total fit is reduced. With the current estimate of this uncertainty of the water in the fiducial volume of ~10%, propagating to the final systematic error as ~1%±0.08 effect (as a square root of the uncertainty scaled by the square root of the contribution).

7.6.6 Beam Energy Uncertainty

To estimate the shift in the energy between the physical beam and the flux files used for the MC generator, the following procedure was used. The histograms with the track lengths are directly related to the energy of the parent neutrinos. Thus, the shift in the peak of these histograms between the data and the MC is a good estimate for this data-MC discrepancy.

The same procedure was used on the track lengths plots from all selections. The part of each plot with low track lengths is defined by the detector efficiency, the shape of the tail – by detector size and fiducial volume choice. Therefore, an area around the peak was chosen in each case (typically ~±200mm) such that a Gaussian fit to the peak in between was low sensitive to few percent changes to this range. The average shift between the means from MC plots and data plots is measured to be δ=~5%.

The next step involves adjusting the MC template histograms by the measured amount and redoing the fitting. The templates are adjusted bin-by-bin, by following equation:

$$N_i' = \delta N_{i-1} + N_i(1-\delta) \qquad 7.9$$

This shift, for both positive and negative values of δ, yields the values of the ratio of $C^{CC1\pi+}/C^{CCQE}$ that are estimated at ~9%±0.57 different from the original fit without this shift.

7.7 Water-in Results

For the PØD detector water-in data for runs I&II, event selection rules were applied for both the data and MC files. The $CC1\pi^+$/CCQE ratio was used for their comparison (equation 7.3) using the events that are fully contained in the detector. Both the g.l. and the f.s.i. event definitions were used. The results are presented in Table 7.5. The flux reweighed results are presented in Table 7.6. The statistical errors are larger for the f.s.i. defined event types as there are typically less $CC1\pi^+$ events in the template MC histograms. No systematic errors for the intermediate fit parameters were calculated as they are presented for the completeness only. The deviation between the g.l. and the f.s.i., in part, is due to the fact that the g.l. MC selection includes only the $CC1\pi^+$ events whereas the f.s.i. includes the coherent production as well since its final state is almost identical (i.e. a muon and a pion) to the $CC1\pi^+$ final state.

Table 7.5: The water-in data to NEUT and GENIE MC ratio results for both g.l. and f.s.i. event type definitions.

VALUE	NEUT G.L.	NEUT F.S.I.	GENIE G.L.	GENIE F.S.I.
CCQE from 2-param fit	1.039±0.031	1.037±0.028	1.001±0.033	1.003±0.032
Bkgnd from 2-param fit	0.930±0.051	0.914±0.059	0.997±0.052	0.994±0.057
CCQE from 3-param fit	0.999±0.051	1.001±0.067	0.963±0.055	0.975±0.053
$CC1\pi^+$ from 3-param fit	1.314±0.074	1.399±0.107	1.273±0.073	1.268±0.092
Bkgnd from 3-param fit	0.823±0.066	0.831±0.092	0.864±0.083	0.896±0.086
Data-over-MC $CC1\pi^+$/CCQE ratio	1.32 ±0.09($stat$) ±0.13($syst$)	1.40 ±0.13($stat$) ±0.14($syst$)	1.32 ±0.09($stat$) ±0.13($syst$)	1.30 ±0.11($stat$) ±0.13($syst$)

Table 7.6: The water-in data to flux v3.1 reweighted NEUT and GENIE MC ratio results.

VALUE	NEUT G.L.	NEUT F.S.I.	GENIE G.L.	GENIE F.S.I.
CCQE from 2-param fit	0.941±0.028	0.939±0.025	0.905±0.0302	0.907±0.029
Bkgnd from 2-param fit	0.841±0.046	0.827±0.053	0.902±0.046	0.899±0.051
CCQE from 3-param fit	0.903±0.048	0.907±0.061	0.867±0.051	0.879±0.048
$CC1\pi^+$ from 3-param fit	1.214±0.071	1.272±0.080	1.177±0.070	1.167±0.083
Bkgnd from 3-param fit	0.737±0.055	0.750±0.083	0.771±0.087	0.805±0.060
Data-over-MC $CC1\pi^+$/CCQE ratio	1.34 ±0.09($stat$) ±0.13($syst$)	1.40 ±0.10($stat$) ±0.14($syst$)	1.36 ±0.09($stat$) ±0.14($syst$)	1.33 ±0.10($stat$) ±0.13($syst$)

8. WATER-OUT DATA ANALYSIS

8.1 Water-out Fit and Results

As mentioned in chapter 7.1, the dataset from Run II includes also the 'water-out' data for run numbers from 7665 to 7754 for the total p.o.t. of 3.57×10^{19}. Same data quality flags were honored as for 'water-in' data selection.

As there are fewer events for this data, the fitting was carried out for the single muon-like track selection only. Save checks and validations were used in the processing of the data. The fit results for the NEUT MC g.l. event type definition is shown in Figure 8.1 for 2-parameter fit and in Figure 8.2 for the full 3-parameter fit. As expected, the errors scale up by the ~square root of the ratio of the number of events between the two datasets.

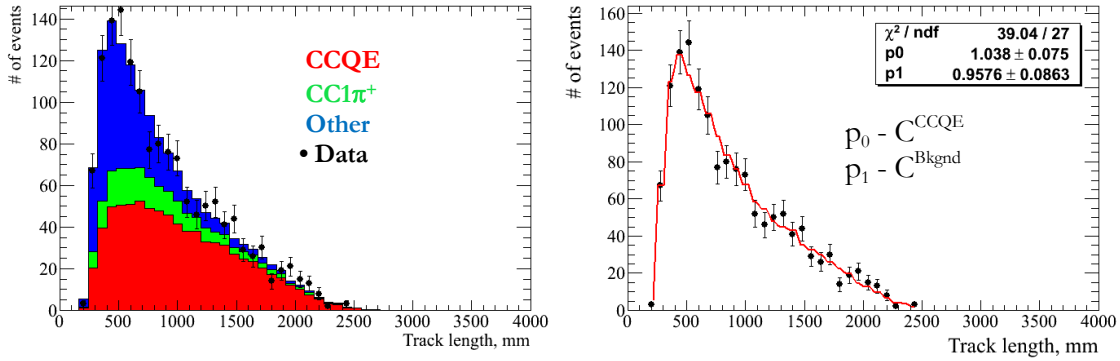

Figure 8.1: Single light track sample MC composition (left) and two-parameter fit to data (right).

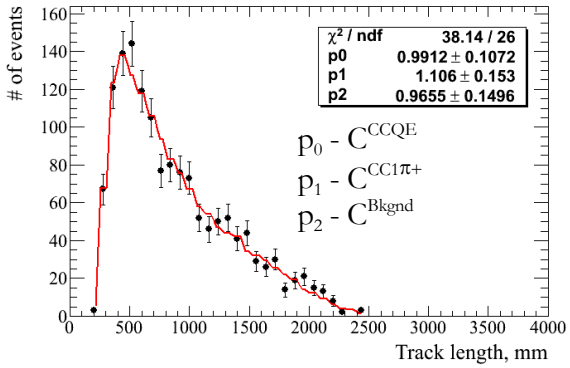

Figure 8.2: Single light track sample three-parameter fit.

Table 8.1: The water-out data to NEUT and flux v3.1 reweighted NEUT MC ratio results for both g.l. and f.s.i. event type definitions.

VALUE	NEUT G.L.	NEUT F.S.I.	NEUT G.L. FLUX REWEIGHTED	NEUT F.S.I. FLUX REWEIGHTED
CCQE from 2-param fit	1.038±0.075	1.030±0.068	0.942±0.068	0.935±0.062
Bkgnd from 2-param fit	0.958±0.086	0.959±0.096	0.864±0.077	0.864±0.086
CCQE from 3-param fit	0.991±0.107	0.992±0.084	0.900±0.083	0.900±0.088
$CC1\pi^+$ from 3-param fit	1.106±0.153	1.167±0.168	1.005±0.163	1.062±0.164
Bkgnd from 3-param fit	0.965±0.150	0.966±0.134	0.867±0.135	0.868±0.121
Data-over-MC $CC1\pi^+/CCQE$ ratio	1.12 $\pm 0.19(stat)$ $\pm 0.11(syst)$	1.18 $\pm 0.19(stat)$ $\pm 0.12(syst)$	1.12 $\pm 0.18(stat)$ $\pm 0.11(syst)$	1.18 $\pm 0.19(stat)$ $\pm 0.12(syst)$

The fit results for both g.l. and f.s.i event type definitions with and without the reweighting using the 11bTuned-v3.1 flux are resented in Table 8.1. No GENIE 'water-out' MC was available at the time of this analysis. The NEUT water-out MC created by same software versions as the 'water-in' was used for the total of 77.8×10^{19} p.o.t.

8.2 On-water Fit and Results

With the water-in data and water-out results, the data to MC comparison of the $CC1\pi^+/CCQE$ ratio on water can be attempted. Please note that since there are just two MC versions, with water-in and water-out, previously quoted comparison results are fully meaningful and can be used further in the future MC tuning and oscillation analyses. This further work to obtain the ratio for the events 'on-water' is supplemental and is presented for the analysis completeness.

The following procedure is used. The water-in MC is reprocessed with additional selection criteria applied to the vertex from the MC truth information: geometric - if the coordinates of the true vertex fall within any water bag, and target material – select oxygen and hydrogen only. Events passing this selection are separated into their own 'in-water' template histogram set; all other events are filled into their own 'in-PØDule' one. Each set subdivides by the g.l. or f.s.i. reaction definitions (e.g. CCQE, $CC1\pi^+$ and OTHER).

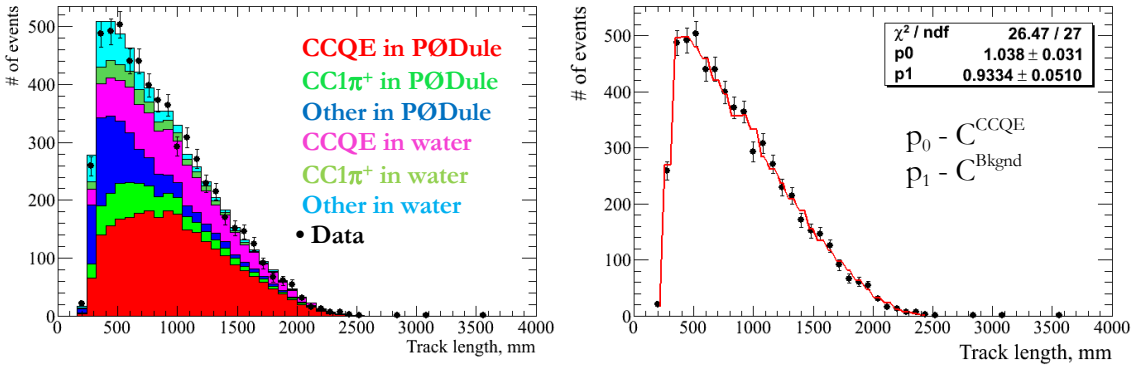

Figure 8.3: Single light track sample MC composition with 'in-water' and scaled 'in-PØDule' templates shown separately (left); two-parameter fit to data (right).

This way, the 'in-PØDule' set of the templates is viewed as the 'water-out' MC. This is not an exact match, the total detector mass without water is ~3 ton less, and thus the pure 'water-out' data has different energy for charged particles (lower E) with tracks that are contained within PØD w.r.t. the 'in-PØDule' set. In addition, detection and reconstruction efficiencies can be different between these sets but these differences are assumed small as no obvious discrepancies were found.

Then, the 'in-PØDule' set of the templates can be scaled by the values of the corresponding C coefficients that were obtained from the 'water-out' fit to data. The 'in-water' set is then added to form again only three template histograms, each consisting of the 'in-water' part and the scaled 'in-PØDule' part. These resultant templates are then fitted to the 'water-in' data following the procedure in chapter 7.4.

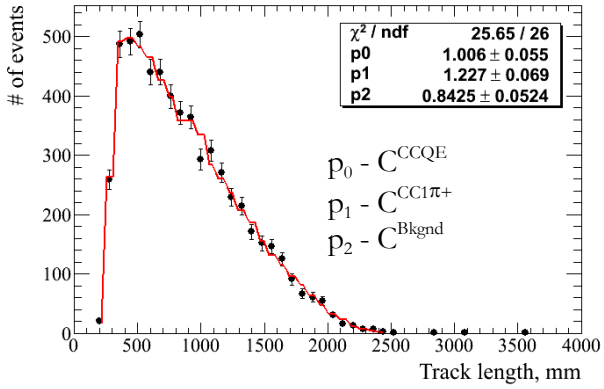

Figure 8.4: Single light track sample three-parameter fit.

As before, the 2-parameter fit for the un-weighted g.l. NEUT MC is presented in Figure 8.3 (right) and the MC composition with the 'in-water' and the already scaled 'in-PØDule' template histograms marked with different colors is in the Figure 8.3 (left). Figure 8.4 shows the full 3-parameter fit. Note that the CCQE parameter (p0) is ~1 for both fits.

Error estimation is a rather difficult task for this analysis as there are assumptions within it that the differences between the water in and out data and MC are small in comparison with other sources of errors as these are very difficult and excessively time consuming to assess. Another assumption is that both the data samples and the MC productions used are free or errors that cause large discrepancies (or have similar error, thus still being comparable). Therefore, an error analysis presented here includes only the presumed largest contributions that are reasonably fast to estimate to the first order.

For the statistical error on the ratio, its main source is the errors estimated during the fit. However, as the template histograms that went into the fit were combined from two parts, the difference between the number of events in the 'in-water' part and the total of the templates will increase the statistical error to the first order by about $\sqrt{72376/22318}$ that is the total number of MC entries over the number of entries in the 'in-water' templates (for NEUT g.l.).

The systematic error will include all the sources mentioned before plus at least two additional sources that are estimated to give the largest contribution. These are the water-out C coefficient errors propagation and the uncertainty in the total water volume in PØD.

As the 'in-PØDule' parts of the templates were scaled by the result from the 'water-out' fit, the statistical errors that were associated with those C coefficients used will propagate to the systematic error for this result.

The difficulty in directly estimating this error is due to the way the template were added to each other and used to form the fit function. Thus the following method was used: for each of the three C parameters used, a set of random numbers was generated using the normal distribution with the width corresponding to the associated error of each. A special ROOT.RooMultiVarGaussian function was used to generate these as triplets due to their correlations, where the correlation matrix from the 'water-out' data fit output was used.

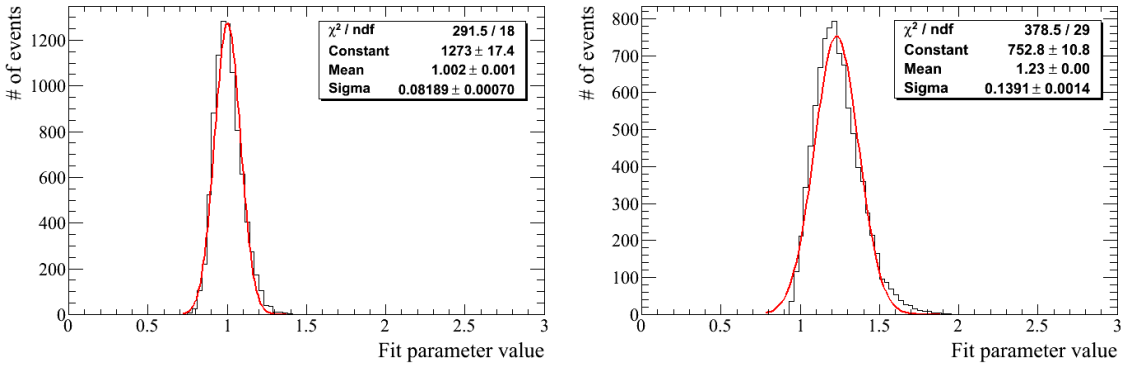

Figure 8.5: Distributions of the C^{CCQE} (left) and $C^{CC1\pi+}$ (right) fit coefficients for different random scale triplets.

Presented in Figure 8.5 are the fit values of the first two coefficients (that form the ratio needed) as the 9000 random scaling values for the 'in-PØDule' parts of the templates are used. Their distributions are not strictly Gaussian due to the correlations that exist between the scaling values; however, a Gaussian fit will suffice to a first order width estimation. The sigma values from these fits are added to the systematic error of the final ratio.

Table 8.2: List of errors included the on-water analysis.

ERROR SOURCE	STATISTICAL OR SYSTEMATIC	ERROR VALUE
Fit Errors	Statistical	~7.5%
Fit is using reduced number of events (on-water vertexes)		Scaled by total MC events to 'in-water' $\sqrt{72376/22318}$
	Total Stat.:	~14%
Energy uncertainty between mc flux files and data	Systematic	~9%
Errors propagated from the water-out fit		~13%
Water volume uncertainty		~3.2%
	Total Syst.:	~16%

Table 8.3: The on-water data to NEUT and flux v3.1 reweighted NEUT MC ratio results for both g.l. and f.s.i. event type definitions.

VALUE	NEUT G.L.	NEUT F.S.I.	NEUT G.L. FLUX REWEIGHTED	NEUT F.S.I. FLUX REWEIGHTED
CCQE from 2-param fit	1.038±0.031	1.033±0.029	1.000±0.030	1.001±0.028
Bkgnd from 2-param fit	0.933±0.051	0.921±0.059	0.892±0.048	0.893±0.057
CCQE from 3-param fit	1.006±0.055	1.001±0.059	0.973±0.054	0.973±0.078
$CC1\pi^+$ from 3-param fit	1.227±0.069	1.309±0.086	1.127±0.078	1.243±0.071
Bkgnd from 3-param fit	0.843±0.052	0.847±0.072	0.814±0.072	0.823±0.077
Data-over-MC $CC1\pi^+/CCQE$ ratio	1.22 ±0.16(stat) ±0.20(syst)	1.31 ±0.19(stat) ±0.21(syst)	1.16 ±0.16(stat) ±0.19(syst)	1.28 ±0.19(stat) ±0.20(syst)

The uncertainty in the total water volume in PØD needs to be accounted for. Here, the number of the on-water events both in data and MC is linearly dependent of the amount of water in the detector. This amount is currently estimated at ~10% precision, propagating as a 10% uncertainty in the number of the events in the template histograms. As this is a fairly small contribution, it will propagate approximately as $\sim\sqrt{10}$ % to a first order. The Table 8.2 lists all the errors included in this analysis. The final results of this analysis are presented in the Table 8.3.

9. CONCLUSION

The PØD detector for the T2K experiment was successfully designed, produced, assembled and commissioned. The calibration using the cosmic rays and 'sand' muon was carried out. The water-in and water-out data for 2 runs was collected.

The data to MC comparison of the CC1π^+/CCQE ratio was conducted using two reaction definitions – g.l. and f.s.i, and for two MC generators – NEUT and GENIE (water-in data only). Latest flux tuning was used. These results are presented in Table 9.1.

The T2K experiment is a new experiment that started the data collection recently. The current results are limited by the statistics due to the low amount of data. As the running of the experiment will continue with more data accumulated, the work presented in this dissertation and similar analyses will be included in the more accurate measurements of the neutrino oscillation parameters to reduce the systematic errors due to the cross-section uncertainties. Most importantly, the schedule for the current year run with 'water out' for the PØD detector will allow for the water in-out subtraction to obtain the neutrino interaction cross-sections on water, specifically the NC1π^0, that will be directly beneficial to the oscillation measurements.

Table 9.1: Data to MC CC1π^+/CCQE ratio comparison results.

WATER IN/OUT	GENERATOR NAME	REACTION TYPE DEFINITION	FLUX TUNING	DATA-OVER-MC CC1π^+/CCQE RATIO
Water-out	NEUT	g.l.	none	$1.12\pm0.19(stat)\pm0.11(syst)$
			11b v3.1	$1.12\pm0.18(stat)\pm0.11(syst)$
		f.s.i.	none	$1.18\pm0.19(stat)\pm0.12(syst)$
			11b v3.1	$1.18\pm0.19(stat)\pm0.12(syst)$
Water-in	NEUT	g.l.	none	$1.32\pm0.09(stat)\pm0.13(syst)$
			11b v3.1	$1.34\pm0.09(stat)\pm0.13(syst)$
		f.s.i.	none	$1.40\pm0.13(stat)\pm0.14(syst)$
			11b v3.1	$1.40\pm0.10(stat)\pm0.14(syst)$
	GENIE	g.l.	none	$1.32\pm0.09(stat)\pm0.13(syst)$
			11b v3.1	$1.36\pm0.09(stat)\pm0.14(syst)$
		f.s.i.	none	$1.30\pm0.11(stat)\pm0.13(syst)$
			11b v3.1	$1.33\pm0.10(stat)\pm0.13(syst)$

WORKS CITED

1. **E. Fermi.** Z. Phys. 88, 161 (1934).
2. **F. Reines and C. L. Cowan.** "The Neutrino". Nature 178 (1956) 446–449.
3. **G. Danby, J. M. Gaillard, K. Goulianos, L. M. Lederman, N. B. Mistry.** "Observation of High-Energy Neutrino Reactions and the Existence of Two Kinds of Neutrinos". Phys. Rev. Lett. 9, 36 (1962).
4. **K. Kodama et al. [DONUT Collaboration].** "Observation of tau-neutrino interactions". Phys. Lett. B504 (2001) 218–224, arXiv:hep-ex/0012035.
5. **B. Pontecorvo.** "Mezonium and unti-mezonium". Sov.Phys.JETP 6 429 (1957).
6. **J. Davis, Raymond, D. S. Harmer, and K. C. Hoffman.** "Search for neutrinos from the sun". Phys. Rev. Lett. 20 (1968) 1205–1209.
7. **K. Abe at al.** "The T2K Experiment". NIM A Jun 06, 2011 NIMA-D-11-00462R1, doi: 10.1016/j.nima.2011.06.067, arXiv:1106.1238 [physics.ins-det].
8. **K.Abe at al.** "First Muon-Neutrino Disappearance Study with an Off-Axis Beam". 6 Jan 2012, arXiv:1201.1386 [physics.hep-ex].
9. **K. Abe at al.** "Indication of Electron Neutrino Appearance from an Accelerator-produced Off-axis Muon Neutrino Beam". Jun15 2011, arXiv:1106.2822 [physics.hep-ex].
10. **Kuraray America Inc.** 200 Park Ave, NY 10166,USA; 3-1-6, NIHONBASHI, CHUO-KU, TOKYO 103-8254, JAPAN.
11. **Beznosko, Dmitriy.** Novel Multi-pixel Silicon Photon Detectors and Applications in T2K. SLAC coft repo: ,also arXiv:0910.4429.
12. **D. Beznosko, A. Bross, A. Dyshkant, A. Pla-Dalmau, V. Rykalin.** "FNAL-NICADD Extruder". July FERMILAB-PUB-05-344, 2005.
13. **D. Beznosko, A. Dyshkant, C.K. Jung, C. McGrew, A. Pla-Dalmau, V. Rykalin.** *"The Coupling of the MRS Photodiode with Coated Extruded Scintillator Using Y7 and Y11 WLS Fibers".* s.l. : NOVA, 2009. Vols. Integrated Circuits, Photodiodes and Organic Field Effect Transistors. ISBN: 978-1-60692-660-4.
14. **Hamamatsu Corporation.** 360 Foothill Road, PO Box 6910, Bridgewater, NJ 08807-0919, USA; 314-5,Shimokanzo, Toyooka-village, Iwatagun,Shizuoka-ken, 438-0193 Japan.
15. **D. Drakoulakos et al. [the MINERνA collaboration].** "Proposal to Perform a High-Statistics Neutrino Scattering Experiment Using a Fine-grained Detector in the NuMu Beam" . http://www.pas.rochester.edu/minerva/.
16. **D. Beznosko, A. Dyshkant, C.K. Jung, C. McGrew, A. Pla-Dalmau, V. Rykalin.** "MRS Photodiode Coupling with Extruded Scintillator via Y7 and Y11 WLS Fibers". February FERMILAB-FN-0796, 2007.
17. **Keithley Instruments, Inc.,.** 28775 Aurora Road, Cleveland, OH 44139,USA.
18. **Saint Gobain (Bicron).** 12345 Kinsman Road, Newbury, OH 44065, USA.
19. **A. Dyshkant, D. Beznosko, G. Blazey, D. Chakraborty, K. Francis, D. Kubik et al.** "Small scintillating cells as the active elements in a digital hadron calorimeter for the e+e- linear collider detector". J. Phys. G: Nucl. Part. Phys., 2004, Vol. 30, pp. N1-N16.
20. **Bivar Inc.** 4 Thomas, Irvine, CA 92618, USA.
21. **K. Nitta, E. Aliu, S. Andringa, S. Aoki, S. Choi, U. Dore et al.,.** The K2K SCiBar Detector, . arXiv:hep-ex/0406023 v1 7 Jun 2004.

22. **D. Beznosko, G. Blazey, D. Chakraborty, A. Dyshkant, K. Francis, D. Kubik et al.** "Investigation of a Solid State Photodetector". NIM A, 2005, Vol. 545, pp. 727-737.
23. **Burle Industries Inc.** 1000 New Holland Avenue, Lancaster, Pennsylvania 17601-5688 U.S.A. www.burle.com.
24. **L. Whitehead, K. Kobayashi, C. Yanagisawa.** "Test of the Burle Micro-Channel Plate Multi-Anode Photomultiplier Tube". April 19, 2006. http://www.phy.bnl.gov/~whitehd/MCPnote.pdf.
25. **G. Bondarenko et al.** "Multi-pixel Photon Detectors". Nucl. Instr. and Meth., A242 (2000) p.187.
26. **R. Hanft, B. C. Brown, W. E. Cooper, D. A. Gross, L. Michelotti, E. E. Schmidt et al.** Magnetic Field Properties of Fermilab Energy Saver Dipoles. FERMILAB-TM-1182, March 1983.
27. **Agilent Technologies, Inc.** Headquarters, 395 Page Mill Rd., Palo Alto, CA 94306, United States.
28. **D. Beznosko, G. Blazey, A. Dyshkant, V. Rykalin, V. Zutshi.** "Effects of the Strong Magnetic Field on LED, Extruded Scintillator and MRS Photodiode". NIM A 553 (2005) 438-447.
29. **GMW Associates.** 955 Industrial Road, San Carlos, CA 94070.
30. **Lumex, Inc.,.** 290 East Helen Road Palatine, IL 60067, USA.
31. **RadioShack Corporation.** Riverfront Campus World Headquarters, 300 RadioShack Circle, Fort Worth, TX 76102-1964, USA.
32. **P. Adamson, J. Alner, B. Anderson, T. Chase, P.J. Dervan, T. Durkin et al.,.** The MINOS light-injection calibration system. NuMI-PUB-SCINT, FD_DOCS-0743, NIM A 492 (2002) 325-343,Oct. 21, 2002.
33. **Dan Green, Anatoly Ronzhin, Vasken Hagopian,.** "Magnetic Fields and Scintillator Performance". FERMILAB-TM-1937, June 1995.
34. **Tektronix Inc.** 14200 SW Karl Braun Drive, P.O. Box 500, Beaverton, OR, 97077 USA.
35. **Newport Corporation.** 1791 Deere Avenue, Irvine, CA, 92606 USA.
36. **D. Beznosko, P. Polozov, V. Rykalin, G. Sellberg.** "Fiber Positioning and MRS Response". FERMILAB-TM-2247, May 7, 04.
37. Hamamatsu MPPC product information datasheet. http://sales.hamamatsu.com/en/products/solid-state-division/si-photodiode-series/mppc.php.
38. **Hideyuki Oide et al.** "Study of Afterpulsing of MPPC with Waveform Analysis". PD07 conference presentation.
39. **M. Yokoyama et al.** "Development of Multi-Pixel Photon Counters". SNIC Symposium, Stanford, CA 3-6 April, 2006.
40. **Minamino, Akihiro at al.** "T2K experiment: Neutrino Detectors". 10/3/2009.
41. **D. Ruterbories at al.** "MPPC Testing at CSU". T2K Workshop, Jan 2009.
42. **J. Estrada, C. Garcia, B. Hoenison, and P. Rubinov.** "MCM II and the TRIPT chip". D0 note 4009, Fermilab-TM-2226, Dec 2003.
43. "Trip-T description". *FNAL internal papers.* smb://D0server6/projects/TriggerElectronics/CAE/Run_IIb_AFE.
44. **Xilinx, Inc.** 2100 Logic Drive, San Jose, CA 95124-3400, USA.
45. **LeCroy Corporation.** 700 Chestnut Ridge Road, Chestnut.
46. **ORTEC.** 801 South Illinois Avenue, Oak Ridge, TN 37830.
47. **S. Assylbekov, B. E. Berger, H. Berns, D. Beznosko, A. Bodek, R. Bradford at al.** "The T2K ND280 Off-Axis Pi-Zero Detector". 21 Nov 2011, arXiv:1111.5030v1 [physics.ins-det].
48. ShopBot Tools, Inc. , 3333 Industrial Dr., Durham, NC 27704 USA.
49. **R. Brun, F. Rademakers.** *'ROOT: An object oriented data analysis framework'*. Nucl. Instrum. Meth. A389 (1997) 81–86.
50. **S. Agostinelli et al.** GEANT4: A Simulation toolkit. Nucl. Instrum. Meth. A506 (2003) 250–303.
51. **Mitsuka, G.** "NEUT". AIP Conf. Proc. 981 (2008) 262–264.

52. **Y. Hayato.** "NEUT". Nucl. Phys. Proc. Suppl. 112 (2002) 171–176.
53. **C. Andreopoulos, et al.** The GENIE Neutrino Monte Carlo Generator. Nucl. Instrum. Meth. A614 (2010) 87–104.
54. **W.T.Eadie, D.Drijard, F.James, M.Roos, and B.Sadoulet.** Statistical Methods in Experimental Physics. North-Holland, 1971.
55. **D. Beznosko, G. Blazey, D. Chakraborty, A. Dyshkant, K. Francis, D. Kubik, J.G.R. Lima, J. McCormick et al.,.** "LCDG4 and DigiSim - Simulation activities at NICADD/NIU". FERMILAB-CONF-05-342-E, Jul 27, 2005.
56. **A. Dyshkant, D. Beznosko, G. Blazey, V. Rykalin, V. Zutshi.** Quality Control Studies of Wavelength Shifting Fibers for a Scintillator- based Tail-Catcher Muon-Tracker Linear Collider Prototype Detector. IEEE Trans.Nucl.Sci.53:3944-3948,2006.
57. **D. Beznosko, G. Blazey, A. Dyshkant, V. Rykalin, J. Schellpffer, V. Zutshi.** Modular Design for Narrow Scintillating Cells with MRS Photodiodes in Strong Magnetic Field for ILC Detector. Nucl.Instrum.Meth.A564:178-184,2006.
58. **D. Beznosko, G. Blazey, A. Dyshkant, V. Rykalin.** Effects of the 9T Magnetic Field on MRS Photodiode. FERMILAB-PUB-05-410, Sep. 20, 2005.
59. **A. Dyshkant, D. Beznosko, A. Pla-Dalmau, V. Rykalin.** Extruded scintillator for the Calorimetry applications. FERMILAB-CONF-06-281, Aug 2006.;AIP Conf.Proc.867:513-520,2006.
60. **C. Andreopoulos, et al.,.** The GENIE Neutrino Monte Carlo Generator. Nucl. Instrum. Meth. A614 (2010) 87–104.
61. **K.Abe, O.Araoka, F.d.M.Blaszczyk, D. Beznosko, C.K. Jung, M.Khabibullin, R.P. Litchfield, K.Nishikawa at. al.** "The T2K Experiment". *T2K Internal Document.* NIM A Jun 06, 2011 NIMA-D-11-00462R1, doi: 10.1016/j.nima.2011.06.067, arXiv:1106.1238 [physics.ins-det].

APPENDIX I

Below is the python code that uses oaAnalysis final interaction state information to define the reaction type using NEIT codes 1 (ccqe), 11 (CC1π^+ on proton), 12 (CC1π^0), 13 (CC1π^+ on neutron) and 200 for all others. The code is adopted from oaAnalysis internal code.

```
neKL = truth['eta number']+truth['lambda number']+truth['other charged mesons number']

pionnumber=truth['pizero number']+truth['piplus number']+truth['piminus number']

pionnumbercharged=truth['piplus number']+truth['piminus number']

pionnumberother=truth['pizero number']+truth['piminus number']

#

if truth['muon neutrino found'] and truth['muon found'] and not neKL and not pionnumber:
truth['DetectorReactionCode']=1

#

elif truth['muon neutrino found'] and truth['muon found'] and truth['piplus number']==1 and not
neKL and not pionnumberother: truth['DetectorReactionCode']=11

#

elif truth['muon neutrino found'] and truth['muon found'] and truth['pizero number']==1 and not
neKL and not pionnumbercharged: truth['DetectorReactionCode']=12

#

else:truth['DetectorReactionCode']=200

##

if truth['DetectorReactionCode']==11 and truth['neutron number'] and not truth['proton
number']: truth['DetectorReactionCode']=13
```

APPENDIX II

Below are the NEUT neutrino event generator internal reaction codes.

NEUTRINO MODE

CHARGED CURRENT
-- ELASTIC --
1 : NU,N-->LEPTON-,P
-- SINGLE PI FROM DELTA RESONANCE --
11 : NU,P-->LEPTON-,P,PI+
12 : NU,N-->LEPTON-,P,PI0
13 : NU,N-->LEPTON-,N,PI+
16 : NU,O(16)-->LEPTON-,O(16),PI+
-- MULTI PI (1.3 < W < 2.0 GeV) --
21 : NU,(N|P)-->LEPTON-,(N|P),MULTI PI
-- SINGLE ETA FROM DELTA RESONANCE --
22 : NU,N-->LEPTON-,P,ETA0
-- SINGLE K FROM DELTA RESONANCE --
23 : NU,N-->LEPTON-,LAMBDA,K+
-- DEEP INELASTIC (2.0 GeV < W , JET set) --
26 : NU,(N|P)-->LEPTON-,(N|P),MESONS

NEUTRAL CURRENT
-- SINGLE PI FROM DELTA RESONANCE --
31 : NU,N-->NU,N,PI0
32 : NU,P-->NU,P,PI0
33 : NU,N-->NU,P,PI-
34 : NU,P-->NU,N,PI+
36 : NU,O(16)-->NU,O(16),PI0
-- MULTI PI (1.3 GeV < W < 2.0 GeV) --
41 : NU,(N|P)-->NU,(N|P),MULTI PI
-- SINGLE ETA FROM DELTA RESONANCE --
42 : NU,N-->NU,N,ETA0
43 : NU,P-->NU,P,ETA0
-- SINGLE K FROM DELTA RESONANCE --
44 : NU,N-->NU,LAMBDA,K0
45 : NU,P-->NU,LAMBDA,K+
-- DEEP INELASTIC (2.0 GeV < W , JET set) --
46 : NU,(N|P)-->NU,(N|P),MESONS
-- ELASTIC --
51 : NU,P-->NU,P
52 : NU,N-->NU,N

ANTI NEUTRINO MODE

CHARGED CURRENT

-- ELASTIC --
-1 : NUBAR,P-->LEPTON+,N
-- SINGLE PI FROM DELTA RESONANCE --
-11 : NUBAR,N-->LEPTON+,N,PI-
-12 : NUBAR,P-->LEPTON+,N,PI0
-13 : NUBAR,P-->LEPTON+,P,PI-
-16 : NUBAR,O(16)-->LEPTON+,O(16),PI-
-- MULTI PI (W > 1.4 GEV) --
-21 : NUBAR,(N|P)-->LEPTON+,(N|P),MULTI PI
-- SINGLE ETA FROM DELTA RESONANCE --
-22 : NUBAR,P-->LEPTON+,N,ETA0
-- SINGLE K FROM DELTA RESONANCE --
-23 : NUBAR,P-->LEPTON+,LAMBDA,K0
-- DEEP INELASTIC (2.0 GeV < W , JET set) --
-26 : NUBAR,(N|P)-->LEPTON+,(N|P),MESONS

NEUTAL CURRENT
-- SINGLE PI FROM DELTA RESONANCE --
-31 : NUBAR,N-->NUBAR,N,PI0
-32 : NUBAR,P-->NUBAR,P,PI0
-33 : NUBAR,N-->NUBAR,P,PI-
-34 : NUBAR,P-->NUBAR,N,PI+
-36 : NUBAR,O(16)-->NUBAR,O(16),PI0
-- MULTI PI (W > 1.4 GEV) --
-41 : NUBAR,(N|P)-->NUBAR,(N|P),MULTI PI
-- SINGLE ETA FROM DELTA RESONANCE --
-42 : NUBAR,N-->NUBAR,N,ETA0
-43 : NUBAR,P-->NUBAR,P,ETA0
-- SINGLE K FROM DELTA RESONANCE --
-44 : NUBAR,N-->NUBAR,LAMBDA,K0
-45 : NUBAR,P-->NUBAR,LAMBDA,K+
-- DEEP INELASTIC (2.0 GeV < W , JET set) --
-46 : NUBAR,(N|P)-->NUBAR,(N|P),MESONS
-- ELASTIC --
-51 : NUBAR,P-->NUBAR,P
-52 : NUBAR,N-->NUBAR,N